Visualization of Heterogeneity in Materials for Lithium Batteries Using Micro X-ray Diffraction

by

Chao Li
B.S. University of Massachusetts Boston

Thesis submitted in partial fulfillment of the requirements
for the degree of Doctor of Philosophy in Chemistry (Analytical Chemistry)
in the Graduate College of the
University of Illinois at Chicago, 2021

Chicago, Illinois

Defense Committee:
Jordi Cabana, Chair and Advisor
Stephanie Cologna
Luke Hanley
Michael Trenary
Kamila Wiaderek, X-ray Science Division, Advanced Photon Source

ACKNOWLEDGMENTS

I would like to express my sincere and deepest appreciation to Prof. Jordi Cabana, my research advisor. It is impossible for me to achieve my goals along this journey without him. His enthusiasm on chemistry and life has inspired me. His patient guidance and valuable advice kept my progress on schedule. He is always willing to give me encouragement and enlighten me by sharing his experience. Prof. Cabana is not only an excellent research advisor, but also a great idol who has shaped me to become a better person.

I would also like to extend my deepest gratitude to my committee members: Dr. Cologna, Prof. Hanley, Prof. Trenary and Dr. Wiaderek for taking time off their busy schedule to review this thesis and provide feedback and helpful advice to improve it.

I'm extremely grateful to have my research group members who gave me the insights into science from all different perspectives. Assistance and insightful suggestions provided by Dr. Mark Wolfman and Dr. Brian May are greatly and specially appreciated.

The completion of my dissertation would not have been possible without the relentless support and invaluable contribution from my dearest collaborators Dr. Ruqing Xu, Dr. Kamila Wiaderek from Argonne National Laboratory and Dr. Regina García from University of Michigan.

Special thanks to my greatest friends Yuan Zhang, Stefan Ilic and Gene Nolis for their endless encouragement and profound belief in my ability along this journey.

ACKNOWLEDGMENTS (Continued)

Foremost, I wish to show my gratitude to my parents for their love and support.

Lastly, I would like to thank my cat Maomao for his accompany in this thesis writing process. His memory will be with me always.

TABLE OF CONTENTS

TABLE OF CONTENTS (Continued)

LIST OF TABLES

LIST OF FIGURES

LIST OF FIGURES (Continued)

LIST OF ABBREVIATIONS

AMPIX	Argonne's multi-purpose *in situ* X-ray
ANL	Argonne National Laboratory
APS	Advanced Photon Source
ASSLBs	All-Solid-State Lithium Batteries
CCD	Charged-coupled device
EV	Electronic Vehicle
ICDD	International Center for Diffraction Data
LIB	Lithium-ion Battery
LLZO	$Li_7La_3Zr_2O_{12}$
NCA	$LiNi_{0.80}Co_{0.15}Al_{0.05}O_2$
OCV	Open-circuit Voltage
PDF	Powder Diffraction File
PVDF	Polyvinylidene fluoride
PXRD	Powder X-ray Diffraction
RT	Room Temperature
SEI	Solid Electrolytes Interphase
SOC	State of Charge

LIST OF ABBREVIATIONS (Continued)

XRD   X-ray Diffraction

UIC   University of Illinois at Chicago

SUMMARY

X-ray diffraction (XRD) is a powerful characterization technique which has been extensively applied in the study of crystalline materials in many different fields, including pharmaceutical industry, forensic science, mineralogy, microelectronics industry, corrosion analysis even in glass industry.

This thesis focuses on the design and the development of protocols to implement methods of XRD using microbeams to study local electrochemical phenomena relevant to cathode materials and solid electrolytes for batteries based on shuttling Li ions to store charge. With the resulting maps, heterogeneity at several length scales, and their associated chemical and physical properties, can be visualized and assessed both qualitatively and quantitatively.

The μXRD mapping methods were demonstrated at two different length scales. Using a lab X-ray source, in Chapter 3, *ex-situ* XRD mapping was applied to evaluate the electrochemical performance of a complete $LiNi_{0.80}Co_{0.15}Al_{0.05}O_2$ cathode by visualizing how the local distribution of states of charge after cycling is affected by storing the electrode under different conditions. The domains of different delithiation states revealed by the μXRD maps were consistent with the structural analysis based on the bulk powder XRD. By showing the local phase distribution, insight was revealed into the effects on the macroscopic transport of lithium ions of the formation of insulating impurities on the surface of $LiNi_{0.80}Co_{0.15}Al_{0.05}O_2$ cathode during storage.

SUMMARY (Continued)

Taking advantage of an extremely powerful X-ray source, a synchrotron, at Argonne National Laboratory, *operando* μXRD was developed and performed to map secondary particles in Chapter 4. The diffraction patterns of each mapping position revealed compositional gradients within single secondary particles of $LiNi_{0.80}Co_{0.15}Al_{0.05}O_2$ during galvanostatic cycling, based on the comparison of the position and shape of selected diffraction peaks to reference data. The μXRD diffraction patterns were also compared with a previous study with the same technique to reveal the effect of cycling rates on the electrochemical behavior of $LiNi_{0.80}Co_{0.15}Al_{0.05}O_2$ secondary particles.

In Chapter 5, a novel μXRD mapping method with Laue diffraction at a synchrotron was successfully developed and applied to create deviatoric strain maps of garnet-typed solid state electrolytes compositionally derived from $Li_7La_3Zr_2O_{12}$. These deviatoric strain maps helped to visualize the variation in microstructure within the solid electrolytes, which helped rationalize differences in local stability of lithium electrodeposition during cycling.

The ultimate goal of this thesis is to establish correlations between local investigated properties and macroscopic electrochemical performance that affect the performance of batteries and inform their future design toward overcoming existing frontiers in the technology.

CHAPTER 1

INTRODUCTION

1.1 <u>Lithium Batteries</u>

Lithium-ion batteries (LIB) are rechargeable (also referred to as secondary) devices that are widely used in society to power wireless electronics, such as cell phones and laptops, and, increasingly, even electric vehicles (EVs). Their key feature is that they offer a good combination of high energy and power density [13] with a flexible and lightweight design [14]. However, despite the rapid developments of the technology driven by the tremendous expansion of electronic devices in the past two decades, current LIBs are not sufficient for the EV industry, which requires cheaper and more sustainable batteries, with a particular focus on maximizing the density of energy storage.

One of the challenges toward further increasing energy density is to simultaneously minimize degradation to maintain or even improve cycle life. Previous studies have established several mechanisms of capacity fade to explain aging mechanisms of LIB such as parasitic side reactions, formation of insulating interphases, and resistance increase [15]. Several studies also reveal that another way that LIBs see their performance limited is through the introduction charge heterogeneity resulting from how redox reactions take place preferentially within the electrode architectures [2]. To probe and visualize such charge heterogeneity would provide insights into

associated degradation mechanisms, possible among which are disconnection of domains or local overcharge.

A very desirable strategy toward increasing the energy density of a battery based on Li would be through the substitution of the graphite anode used in commercial devices today. When the first lithium-based battery was introduced in 1970s by Nobuatsu Watanabe and Masataro Fukuda [16], pure Li metal was used as the anode instead, motivated by its extremely high theoretical specific capacity (3860 mAh·g^{-1}), the lowest negative electrochemical potential (-3.040 V versus standard hydrogen electrode), and low density (0.534 g·cm^{-3}) [17]. However, this early Li battery system was limited by the formation of Li dendrites and low coulombic efficiency during cycling [18]. As a result, in 1985, the concept of Li-ion battery was developed by Akira Yoshino, with a carbonaceous material as the storage medium for Li ions in substitution of Li metal, which subsequently became widely used in commercial applications for more than 30 years [19]. However, as the push for increased energy storage has re-emerged in the context of EV applications, research efforts have been attracted back to enabling lithium metal. This thesis addresses persistent challenges that apply to both established LIBs and emerging Li metal batteries.

1.1.1 Basic Principles of Li Batteries

A battery is a cell or a group of cells converting chemical energy into electrical energy. A typical Li-ion electrochemical cell consists of an anode (with its potential being more negative), a cathode (more positive), an electrolyte and a separator. Both anode and cathode are active
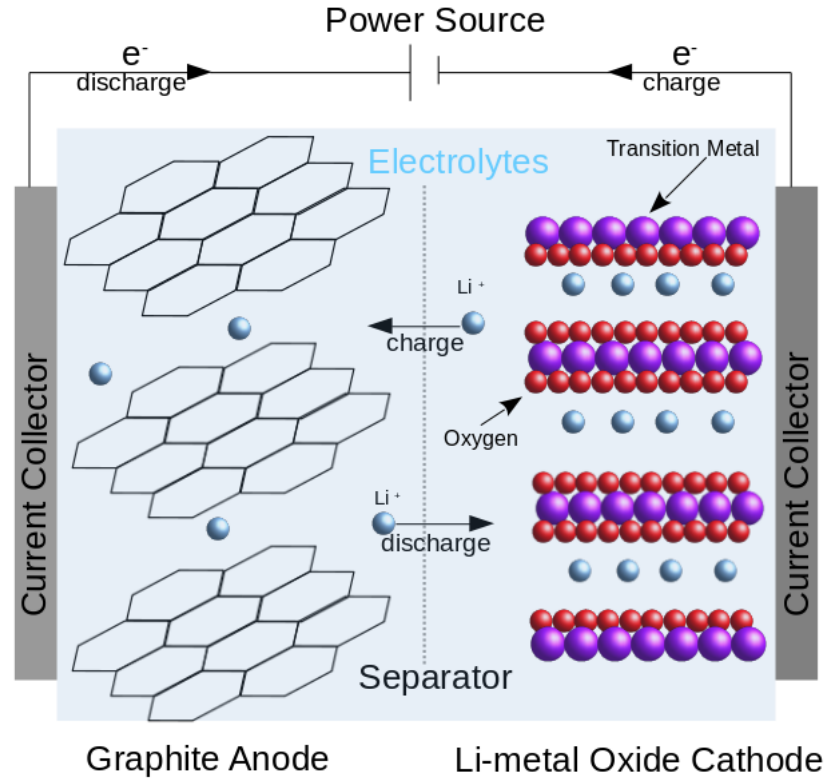
Figure 1. Schematic of a typical Li-ion electrochemical cell.

toward redox reactions within the cell. The cell potential, E_{cell} in volt (V), is determined by the chemical potential difference between cathode and anode.

An example of the possible reactions is provided for the case of Li-ion technology using current commercial devices, with graphite as anode and a lithium transition metal oxide $LiMO_2$ as cathode, where M represents an example of transition metal with oxidation state $+3$ as shown in Figure 1.

$$LiMO_2 \rightleftharpoons Li_{1-x}MO_2 + xLi^+ + xe^- \tag{1.1}$$

$$6\,C + xLi^+ + xe^- \rightleftharpoons LiC_6 \tag{1.2}$$

$$6\,C + LiMO_2 \rightleftharpoons MO_2 + LiC_6 \tag{1.3}$$
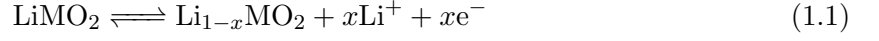
High-energy Li batteries simply arise from the replacement of Li intercalation into graphite by the reaction of plating of Li metal as the anode.

The cathode is oxidized and the anode is reduced during cell charging following the two half reactions at the full reaction above. The lithium ions are transferred from cathode to anode whereas electrons, e^-, move through an external circuit from cathode to anode. The thermodynamic limit of storage enabled by the full reaction can be defined through Gibb's free energy in Equation 1.4,

$$\Delta G = -nF\mathrm{E_{cell}} \tag{1.4}$$

where ΔG is the change of Gibb's free energy during the redox reaction, n is the number of moles of electrons transferred in the spontaneous redox reaction and F is the Faraday constant ($F = 96\ 485\ \mathrm{C\cdot mol^{-1}}$). In battery engineering, capacity is used to describe the total amount of charge in the device, where nF is normalized by the active mass. Furthermore, capacity is commonly measured by ampere-hour(A·h) at the E_{cell} of the battery.

The driving force and the rate of electrochemical reaction of the cell can be controlled by connecting electrodes to an external power supply. The potential of the cell can be controlled

by a potentiostat and the current can be controlled by a galvanostat. The potential difference between electrodes can be used to impose a driving force for the electrochemical reaction in the cell even when it is spontaneous as the battery is discharged. The rate of the reaction is controlled by the electrode overpotential, η_s, as articulated by the *Butler-Volmer* equation [20],

$$i = i_0[exp(\frac{\alpha_a F}{RT}\eta_s) - exp(-\frac{\alpha_c F}{RT}\eta_s)] \tag{1.5}$$

where R is universal gas constant, R = 8.3143 J·mol^{-1}·K^{-1}, T is the absolute temperature in Kelvin, α_a is the anodic charge transfer coefficient, α_c is the cathodic charge transfer coefficient, F is the Faraday constant, i is the current density, the rate of flow of charge per unit area perpendicular to the direction of flow, and i_0 is the exchange current density which is related to the rate constant of the overall reaction. The degradation of Li batteries is often a result of a decrease in i_0, which can be affected by the change of concentration of reactants and products, temperature, the nature of the electrode interphases and impurities on the surface of the electrodes. Losses in battery performance can be detected through the coulombic efficiency (CE). It is the ratio of discharge capacity to charge capacity within the same cycle [21]. The decrease of coulombic efficiency during cycling is an indication of decreased reversibility.

As the applied potential creates the driving force of the electrochemical reaction within the cell, it also creates a potential gradient $\nabla\Phi$ which drives the movement of both ions and electrons. The potential gradient can be related to current density by *Ohm's law* in Equation 1.6 [20],

$$i = -\sigma\nabla\Phi \tag{1.6}$$

where σ is the total conductivity of the cell. This is also the reason why the conductivity of the different battery components is important.

The other important component of a Li battery is the electrolyte. It is a medium which provides the ionic conductivity and electronic insulation to allow Li ion transport between electrodes without electron flow that would induce a short-circuit. Ideally, the ratio of transport of lithium ions over every other ionic species (e.g., anions), also known as the transference number, t_+, will be unity in the electrolyte [22]. While a good electrolyte would also ideally be electrochemically stable against both high-voltage cathode materials and low-voltage anodes, in practice, kinetic stabilization arises from their ability to decompose through the formation of a film on either electrode that is passivating to electron transfer while allowing ions through, namely, a solid electrolyte interphase (SEI) [18]. A carbonate ester-based electrolyte system, such as mixtures of cyclic ethylene carbonate (EC) and linear dimethyl carbonate (DMC), as solvents, and $LiPF_6$ as the solute, is widely used in modern devices because of a high oxidation potential (over 4.2 V vs Li/Li^+) [18]. When liquid electrolytes are used, a separator is also added to the cell to prevent physical contact between the electrodes, and, thus, avoid internal electrical shorting. A polypropylene membrane (e.g., Celgard 2400) is common because of its good chemical stability and mechanical strength. Glass fiber was also used in this thesis to conduct specialty measurements with the Argonne's multi-purpose *in situ* X-ray (AMPIX) cells, because of its highly porous structure and excellent wettability [23]. As mentioned above, one additional challenge with using Li metal as anode is its predisposition to grow in highly uneven morphologies, particularly dendrites which could pierce the separator and lead to short-

circuit within the cell. A possible solution that is currently being pursued is to substitute the conventional liquid electrolytes with a stiff solid-state electrolyte such as glassy or ceramic inorganic compounds, or organic polymers [17]. In this case, the solid electrolyte can also act as separator. Arguably one of the most popular choices is the family of Li-stuffed garnet-type metal oxides, $Li_7La_3Zr_2O_{12}$ and compositional derivatives, with high Li-ion conductivity ($\sim 10^{-4}$ S·cm^{-1} at room temperature) and great chemical stability against both highly reducing Li and high voltage cathodes [24].

1.1.2 Cathode Materials for Lithium Batteries

1.1.2.1 Overview of Current Cathodes Materials for Lithium Batteries

There are two major groups of cathode materials studied for lithium batteries. The major difference between these two general classes of cathode materials is the mechanism of lithiation/delithiation: conversion and intercalation.

The electrodes made following conversion reactions undergo complete chemical rearrangement during lithiation/delithiation. Equation 1.7 is an example reaction using metal halides (MX_z, X = F, Cl) as cathode for Li batteries:

$$MX_z + yLi \rightleftharpoons M + zLi_{y/z}X \tag{1.7}$$

This type of cathode material has high theoretical capacities (e.g. theoretical capacity of $S_8\|Li_2S$ is 1675 mAh·g^{-1}), but they suffer from poor electronic conductivity (e.g. metal halides)
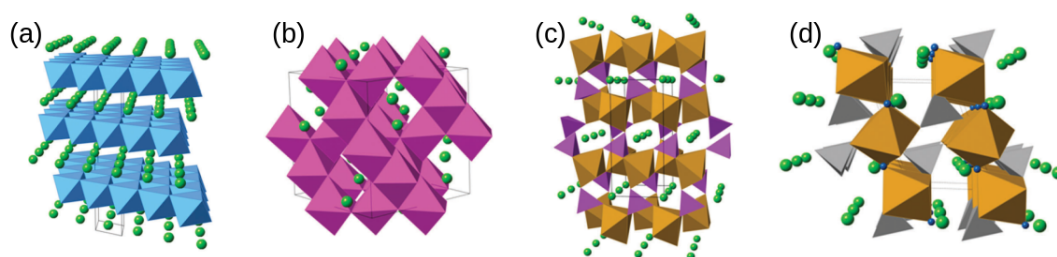
Figure 2. Representative crystal structures of intecalation cathode materials for lithim-ion batteries: (a) layered $LiCoO_2$; (b) cubic spinel $LiMn_2O_4$; (c) olivine $LiFePO_4$; and (d) tavorite $LiFeSO_4$. Li ions are shown as light green spheres, CoO_6 octahedra in blue; MnO_6 octahedra in mauve, Fe–O polyhedra in brown, PO_4 tetrahedra in purple, SO_4 tetrahedra in grey and fluoride ions in dark blue. Black lines demarcate one unit cell in each structure. Reproduced from [1] with permission. Copyright © The Royal Society of Chemistry 2014

of at least some of the components in the reaction, large volume changes, and, thus, broadly, their poor cycle performance makes them less competitive than intercalation cathodes [13].

An example reaction of intercalation mechanism was shown in Equation 1.1. Intercalation cathode materials can be divided into different families based on their crystal structures as shown in Figure 2 [1]. The most common structural types are layered, spinel, olivine and tavorite as listed in Table I with representative compounds [13]. All of these structures allow lithium ions to move in and out reversibly during charging/discharging with minimal structural rearrangement, i.e., topotactically.

Among intercalation cathode materials, olivine-structured or tavorite-type polyanion $(XO_4)^{3-}$ (X=S, P, Si, As, Mo, W) compounds have good thermal stability [13], but layered or spinel transition metal oxides are more competitive thanks to their higher theoretical specific capacity, as shown in Table I [13].

TABLE I. Characteristics of Representative Intercalation Cathode Compounds

Crystal Structure	Compounds	Specific Capacity(mAh·g^{-1}) (theoretical/experimental)	Average Voltage [25] (V)
Layered	$LiCoO_2$	274/148 [26]	3.8
	$LiNiO_2$	275/150 [27]	3.8
	$LiMnO_2$	285/140 [28]	3.3
	$LiNi_{0.33}Mn_{0.33}Co_{0.33}O_2$	280/160 [29]	3.7
	$LiNi_{0.80}Co_{0.15}Al_{0.05}O_2$	279/199 [30]	3.7
	Li_2MnO_3	450/180 [31]	3.8
Spinel	$LiMn_2O_4$	148/120 [32]	4.1
	$LiCo_2O_4$	142/84 [33]	4.0
Olivine	$LiFePO_4$	170/165 [34]	3.4
	$LiMnPO_4$	171/168 [35]	3.8
	$LiCoPO_4$	167/125 [36]	4.2
Tavorite	$LiFeSO_4F$	151/120 [37]	3.7
	$LiVPO_4F$	156/129 [38]	4.2

1.1.2.2 Transition Metal Oxides

Both layered and spinel lithium transition metal oxides have been extensively studied for lithium batteries. This thesis focuses on layered oxides considering their higher theoretical specific capacity compared to spinels, which makes them the premier choice for commercial applications.

$LiCoO_2$ was the very first commercialized layered transition metal oxide cathode. As with many transition metal oxides, $LiCoO_2$ has a high theoretical specific capacity (274 mAh·g^{-1}) [26]. Research on $LiCoO_2$ focuses on its limitations such as cost of raw materials, instability to fairly modest temperature excursions or capacity fading when more than 50% Li is cycled in and out of the structure [13]. A classical solution is to modify the composition by substituting Co by a combination of other transition metals.

LiNiO$_2$ and LiMnO$_2$ are examples that have been studied to completely substitute Co. Both LiNiO$_2$ and LiCoO$_2$ have very similar crystal structure and theoretical specific capacity (Table I), but compared to LiCoO$_2$, LiNiO$_2$ provides a lower cost as Ni is more abundant in the nature. However, LiNiO$_2$ still suffers from low thermal stability when cycling, driven by the fact that Ni^{3+} is readily reduced to Ni^{2+}, which tends to block the Li diffusion pathways by occupying Li$^+$ sites [39]. Compared to LiCoO$_2$ and LiNiO$_2$, LiMnO$_2$ is much cheaper and less toxic with even a slightly higher theoretical specific capacity, 285 mAh·g^{-1} [28]. The major concern with LiMnO$_2$ is a particularly poor cycling performance as the structure evolves from layered to spinel when Li is extracted and re-introduced into the oxide [40] and Mn is prone to corrosion by forming Mn^{2+}, which is soluble in the electrolyte [41].

Among the possible combinations of transition metals, those rich in Ni are considered one of the promising because they minimize Co contents, while preserving high capacity. Permutations like LiNi$_{0.80}$Co$_{0.15}$Al$_{0.05}$O$_2$(NCA) and LiNi$_x$Co$_y$Mn$_z$O$_2$ are some examples that have been studied and commercialized in the battery market. Keeping some Co helps preserve the power density of the electrode, whereas the additions of Al and Mn help to achieve a better cycling performance and a better thermal stability.

1.1.2.3 A Promising Cathode Material: LiNi$_{0.80}$Co$_{0.15}$Al$_{0.05}$O$_2$

In this thesis, the layered transition metal cathode material, LiNi$_{0.80}$Co$_{0.15}$Al$_{0.05}$O$_2$ (NCA) was studied. Compared to LiNiO$_2$, NCA has a better structural stability thanks to Co and Al. NCA is much cheaper than LiCoO$_2$ but with similar specific capacity, 279 mAh·g^{-1} [30]. As NCA is one of the most promising cathode materials, it has been studied extensively in
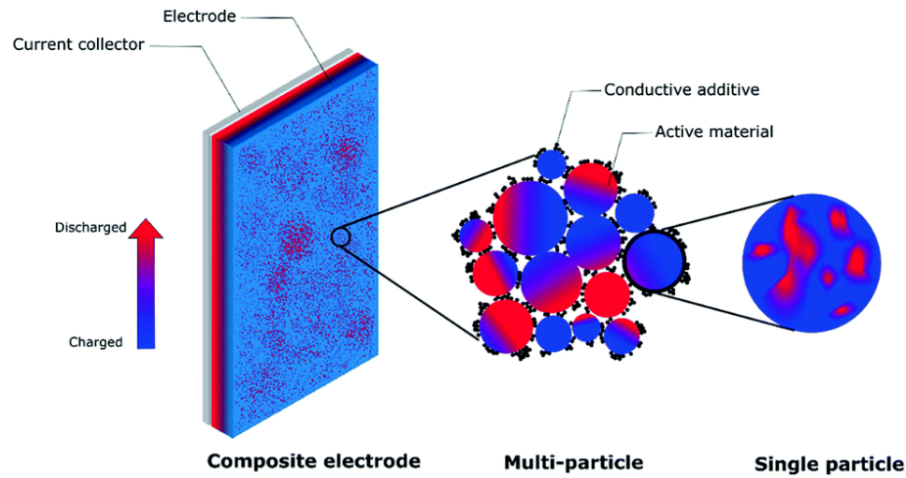
Figure 3. Heterogeneous State-of-Charge(SOC) distribution on cathode material at different length scales from the electrode level to the single particle level. The color code was used to represent different SOC state with blue color indicates a more charged state and the red color represents a more discharged state. Adapted from [2] with permission. Copyright ©The Royal Society of Chemistry 2019

the past. Some studies provided a good insight into the electrochemcial properties of NCA, such as the need for activation of its electrochemical rection reported by Robert *et al.* [8], long term capacity fading behavior discussed by Liu *et al.* [10] and the comparison of its thermal stability to LiFePO$_4$ by Golubkov *et al.* [42]. Some other studies explored different methods to improve the electrochemical performance of NCA such as doping Mn^{4+} and Ti^{4+} to manipulate the layer spacing to improve lithium diffusion kinetics during cycling [43] or using atomic layer deposition to limit surface phase transitions driven by Ni reduction at high voltage [44].

As reported by Zhang *et al.* [2], the advent of uneven charge distribution at both particle and electrode level, as shown in Figure 3, could limit utilization of the active material and

lead to local overcharge or overdischarge. Our work involved the development characterization methods to examine these effects on NCA, at both particle and electrode level. In this thesis, broadly, one of our goals has been to develop methods to further visualize the connection between microscopic properties of NCA and its macroscopic electrochemical performance as a cathode, with a particular focus on transport of charge both at the level of individual particles and complete electrode architectures.

1.1.3 Solid Electrolytes

The chemical reactivity of liquid electrolytes raises safety issues that result from electrolyte leakage and vaporization [45]. These safety concerns aggravate in the presence of a highly reactive anode, like Li metal. And they scale up in battery systems to power electric vehicles, which require substantially increasing size of the battery compared to portable electronics. One of the solutions proposed to eliminate these safety concerns resulting from using liquid electrolytes is to build up a lithium battery with solid electrolytes.

As mentioned above, Li-stuffed garnet-typed metal oxides, $Li_7La_3Zr_2O_{12}$ (LLZO) and compositional derivatives, constitute a promising candidate family of solid electrolytes for future lithium batteries. Particularly, their cubic phase (with space group Ia-3d) has high ionic conductivity (10^{-4} S·cm^{-1} at 298 K), which is two order magnitude higher than their tetragonal counterpart (with space group of I4$_1$/acd) [46] and electrochemical stability compared to other solid electrolytes. Current studies on LLZO focus on aspects of material synthesis, cation doping, structure characterization, Li$^+$ transport mechanism and improvement of conductiv-

ity [47–49]. These studies suggested the conductivity of LLZO is very sensitive to even a small change in composition and microstructure.

One of the biggest challenges of LLZO is its air stability. When exposed to ambient conditions, $Li_7La_3M_2O_{12}$ (M = Zr, Sn, Hf) was reported by Kang *et al.* [50] to undergo the following chemical reactions,

$$2\,Li_7La_3M_2O_{12} + 7\,H_2O \rightleftharpoons 14\,LiOH + 3\,La_2O_3 + 4\,MO_2 \tag{1.8}$$

$$2\,Li_7La_3M_2O_{12} + 7\,CO_2 \rightleftharpoons 7\,Li_2CO_3 + 3\,La_2O_3 + 4\,MO_2 \tag{1.9}$$
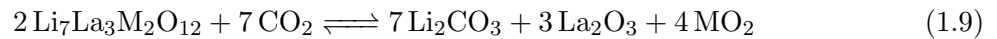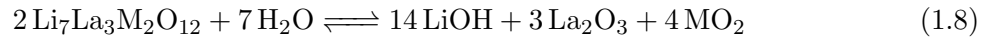
While these reactions are mostly constrained to surface domains, the formation of Li_2CO_3 leads to degradation of ionic conductivity and, thus, increased interfacial resistance. The air stability can be affected by synthetic and storage conditions. Researchers are trying to overcome these issues through mechanical polishing [51], doping [52] and new synthesis methodologies that protect surfaces from extensive contact with air [53]. The LLZO-type solid electrolytes studied in this thesis were examples which were doped with Ta and Al at the Zr and Li sites, respectively.

Another challenge for garnet-type solid electrolytes is the mechanical stress that results from the high sintering temperature (> 1200 °C) and long sintering process(> 10 h) required to produce dense membranes with high purity [54–56]. Nakatsumi *et al.* [57] have proposed that the presence of the strain created by mechanical stress could increase the charge transfer resistance but there was no clear mechanism reported. In this thesis, analysis of the local strain

was performed on membranes made of a few different LLZO-type solid electrolytes to evaluate the difference in electrochemical performance induced by sintering.

1.2   X-ray Diffraction

1.2.1   X-ray Source and Optics

In a laboratory setting, X-rays are usually produced by a sealed tube. A high voltage (V) is applied to accelerate the electrons emitted from a cathode to hit the metal anode to generate polychromatic radiation, including continuous radiation (white beam or *Bremsstrahlung* radiation) and several discrete characteristic radiation lines at different wavelengths based on the anode materials, λ, which can be described by,

$$\lambda = \frac{hc}{eV} \tag{1.10}$$

where h is Plank constant, 6.6264×10^{-34} J·s, c is the speed of light in a vacuum, $2.9979 \times 10^8 m \cdot s^{-1}$ and e is electron charge, $1.602\ 176\ 634 \times 10^{-19}$ C.

The two types of Bruker D8 series diffractometers in this thesis use the same type of X-ray source but with different optics. The X-rays were generated using an applied voltage of 40 kV to accelerate the electrons emitted from heated tungsten cathode to hit the copper anode. The generated X-ray source is a polychromatic radiation which includes three major characteristic radiation lines, $K_{\alpha 1}$ ($\lambda = 1.540562$ Å), $K_{\alpha 2}$ ($\lambda = 1.544390$ Å) and K_{β} ($\lambda = 1.392218$ Å) [3]. Monochromatic radiation is required for X-ray structural analysis. As the

most intensive characteristic radiation line, the doublet K_α radiation ($\lambda = 1.541838$ Å) was used.

Two different optics and geometries are presented in Figure 4 [3]. Both X-ray optics are designed to achieve the desired spectrum purity (monochromatic radiation), beam size and path of the beam. The Cu-K_β line can be blocked by using a monochromator or a nickel β-filter. The monochromator utilizes the diffraction properties of a crystal together with a knife-edge to allow the only desired radiation Cu-K_α go through, while the nickel β-filter can reduce the intensity of unwanted wavelengths by absorbing the X-rays emitted at the energies of interest.

The majority of modern X-ray diffractometers are built with a Bragg-Brentano geometry as shown in Figure 4 (a) [3]. The angles between sample and both incident and diffracted beams, θ, are the same with this geometry. The monochromator can be placed either after the X-ray tube, before the sample, or on the diffracted beam side, before the detector. The soller and divergence slits are used to control the axial and equatorial divergence of the incident beam, respectively.

The optics of a two-dimensional diffractometer are presented in Figure 4 (b) [3]. The basic principle of this instrument is to collect patterns of significantly smaller portions of the sample compared to a conventional powder diffractometer. To compensate for the loss of diffracted intensity of the spots sampled, either large arcs or a whole Debye diffraction ring of specific 2θ range are measured. In these instruments, the Bragg-Brentano geometry and soller slits are replaced by a setup where the angle of incident beam is fixed and the angle of detector is adjusted to collect patterns with different diffraction angles. In this setup, the monochromator
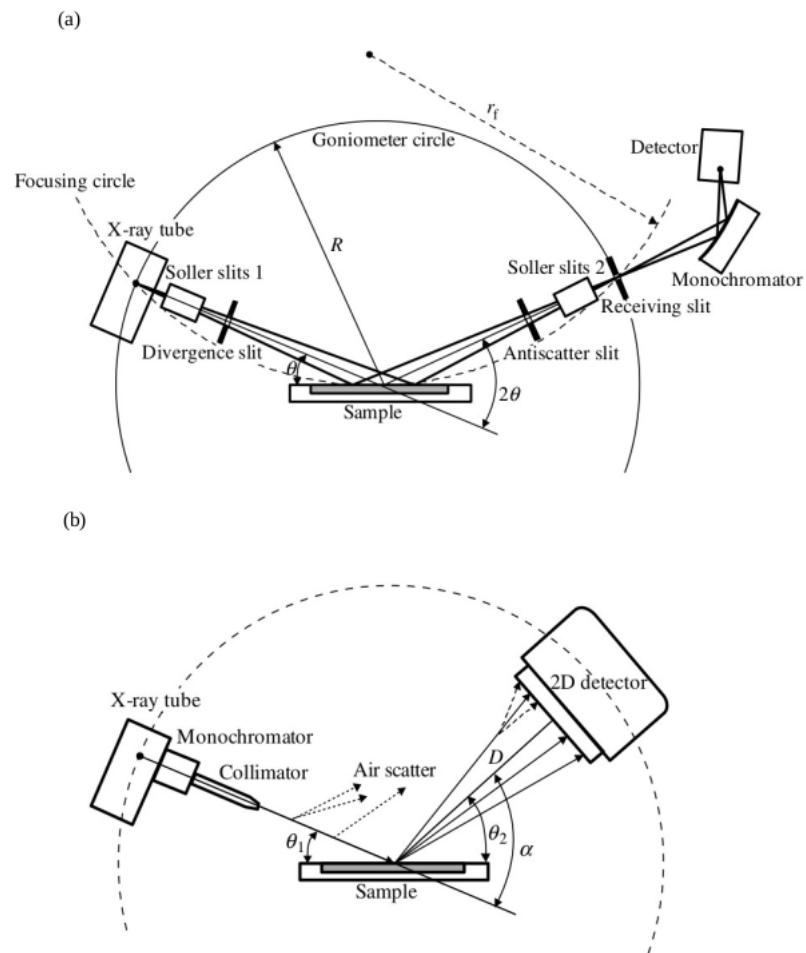
Figure 4. Schematic of X-ray geometries used in our laboratory instruments: (a) conventional X-ray diffractometer with Bragg-Brentano geometry, and (b) 2D X-ray diffractometer. Reprinted from [3] with permission. Copyright © 2009 John Wiley & Sons, Inc.
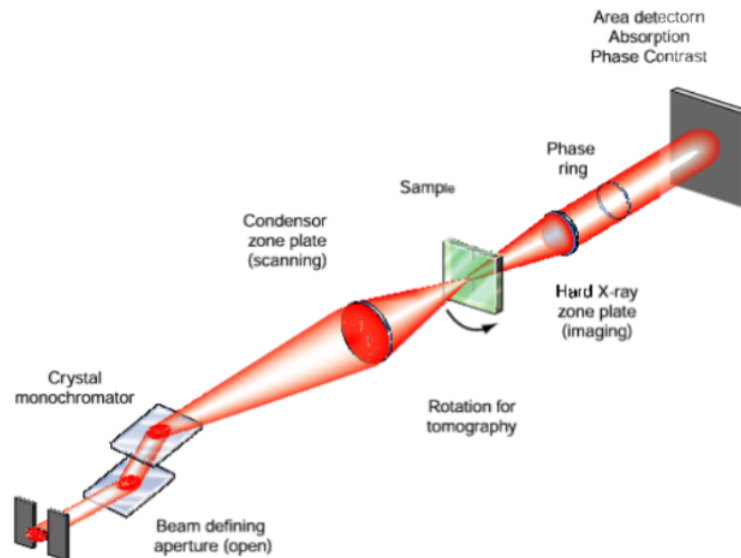
Figure 5. Scheme of experimental configurations using synchrotron hard X-ray microscopy imaging method with full-field transmission mode. Reprinted from [4] with permission. Copyright © 2005 Cambridge University Press

can only be placed at the source, coupled with a collimator to focus the monochromatic beam. A collimator is a cylindrical device to control the beam size and divergence. Pinhole-styled collimators were used for the mapping of cathodes described in Chapter 3 to obtain resolved diffraction patterns of discrete portions of the sample.

The beam source at a synchrotron is at much larger scale compared to a laboratory instrument. For example, Argonne National Laboratory hosts a 450-MeV accelerator of electrons at the Advanced Photon Source, in the shape of a ring with totalling 1104 m in storage circumference [58]. X-rays are emitted tangent to this ring, at so-called beamlines, at wavelengths that

can be tuned from sub 100 eV to over 100 keV, with fluxes much larger than from an X-ray tube. The fluxes make it possible to examine the crystal structure of samples even with beams focused at scales ranging from nanometer to micrometer, as presented in Chapter 4. The X-ray optics of this type of measurements performed at a synchrotron is shown in Figure 5 [4]. Measurements in transmission geometry are possible, in contrast to reflection for laboratory X-ray measurements. The transmission mode takes advantage of the great penetrating capability of high-energy X-rays at synchrotrons to record diffraction patterns. This imaging method allows the user to locate individual particles of interest, and scan the beam on spots on the particle to record structural information with a 2D detector (e.g., charge coupled device).

A synchrotron facility can also provide a tunable polychromatic X-ray beam (white beam), the X-ray source for energy dispersive X-ray diffraction. Such white beam can be used to study structural properties such as deviotoric strain, as presented in Chapter 5.

1.2.2 Crystal Structure

X-ray diffraction is a reliable analytical tool to study crystalline materials. The atoms of crystalline materials are arranged in a repeated pattern. The smallest repeating element in the lattice is called unit cell. Unit cells are categorized into seven crystal systems which can be described with six parameters: a, b, c define the crystallographic axes and α, β, γ describe the angles between the axes.

Three crystal systems will be discussed in this thesis as shown in Table II. The X-ray is diffracted by the atoms in a lattice plane where they are all ordered. The distance between adjacent parallel lattice planes that are equivalent by symmetry is described as d-spacing. The

TABLE II. Crystal Structures of the Materials Studied in This Thesis

Crystal Systems	Unit Cell	Example Material	Chapter
Cubic	$\alpha = \beta = \gamma = 90°$, $a = b = c$	$Li_7La_3Zr_2O_{12}$	5
Tetragonal	$\alpha = \beta = \gamma = 90°$, $a = b \neq c$	$Li_7La_3Zr_2O_{12}$	5
Hexagonal	$\alpha = \beta = 90°, \gamma = 120°$, $a = b \neq c$	$LiNi_{0.80}Co_{0.15}Al_{0.05}O_2$	3,4

fraction intercepts by which the planes intersect the crystallographic axes of the unit cell are denoted as *1/h, 1/k* and *1/l*, which can be used to describe the lattice plane from its Miller indices (*hkl*). For example, peak (003) of NCA discussed in Chapter 4 refers to the X-ray diffraction signal collected on the family of (003) lattice planes.

1.2.3 <u>Bragg's Law</u>

When using X-ray diffraction to study crystalline materials, the patterns are collected based on the diffraction signals that satisfy Bragg's diffraction condition,

$$n\lambda = 2dsin\theta \tag{1.11}$$

where, n is the order of the reflection, λ is the wavelength of the incoming X-rays, d is the spacing between equivalent lattice planes and θ represents the angle of incidence of the diffraction beam as shown in Figure 6 [3].

Usually, $n=1$, the first-order reflection from the fundamental energy is used in the study with monochromatic powder X-ray diffraction. The XRD signal from a perfect crystal structure is a vertical line (called delta function [3]) as shown in Figure 6 (b). Due to instrumental limitations
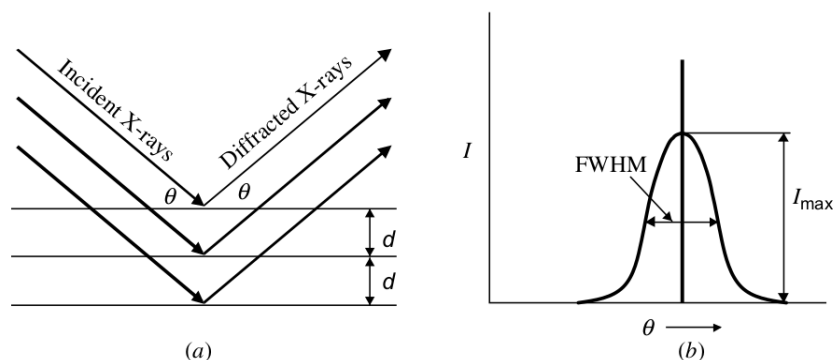
Figure 6. (a) Scheme of X-ray diffraction on lattice planes and (b) An example of diffraction peak observed at the Bragg angle θ. Reprinted from [3] with permission. Copyright © 2009 John Wiley & Sons, Inc.

to angular resolution, the XRD signals are usually observed as a broadened symmetric peak rather than a vertical line. The peak can be described by its diffraction angle θ, intensity, I and shape of the peak, including its full width at half maximum (FWHM). The collection of Bragg reflections is unique to one of the crystal systems above with a given symmetry and set of cell parameters. Therefore, it can be used to identify crystalline compounds in a sample.

Measurements of Bragg powder diffraction with monochromatic X-ray radiation are widely applied in solid state chemistry. However, in order to provide three dimensional structural

information of a single crystalline or polycrystalline material, advantages can be gained with polychromatic radiation (white beam), based on the established Laue equations,

$$a(\cos\psi_a - \cos\phi_a) = h\lambda$$
$$b(\cos\psi_b - \cos\phi_b) = k\lambda \qquad (1.12)$$
$$c(\cos\psi_c - \cos\phi_c) = l\lambda$$

where, a, b, c are the dimensions of unit cell, ψ and ϕ are the incident and diffracted angle of the beam on the corresponding dimensions, h, k, l are the order of the reflections of equivalent n in Equation 1.11. The polychromatic radiation provides a beam source with a range of wavelengths, λ, which makes it achievable to index a (hkl) spectrum where all of three equations are satisfied simultaneously. The number of μXRD diffraction signals are limited in materials with large grain size or with preferred crystal orientation. With a wider energy range, polychromatic beam provides an advantage to efficiently collect as many as reflections with different orders, n. Moreover, it also allows to acquire spatially resolved diffraction data without rotating the sample.

1.3   Application of X-ray Diffraction for Li Battery Study

This thesis is motivated by the applications of X-ray diffraction for Li battery studies. Powder X-ray diffraction has been widely used for this purpose, especially the components with crystalline materials. The XRD patterns provide the crystal structure of the material, based on the peaks with corresponding 2θ position where the Bragg law is satisfied. The material can be matched to its XRD pattern through a comprehensive database (e.g., the Powder Diffraction

File, PDF maintained by International Center for Diffraction Data, ICDD). For intercalation cathode materials, their crystal structure could be changed during cycling as the movement of Li ions changes d-spacing, which can be observed in the XRD patterns through a change of peak position after (*ex situ*) or even during galvanostatic cycling (*operando*). In many battery studies, the evolution of lattice parameters is related to the state of (de)lithiation of the cathode material. For example, Robert *et al.* [8] produced plots of lattice cell parameter for different x values in $Li_{1-x}Ni_{0.80}Co_{0.15}Al_{0.05}O_2$. If the kinetics of charge transport is uniform across the entire cathode, in other words, every single spot on the cathode has the same state of charge (SOC), the same unique XRD pattern could be obtained throughout the sample. If the SOC is not evenly distributed across the cathode, the XRD patterns will vary locally and even include varying mixtures of multiple phases that denote the reaction is not complete. The same effect can be found at the particle level; for example, chemical heterogeneity within a charged and discharged $LiCoO_2$ particle was visualized using *in situ* transmission X-ray microscopy (TEM) by Xu *et al.* and an example of uneven phase distribution is presented in Figure 7 [5]. Peak splitting or peak broadening can be observed as a result of the overlap of the phases. This concept is fundamental to chapters 3 and 4, to study the phase transition and kinetics of $LiNi_{0.80}Co_{0.15}Al_{0.05}O_2$ during/after cycling.

The crystal structure of a material not found in databases can still be studied through analysis of the XRD patterns, through an iterative process of modeling and fitting of the collection of signals known as refinement, to extract the space group, which denotes the specific symmetry of the lattice, as well as the lattice parameters. As XRD is very sensitive to small
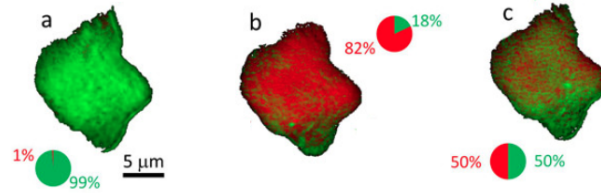
Figure 7. In situ transmission X-ray microscopy chemical heterogeneity maps of LiCoO$_2$ particles after being cycled at 1C rate: (a) pristine state, (b) charged to 4.6 V and (c) charged to 4.6 V, then discharged to 3V. The red and green areas represent charged and discharged domains, respectively. Adapted from [5] with permission. Copyright © 2017 American Chemical Society

alterations of the lattice spacings, it can be applied to investigate the deformations induced by stress from an external force or the existence of residual stress and deviatoric strain from internal forces in the material, imposed, for instance, by specific fabrication methods, with Laue X-ray diffraction, as exemplified in Chapter 5.

CHAPTER 2

EXPERIMENTAL APPROACH

2.1   Materials of Study

2.1.1   Cathode Material: $LiNi_{0.80}Co_{0.15}Al_{0.05}O_2$

Commercial $LiNi_{0.80}Co_{0.15}Al_{0.05}O_2$ was used as the cathode material of interest in this work. This material is manufactured by TODA KOGYO Corporation. Laminates of NCA were provided by the Cell Analysis, Modeling, and Prototyping (CAMP) Facility at Argonne National Laboratory (ANL). These laminates were designed to meet industry specifications of high energy density in the final Li-ion device. They consisted of 90.0 wt% active material, Toda NCA, 5.0 wt% Timcal C-45 and 5.0 wt% Solvay 5130 polyvinylidene fluoride (PVDF) binder. The cathode was coated on a metal Al foil. The coating thickness was 33 μm and the thickness of Al foil was 20 μm. The porosity of the cathode was 35.3%.

Experiments to elucidate insight into individual particles required the design of custom electrodes with a low concentration of active material to avoid spatial overlap. Diluted NCA cathode tapes were provided by Dr. Nathalie Pereira from the Energy Storage Research Group at Rutgers University. Each cathode tape was consisted of 20% activate material, 20% carbon black and 60% PVDF binder with an average thickness of 30-35 micron. The free standing pieces were cast on mylar for easy transportation.

TABLE III. LLZO Samples Examined by Laue X-ray Diffraction

Sample	Sample Components	Chemical Formula	Thickness (mm)	Shape of Measured Area
1	Al-LLZO pre-annealed	$(Li_{6.26}Al_{0.24})La_3Zr_2O_{12}$	1.24	Quadrant
2	Al-LLZO post-annealed	$(Li_{6.26}Al_{0.24})La_3Zr_2O_{12}$	1.18	Strip
3	Ta-LLZO hot-pressed	$Li_{6.5}La_3(Ta_{0.55}Zr_{1.45})O_{12}$	0.75	Quadrant
4	Al-LLZO hot-pressed	$(Li_{6.26}Al_{0.24})La_3Zr_2O_{12}$	1.04	Quadrant

2.1.2   Solid Electrolyte: $Li_7La_3Zr_2O_{12}$

Four samples were received from the group of Prof. Jeff Sakamoto at University of Michigan as shown in Table III. All samples were received in the shape of a disk with approximate average radius of 6 mm. Sample 2 was cracked into several smaller pieces during transport. The received samples were stored and manipulated in an Ar-filled glovebox. Annealing is a technique to induce grain growth by which the sample was heating without simultaneous application of pressure. Instead, $Li_7La_3Zr_2O_{12}$ was treated by hot-pressing (also known as pressure sintering), which refers to the simultaneous application of heat and uniaxial pressure during densification.

2.2   Powder X-ray Diffraction

A Bruker D8 Advanced, equipped with Cu-K_α radiation, was used for PXRD measurements at wavelength $\lambda = 1.5418$ Å. These measurements average over a large portion of the sample, thus being representative of the bulk. Where needed, samples were mounted in an enclosed holder transmissive of X-rays and sealed with an o-ring to prevent exposure to air during the measurement. Mounting was carried out in an MBraun Ar-filled glovebox. The measurements

were performed at room temperature with the diffractometer tube set at 40 kV and 40 mA. The PXRD reflections were collected at 2θ angular range of $10°$ to $80°$ with $0.019°$ step size and exposure time of 0.5 s. GSAS-II was used to fit the patterns using the expected space group of the compound to extract unit-cell parameters, a method known as Pawley refinement [59].

In this thesis, this experimental method was applied to NCA cathodes after galvanostatic cycling presented in Chapter 3 and $Li_7La_3Zr_2O_{12}$ samples for strain analysis presented in Chapter 5. These measurements acted as a baseline analysis of chemical composition to compare with the detailed spatial insight provided by the microprobe methods.

2.3   Micro X-ray Diffraction

X-ray beams can be focused to display a small point footprint on the sample. Such small footprints, as in micro X-ray Diffraction (μXRD), make it possible to resolve signals from different beam-sized spots within the material of interest. Local XRD patterns can thus be collected at each spot that is hit by the beam to generate maps to visualize the distribution of chemical heterogeneity, or, if the beams are small enough, even advance the study of phenomena occurring at the level of individual particles.

In this thesis, lab-based μXRD was successfully used to study the distribution of heterogeneity within a cathode laminate, as demonstrated in Chapter 3 with $LiNi_{0.80}Co_{0.15}Al_{0.05}O_2$. In turn, synchrotron experiments at Argonne National Lab were employed to resolve and visualize phenomena occurring at individual secondary particles of NCA during cycling, as presented in Chapter 4. The same beamline was also used to probe local changes in deviatoric strain in solid-state electrolyte membranes composed of $Li_7La_3Zr_2O_{12}$ as described in Chapter 5.

A Bruker D8 Discover series 2, equipped with Cu-K$_\alpha$ radiation ($\lambda = 1.5418$ Å), was used for μXRD experiments conducted in our laboratory. The instrument has three different collimator sizes available: 0.3 mm, 0.5 mm and 0.8 mm. The angle of incidence of the X-ray beam on the sample was set to 50° to minimize the area that was illuminated. The diffracted signal was collected by a Våntec-500 area detector covering a fixed 2θ range of 20°. The detector was placed in a single position during the measurement to minimize acquisition times at the expense of not collecting patterns as wide as in conventional powder XRD. A custom-built open-source Python package, *scimap* [60], created by a previous member of our group, Dr. Mark Wolfman, was used for data acquisition and integration of the two-dimensional diffraction pattern via Bruker's GADDS. Selected diffraction of some spots were further investigated by GSASII using Pawley refinements [59].

Synchrotron μXRD was performed at 34 ID-E at the Advanced Photon Source, Argonne National Laboratory. The energy range of the beam source can be tuned between 7 and 30 keV, and the optics allow experiments with either monochromatic or polychromatic (white or pink) radiation. The beam size is 300 nm $\times$ 300 nm.

Two types of experiments were conducted at this beamline. Monochromatic Bragg XRD, comparable to the versions in our laboratory, was collected in transmission mode using a two-dimensional MAR 165 CCD detector. The sample was moved relative to the beam with 12 s of exposure time. The step size was determined by the size of the particles. The two-dimensional diffraction frames were integrated into one-dimensional patterns and subsequently analyzed using GSASII [59].
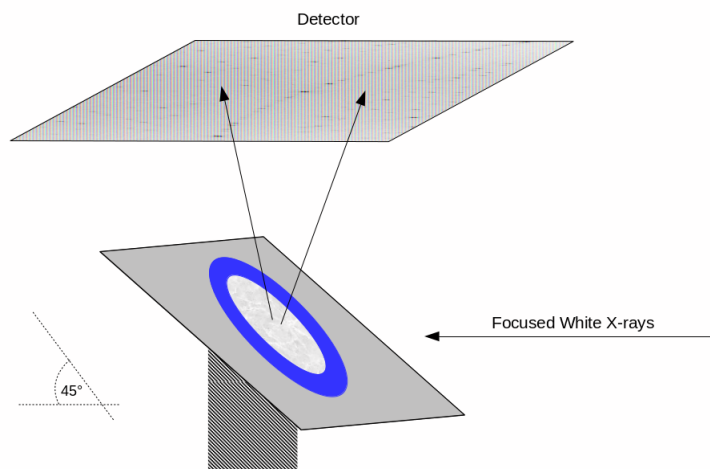
Figure 8. Experimental setup for Laue X-ray diffraction Measurements

The use of a polychromatic beam at 34 ID-E enabled the collection of μX-ray Laue Diffraction patterns. The experimental setup is shown in Figure 8. The sample was placed on an 45° inclined stand. A focused polychromatic beam with broad-bandpass radiation (white beam) was used to hit the surface of the sample with 20-100 μm penetration based on the material (in this work, it was calculated 20-30 μm based on the mass density of the samples). The diffraction was collected by a Perkin-Elmer XRD 1621 flat-panel detector. The area of interest in the sample was mapped with a scanning step-size of 50 μm. The axis system was aligned with the sample for analysis, with the x and y axis set as the horizontal plane of the membrane while z was the vertical axis normal to its surface, i.e., along its thickness. The collected reflections of Laue μX-ray diffraction patterns were automatically indexed with its crystal system via IGOR Pro, with the package LaueGo developed by APS.

After peaks were indexed, deviatoric strain analysis was carried out based on the measured peak positions to extract the actual ratio among a_x, a_y and a_z. The deviatoric strains in six directions can be studied as shown in the ε matrix:

$$\varepsilon = \begin{Bmatrix} \varepsilon_{xx} & \varepsilon_{xy} & \varepsilon_{xz} \\ \varepsilon_{yx} & \varepsilon_{yy} & \varepsilon_{yz} \\ \varepsilon_{zx} & \varepsilon_{zy} & \varepsilon_{zz} \end{Bmatrix}$$

where $\varepsilon_{xy}=\varepsilon_{yx}$, $\varepsilon_{xz}=\varepsilon_{zx}$ and $\varepsilon_{yz}=\varepsilon_{zy}$. In deviatoric strain measurements, the unit cell volume is assumed to be constant. A positive ε stands for deviatoric strain due to tension while a negative ε represents deviatoric strain due to compression. It should be noted that Laue X-ray diffraction is not sensitive to isotropic lattice compression or expansions. Therefore, the deviatoric strain of the lattice experiencing isotropic alteration is 0 in our measurement.

2.4   Electrochemical measurements

2.4.1   *Ex situ* Mapping of Ensemble Cathode

The study of battery cathodes in academic laboratories is typically conducted at constant current, i.e., galvanostatically. The laminates provided by CAMP were assembled into 2032-type coin cells in an Ar-filled MBraun glovebox with Li metal as anode, a polypropylene membrane (Celgard 2400) as separator and an electrolyte composed of ethylene carbonate (EC) and dimethyl carbonate (DMC), in 1:1 v/v ratio, as solvent and $LiPF_6$ as the solute (Novolyte Technologies). The cells were tested at different C/n rates, defined as fully charging the cell in n hours, using a cycler from BioLogic. All potentials in this thesis are referred to the Li^+/Li^0 couple. Once the electrochemical experiment was complete, the NCA cathode was harvested from

each coin cell and washed with DMC in the Ar-filled glovebox to remove electrolyte residues for XRD analysis.

2.4.2 *Operando* Mapping of Secondary Particles

The Argonne's multi-purpose *in situ* X-ray (AMPIX) cell presented in Figure 9 [6] was used for *operando* experiments in this work. AMPIX is designed to conduct electrochemical cycling while allowing transmission of X-rays, unlike conventional coin cells. The battery cavity consists of the same basic arrangement of components as in coin cells, as shown in Figure 9 (c). The X-ray transmissive windows designed at both sides of battery cavity provided a pathway of X-ray to go through. Lithium metal was used as counterelectrode attached to a copper current collector. A window-sized (d=3 mm) hole was cut in the center of the copper sheet and covered by a polymide film (Kapton) to allow the penetration of the beam. A glass fiber separator was used in this work, with the same electrolyte as in coin cells. The working electrode was a diluted NCA tape provided by Rutgers University. The AMPIX cells were assembled in an Ar-filled MBraun glovebox.

Operando mapping was performed at beamline 34 ID-E. The Bragg XRD measurements were conducted in transmission geometry. The location of individual secondary particles was determined using fluorescence imaging at the Ni K_α emission line, at approximate 8 keV, at an area of 100 μm $\times$ 100 μm. We targeted particles that were isolated from the rest, without any spatial overlap. The X-ray microbeam was rastered across a region of interest where a particle of interest was located, including part of its surroundings to define the contour appropriately. The AMPIX cell was connected to a BioLogic VMP3 cycler for galvanostatic cycling. The
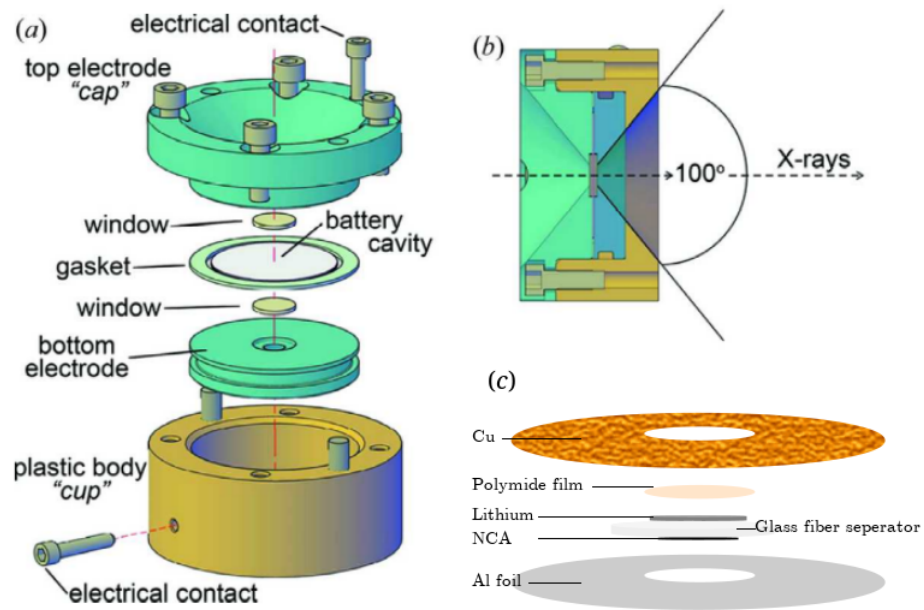
Figure 9. (a) Schematic of an AMPIX electrochemical cell, (b) the assembled AMPIX cell and (c) the cell layers stacks in this work. (a) and (b) were reproduced from [6] with permission of the International Union of Crystallography

measurements were conducted at multiple rates. At slower C rate, i.e. C/8, three particles could be mapped at the same time. Faster C rates, i.e. C/3, only allowed one particle to be examined per cell to ensure sufficient time resolution in the experiment. Since diffraction signal arises from all components in a transmission measurement, the strong reflections from lithium particles in the Debye diffraction ring manifested in high intensity spots which had to be masked out before further analysis.

<center>CHAPTER 3</center>

<center>SURFACE IMPURITIES AFFECT MACROSCOPIC TRANSPORT IN</center>

<center>LiNi$_{0.80}$Co$_{0.15}$Al$_{0.05}$O$_2$ CATHODES</center>

The content of this chapter is based off a manuscript in preparation: Li,C., Wolfman,M., May, BM.and Cabana,J.: Surface Impurities Affect Macroscopic Transport in LiNi$_{0.80}$Co$_{0.15}$Al$_{0.05}$O$_2$ Cathodes

3.1 <u>Introduction</u>

As a promising cathode material, the performance of LiNi$_{0.80}$Co$_{0.15}$Al$_{0.05}$O$_2$ has been studied extensively in past years [9, 61–64]. One of the studies carried out by Kazutoshi *et al.* [65] proposed that the surface of NCA is not stable in ambient atmosphere, leading to impurities such as Li$_2$CO$_3$ following the reaction,

$$\text{LiNi}_{0.80}\text{Co}_{0.15}\text{Al}_{0.05}\text{O}_2 + \frac{1}{4}x\text{O}_2 + \frac{1}{2}x\text{CO}_2 \longrightarrow \text{Li}_{1-x}\text{Ni}_{0.8}\text{Co}_{0.15}\text{Al}_{0.05}\text{O}_2 + \frac{1}{2}x\text{Li}_2\text{CO}_3 \quad (3.1)$$
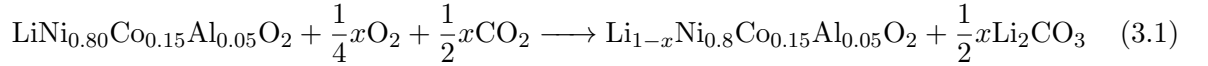
Zhuang *et al.* [66] further stated that NCA particles are electrically isolated from the battery circuit by the presence of Li$_2$CO$_3$, which leads to both capacity and power losses. The study provided a comprehensive understanding of the effect of this impurity on accessible capacity and the rates at which the NCA cathode cycled. However, it left a gap between the ensemble cathode and local changes in kinetics that could induce detrimental heterogeneity in the utilization of the electrode.

<center>33</center>

In this chapter, we evaluate the hypothesis that different storage conditions could induce different electrochemical performance of NCA cathodes, driven by the prevention of surface impurities associated with contact with air. We further hypothesize and verify that any differences in performance would be due to the formation of heterogeneity in how the reaction occurs within the charged NCA cathode. The distribution of different phases was mapped by μXRD in our laboratory, which provided insight into local effects of transport that link to the macroscopic response of the NCA cathode.

3.2   Experimental Methods

The NCA cathode laminates were separated into two sets subject to different storage conditions. One set was stored in an Ar-filled glovebox, labeled NCA-Ar. The other set was stored in the ambient laboratory atmosphere without any further controls, labeled NCA-air. All the XRD and electrochemical measurements were conducted as generally introduced in Chapter 2. In particular, all coin cells were assembled with a difference in the radius between the NCA cathode (r=0.75 inch) and the Li metal anode (r=0.25 inch) for the purpose of creating purposeful gradients in electrochemical kinetics along the lateral dimensions of the cathode, as described by Wolfman et $al.$ [7]. In brief, the alignment of the two electrodes with each other means that the reaction at the cathode is significantly favored at its center compared to its edge because of the different distances between these positions and the Li supply as shown in Figure 10 [7].
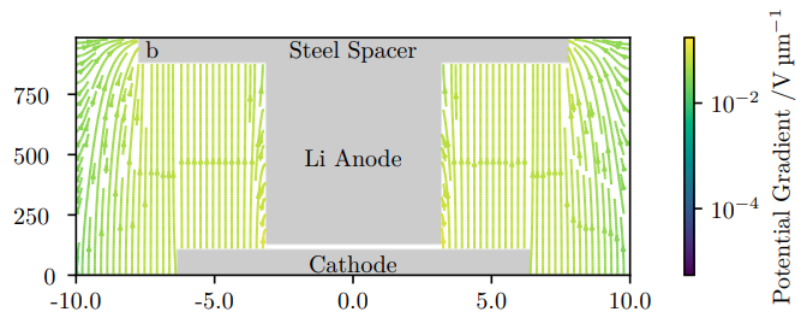
Figure 10. Streamlines in electric field within a coin cell with half-sized lithium metal anode. Reprinted from [7] with Permission of IOP Publishing Ltd. All rights reserved. Copyright © The Electrochemical Society

If transport within the cathode cannot rapidly redistribute Li, these gradient in Li supply will impose local kinetic limitations, as also observed by Wolfman *et al.* [7]. Likewise, any observed differences in electrode activity can be used to identify the existence of transport limitations. The cells were charged galvanostatically to 5.0 V at different C rates. The cells with NCA-Ar were tested at C rates of C/10, 1C and 5C (i.e., C/0.2) and the cells with NCA-air were tested at C/10, C/5 and C/2. The cells were open immediately after they stopped and the electrodes were harvested, dried and washed to prevent relaxation in the presence of electrolyte.

The NCA cathodes were measured *ex situ* after cycling by powder XRD. Phase analysis was performed by GSASII [59]. The lattice cell parameters, extracted from indexing the XRD
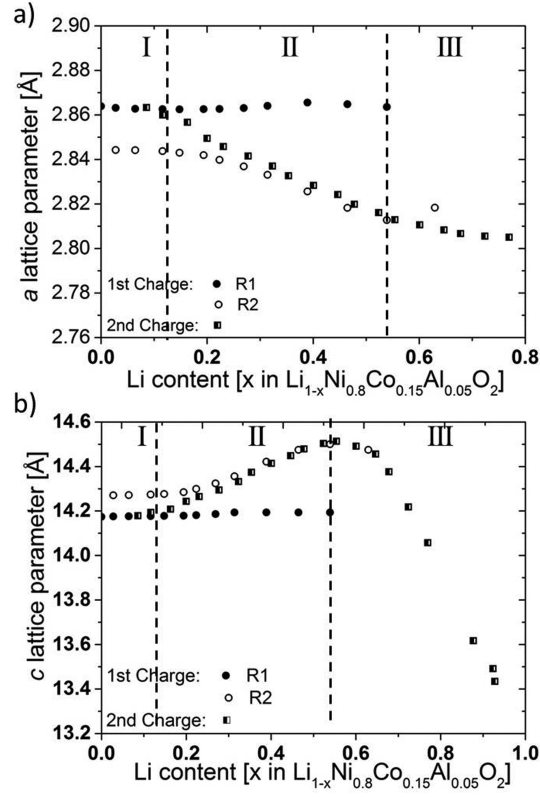
Figure 11. Lattice parameters (a) a and (b) c as a function of Li-content, x, in $Li_{1-x}Ni_{0.80}Co_{0.15}Al_{0.05}O_2$ for the first and second charge cycles extracted from *operando* synchrotron XRD data. Error bars are smaller than the symbols. Reproduced from [8] with permission. Copyright ©2014 American Chemical Society

patterns with a layered structure with R-$3m$ space group, were used to estimate the delithiation state, x in $Li_{1-x}Ni_{0.80}Co_{0.15}Al_{0.05}O_2$, based on the experimental data presented in Figure 11 by Robert *et al.* [8], extracted from *operando* PXRD analysis of homogeneous electrodes.

The value of x is between 0 to 1, where $x = 0$ represents the pristine state and $x=1$ represents the fully charged (delithiated) NCA cathode. The lattice parameter c is more sensitive to

changes in x, but its trajectory is not constant, changing direction at x=0.55. As a result, the lattice parameter a, which is less sensitive but largely decreases throughout, was used as a secondary probe when two possible values of x emerge from interpolating from c. For example, a c vaule of 14.49053 Å, coupled with an a value of 2.82424 Å, would be consistent with an estimated level of delithiation x=0.49 (Figure 11).

The cathodes were also measured by *ex-situ* μXRD. In this work, the measured 2θ angular range was 52-72° (corresponding to q range of 3.6 to 4.8 Å^{-1}), covering four NCA reflections: (107), (018), (110) and (113). The two-dimensional diffraction frames were integrated into one dimensional diffraction patterns using GADDS. The Python package, *scimap* [60], was used for background fitting of the one dimensional diffraction patterns using Chebyshev polynomials, as shown in Figure 12. Cell parameters were calculated by minimizing the sum-of-squares difference between observed and calculated peak positions as presented by Wolfman *et al.* [7] using

$$2\theta = 2\arcsin\left(\frac{\lambda}{2d}\right) \tag{3.2}$$

where, for hexagonal unit cell, d is determined by

$$\frac{1}{d^2} = \frac{4}{3}\left(\frac{h^2 + hk + k^2}{a^2}\right) + \frac{l^2}{c^2} \tag{3.3}$$

where, h,k,l is the Miller index of each crystallographic plane in the unit lattice. The cell parameter a extracted from these fits was used to build phase distribution maps. The one
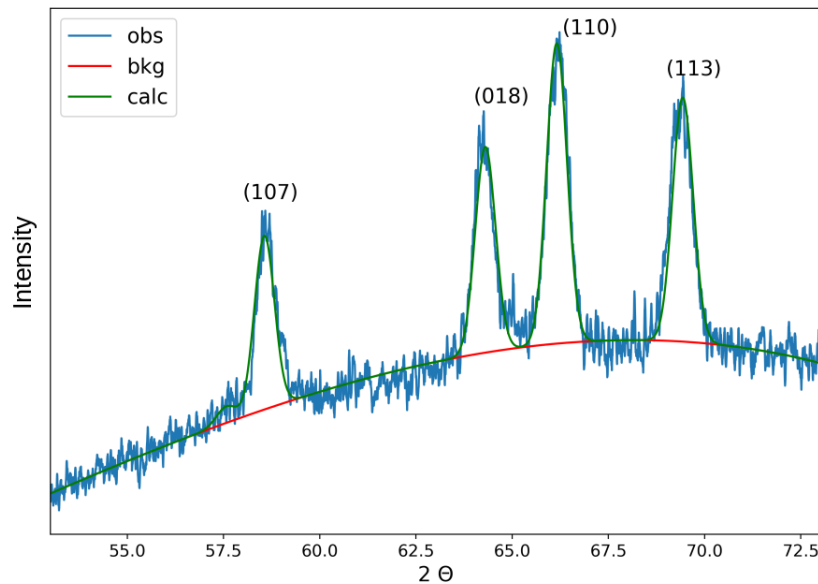
Figure 12. Example of Peak Fitting with Chebyshev polynomials where the red curve is the baseline of background, blue represents the actual data and green is the fitting curve calculated by *scimap*.

dimensional XRD patterns of selected spots showing evidence of multiple phases were further refined with GSASII to probe local phase heterogeneity [59].

3.3   Result and Discussion

3.3.1   Lithium Content Estimated From Cell Parameters

The powder XRD patterns of both pristine cathodes were normalized and presented in Figure 13, labeled with the theoretical reflections of NCA and Al foil. The observed difference in peak width was a result from the difference in the instrumental resolution due to the conditions of the measurement. All peaks could be indexed with the crystal structure of
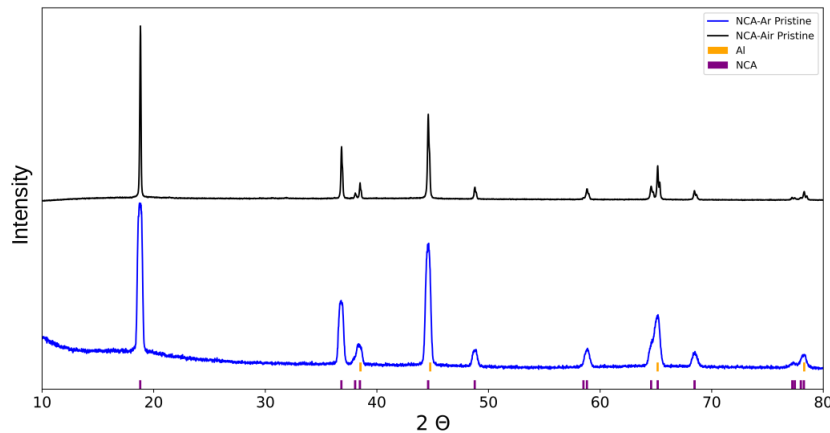
Figure 13. Powder X-ray Diffraction Patterns of pristine $LiNi_{0.80}Co_{0.15}Al_{0.05}O_2$ cathodes. The ticks indicated the positions of the predicted reflections of Al foil and $LiNi_{0.80}Co_{0.15}Al_{0.05}O_2$, according to the literature

$LiNi_{0.80}Co_{0.15}Al_{0.05}O_2$, with *R-3m* space group, indicating the absence of impurities observable above the limit of detection of XRD. It is worth noting that surface impurities like Li_2CO_3 would not be observable in this measurement. The *a* and *c* lattice parameters extracted from both patterns were very similar and agreed well with literature values (Table IV).

3.3.2   Homogeneous Delithiation of NCA-Ar Cathodes

The electrochemical profiles of NCA-Ar at different C rates (2C, 1C and C/10) when charged to 5.0 V versus Li^+/Li is presented in Figure 14 (a). Overall, NCA-Ar reached about 250 mAh/g at slower charging rates (C/10 and 1C) and 237 mAh/g at 2C. These values matches the literature of the gap between the theoretical capacity for full delithiation (279 mAh/g) and the experimental capacity (199 mAh/g) [30]. The experimental capacity reached in these

TABLE IV. Estimated Li Content x in $Li_{1-x}Ni_{0.80}Co_{0.15}Al_{0.05}O_2$ Based on Lattice Constants

Sample	a(Å)	c(Å)	x
NCA-Ar Pristine	2.865	14.189	0.00
NCA-air Pristine	2.863	14.194	0.00
Literature Pristine [8]	2.865	14.179	0.00
Literature Pristine [67]	2.865	14.181	0.00
NCA-Ar @ C/10	2.824	14.491	$\sim$0.49
NCA-Ar @ 1C	2.823	14.464	$\sim$0.44
NCA-Ar @ 5C	2.828	14.487	$\sim$0.48
NCA-air @ C/10 phase 1	2.811	14.104	$\sim$0.77
NCA-air @ C/10 phase 2	2.818	14.362	$\sim$0.68
NCA-air @ C/5 phase 1	2.834	13.778	$\sim$0.84
NCA-air @ C/5 phase 2	2.866	14.250	$\sim$0.18
NCA-air @ C/2 phase 1	2.823	14.009	$\sim$0.78
NCA-air @ C/2 phase 2	2.848	14.291	$\sim$0.26

measurements indicated that the cathodes had excellent performance despite the smaller Li anode. There was a spike in the voltage in the initial stages of charging at the two fastest rates, which is associated with the overpotential required to activate the process of delithiation. The spike gave way to a moderate decrease, and the expected progressive increase toward 5.0 V as lithium ions are transferred from the cathode to the anode. In the case of C/10, the potential smoothly increased without initial spikes.

Since full delithiation is expected to result in convergence of all domains of the electrode toward the end state, we explored the possibility of building heterogeneity due to transport when the reaction was only completed halfway. NCA-Ar was charged to 140 mAh/g ($\sim$50% state of charge, SOC) in the same type of cell with an undersized Li anode at different C rates (5C, 1C and C/2) as shown in Figure 14 (b). Similar spikes due to the activation overpotential
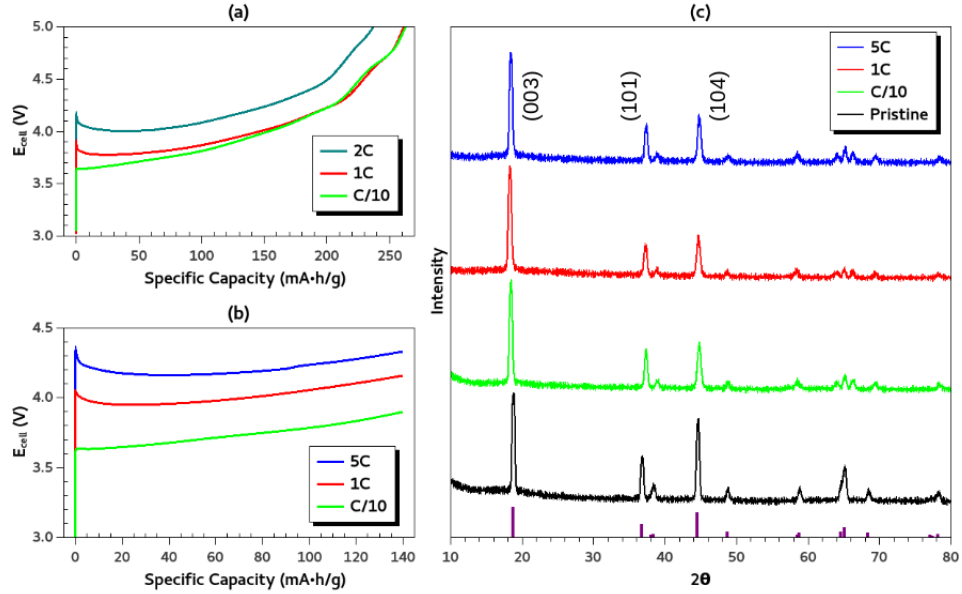
Figure 14. Galvanostatic charging curves and PXRD patterns of NCA-Ar cathodes in cells with half-sized lithium as anode. (a) E vs Q at different discharge rates after charging to 5.0 V. (b) E vs Q up to to 50% state of charge (SOC) at different discharge rates. (c) PXRD patterns of NCA-Ar charged to 50% SOC at different rates, compared to pristine.

as in Figure 14 (a) were observed at the fastest rates, with C/10 showing essentially no sign of it.

The composition of the charged NCA-Ar cathodes was analyzed by PXRD (Figure 14 (c)). All peaks in all XRD patterns could be indexed using a single unit cell with the same layered structure as $LiNi_{0.80}Co_{0.15}Al_{0.05}O_2$, without any extraneous signals. However, there was a change of the peak position between pristine and charged NCA-Ar. It indicated a structural change from delithiation. These changes were expected as the atomic structure has to accommodate the loss of Li. More specifically, the (003) peak shifted to lower 2θ while (101)

and (104) peaks shifted to higher 2θ compared to the NCA pristine PXRD pattern. The fact that a single unit cell was observed throughout is consistent with the fact that this transformation is expected to follow a single phase mechanism in Figure 11 [8]: when Li is removed from $LiNi_{0.80}Co_{0.15}Al_{0.05}O_2$, the a parameter drops from 2.86 Å to 2.82 Å, while c parameter initially increases from 14.2 Å to 14.5 Å, up until $\sim$50% SOC, then drops rather steeply up to full delithiation.

The fact that only one unit cell was sufficient to index the peaks was an indication that only one phase was detected for each charged NCA-Ar cathode. The unit cell parameters based on the fitting of the patterns with the layered framework (Table IV) were very similar at all three C rates, as expected from their similar capacities. The values of x estimated from the lattice parameters were in rather close agreement with the experimental capacity (50% SOC). The observations above indicate the electrodes were homogeneous after charging, indicating that there was no evidence of the differential kinetics within the electrode observed for $LiMn_2O_4$ in similar conditions, regardless of rates [7].

3.3.3 Heterogeneous Delithiation of NCA-air Cathodes

The electrochemical profiles of NCA-air when charged up to 5 V with different C rates (C/2, C/5 and C/10) are presented in Figure 15 (a), with the voltage window is from 3.5 V to 5.0 V versus Li^+/Li. All of these three samples required a much higher activation overpotential (above 4.5 V) to start electrochemistry compared to Figure 14 (a). There was an initial spike even at C/10. As observed in the study by Grenier *et al.* [9], the presence of an impurity layer on the surface of NCA (ambient condition in their study) correlates with a strong spike at the

beginning of the charging, which matches our observation of the increased overpotential for NCA-air in Figure 15 (a). The values of specific capacity of NCA-air at slow rates (C/5 and C/10) were similar, 166 mAh/g and 162 mAh/g respectively. However, as C rate increased to C/2, the charging capacity decreased to about 118 mAh/g, driven by a drastic increase in the overpotential required to reach the same SOC. The trend with rate was similar to NCA-Ar, but the capacities were much lower, which still reached 237 mAh/g at 2C compared to 168 mAh/g for NCA-air at C/2. Furthermore, even after the initial spike was overcome, the potential of NCA-air did not smoothly increase with SOC, as would be expected, but rather showed some oscillations that indicated significant sluggishness of the process. The stark difference in overall profile, activation overpotentials and achievable specific capacity suggested the electrochemical performance of NCA cathode was severely affected by exposure to ambient conditions, even though its bulk structure did not change.

The composition of NCA-air cathodes charged to 5 V, presented in Figure 15 (a), were analyzed by PXRD, shown in Figure 15 (b). While all peaks in the pristine state could be indexed with a single unit cell with a layered framework, there was notable splitting of peaks and appearance of shoulders after charge, which became most pronounced at C/2 and C/5. It is clear that the kinetic differences between electrodes manifested in a different extent of utilization and transport. Indeed, the presence of at least 2 different phases in an electrode when the thermodynamics of the transformation dictate a single phase mechanism can only be explained by the fact that not all domains in the electrode reacted at the same rate, let alone the overall rate imposed on the cell, in a similar behavior to previously reported for $LiMn_2O_4$
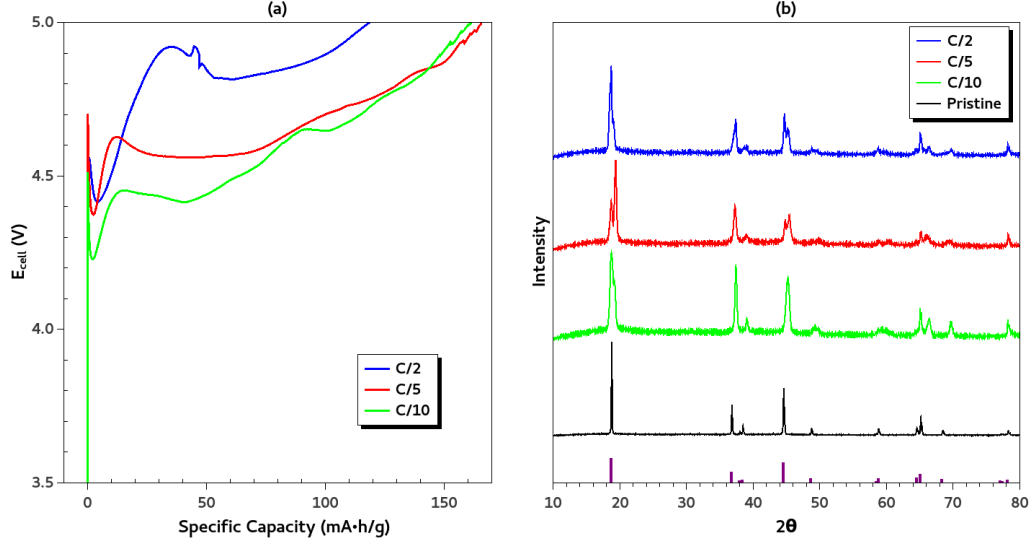
Figure 15. (a) Electrochemical profiles and (b) PXRD patterns of NCA-air charged at different C rates with half-sized lithium as anode.

in similar conditions [7]. The patterns could be successfully indexed with two different unit cells of the same space group ($R\text{-}3m$), but different lattice parameters (Table IV).

According to the calibration data, two values of x, approximately 0.77 and 0.68, were found in NCA-air at C/10 based on the cell parameters of two NCA phases, a= 2.810 Å, c= 14.104 Å and a= 2.818 Å, c= 14.363 Å, respectively. The values of x changed as the rates increased. At C/5, the cell parameters a= 2.834 Å, c= 13.778 Å and a= 2.866 Å, c= 14.250 Å (Figure 16 (a), goodness of fit, wR=5.9%) were corresponding to NCA phases with x=0.84 and x =0.18, respectively. The values were comparable at C/2: a= 2.823 Å, c= 14.009 Å and a= 2.848 Å, c= 14.291 Å (Figure 17 (a), goodness of fit, wR=8.4%) corresponded NCA phases with x=0.78
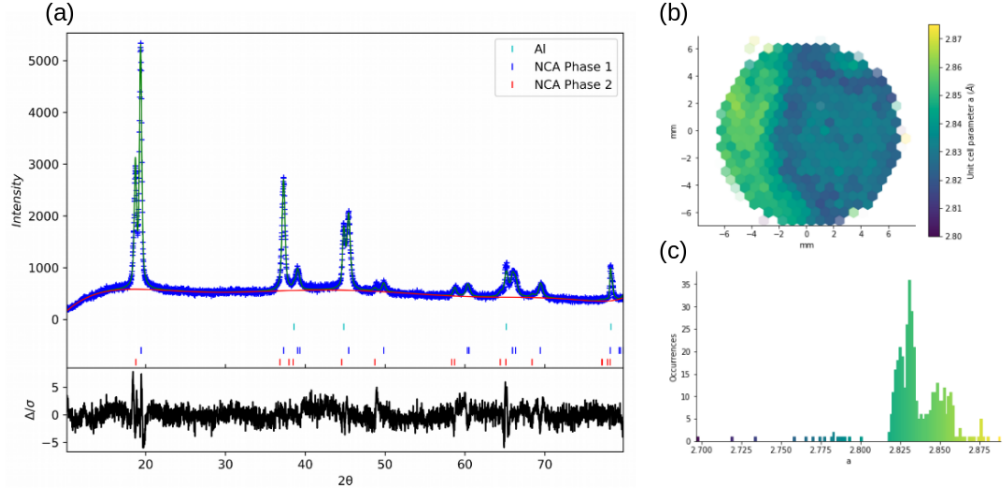
Figure 16. Phase Analysis of NCA-air charged at C/5 with a half-sized Li anode. (a) Fit of the PXRD pattern using two different unit cells with a layered framework, with R-$3m$ space group, and corresponding to two chemical states of $Li_{1-x}Ni_{0.80}Co_{0.15}Al_{0.05}O_2$ with different x; (b) Spatial distribution of phase parameter a in the electrode, extracted from μXRD; (c)Histogram of parameter a observed in the different μXRD patterns.

and $x =0.26$ respectively, but the phase with 0.26 was more predominant in the probed volume, based on the relative intensity of the peaks.

3.3.4   Phase distribution of NCA-air charged at C/5

The spatial distribution of the different NCA phases detected via PXRD in Figure 16 (a) was visualized through μXRD in Figure 16 (b). The histogram of the occurrences of parameter a, in Figure 16 (c), evaluates the relative occurrence of different unit cells. The histogram showed a rather bimodal distribution. As shown in Table V, the maxima in lattice parameter a were at 2.83 Å and 2.85 Å, respectively, in good agreement with the main values extracted from PXRD (Table IV). The histogram suggested that the phase distribution map was consistent

TABLE V. NCA-air Phase Evaluation (C/5)

	a(Å) from Bulk PXRD	a(Å) from Histogram
NCA-air phase 1	2.834	2.83
NCA-air phase 2	2.866	2.85

with analysis of PXRD, which averages over the bulk ensemble. When the different values extracted are mapped onto the electrode, it clearly shows a distribution of phases around the two maxima in the histogram over two large and distinct domains of the cathode. As can be seen, parameters around phase 1 (a around 2.830 Å) dominated the central region. It suggests that this region had higher levels of delithiation (around x= 0.84). In contrast, cell parameters closer to phase 2, which had lower level of delithiation state (x=0.18), were located in the edge regions, especially to the left. The distribution of delithiated states confirmed that the center of the electrode delithiated at a faster rate than the edges, even though a constant current was applied to the whole cell.

3.3.5 Phase distribution of NCA-air with C/2

The same analysis was applied to NCA-air charged rate at C/2 (Figure 17). The histogram was again bimodal, with maxima located at values close to the cell parameter measured by PXRD for phases 1 and 2 (Table VI). However, the distribution around the maximum at 2.82 Å was much narrower compared to 2.85 Å and both maxima at C/5. The width of the distribution at each maxima represents the slope of the chemical gradient between the respective regions. It is interesting that such chemical gradient is much steeper in regions with lower parameter
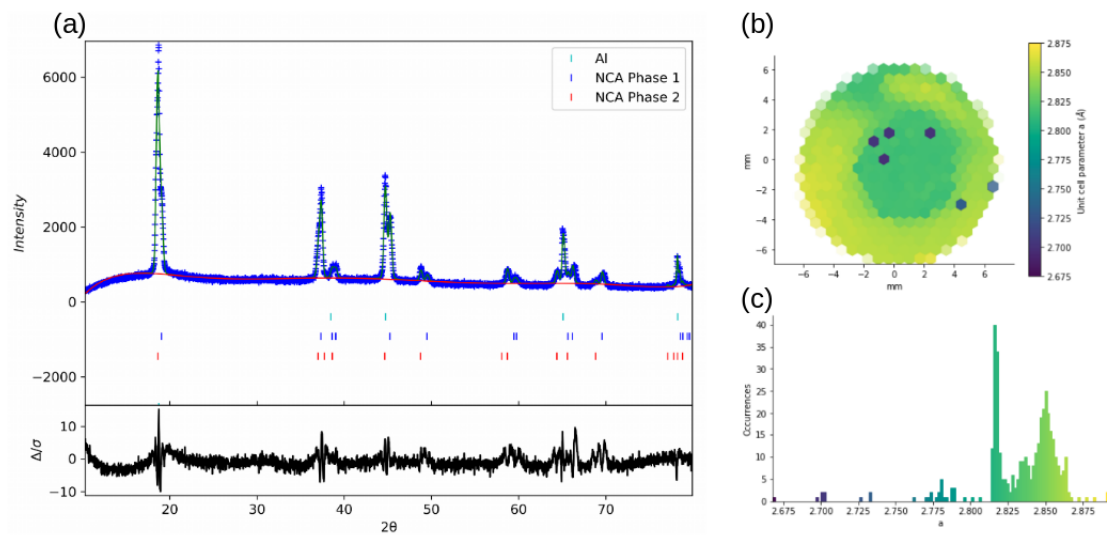
Figure 17. Phase Analysis of NCA-air cathode charged at C/2 with half-sized Li anode. (a) Fit of the PXRD patterns using two different unit cells with a layered framework, with $R\text{-}3m$ space group, and corresponding to two chemical states of $Li_{1-x}Ni_{0.80}Co_{0.15}Al_{0.05}O_2$ with different x; (b) Spatial distribution of phase parameter a in the electrode, extracted from μXRD; (c) Histogram of parameter a observed in the different μXRD patterns.

TABLE VI. NCA-air Phase Evaluation (C/2)

	a(Å) from Bulk PXRD	a(Å) from Histogram
NCA-air phase 1	2.823	2.82
NCA-air phase 2	2.848	2.85

a and, thus, higher levels of delithiation (x in $Li_{1-x}Ni_{0.80}Co_{0.15}Al_{0.05}O_2$). As with C/5, the regions with lower parameter a were clustered around the center of the electrode, with a clear delineation with regions with $a >2.83$ Å, leading to a concentric pattern, where the central domain had the same approximate diameter as the Li anode. This observation indicates that delithiation was preferential in the area of the cathode that was directly facing the anode in the cell, where Li ions transported faster than at the edges. These same effects were observed in similar experiments conducted with $LiMn_2O_4$ [7], suggesting a common limitation of transport within the electrode architecture, independent of the specific active material.

3.3.6   Phase Analysis of Local Spots on NCA-air with C/2

In order to get further insight into the local chemical distribution in NCA-air charged with a rate of C/2, spots were selected for further investigation, based on their locations in transition zones or where erroneous values of cell parameter were extracted by the automated algorithm (Figure 18). As discussed above, the algorithm was designed to treat each spot on the map as a single phase. A series of example patterns indexed with space group of *R-3m* can be found in Figure 18 (b) and their locations in the map is indicated in Figure 18 (a).
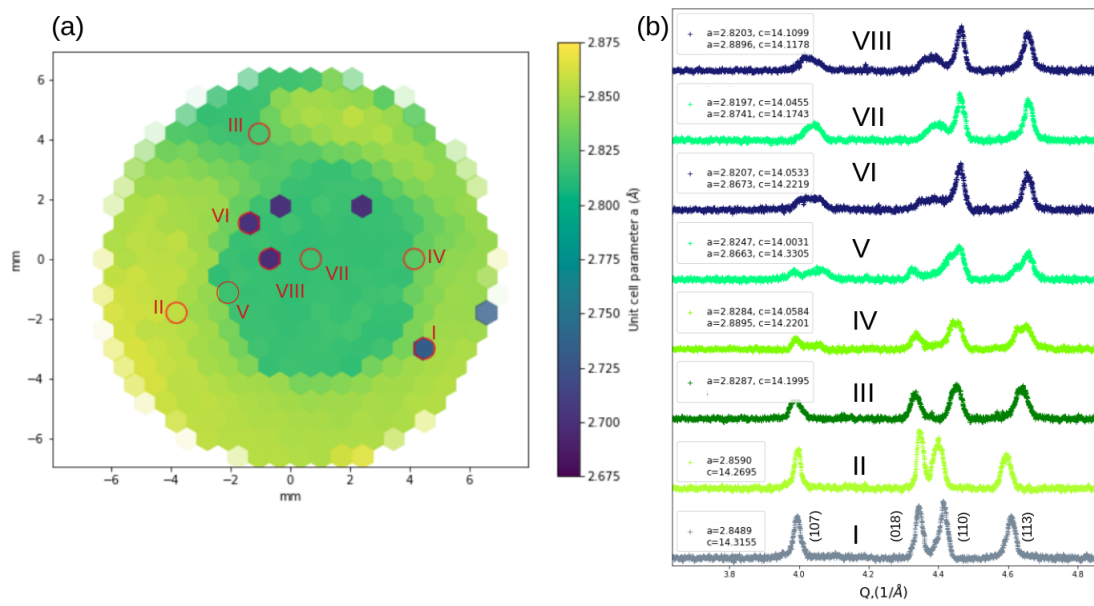
Figure 18. Phase analysis of selected spots on NCA-air cathode charged at C/2 with a half-sized Li anode. (a) Spatial distribution of phase parameter a in the electrode, extracted from μXRD; (b) XRD patterns of individual spots indicated in (a).
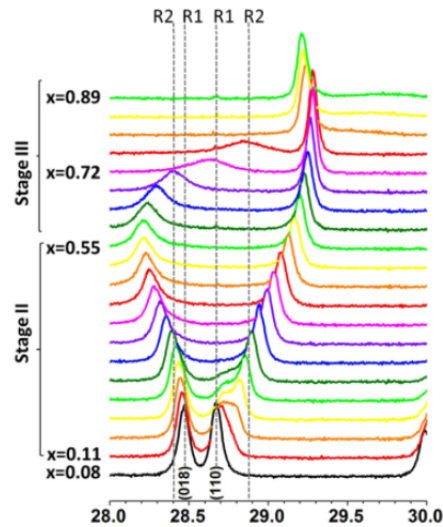
Figure 19. In situ synchroton X-ray diffraction patterns for the second charge for the (018) and (110) Bragg peaks of NCA, indexed with space group of $R\bar{3}m$. R1 and R2 denote two different rhomobohedral phases assigned during this transformation, whereas x denotes the amount of Li that is deinserted from $Li_{1-x}Ni_{0.80}Co_{0.15}Al_{0.05}O_2$. Reprinted with permission from [8]. Copyright ©2014 American Chemical Society

The cell parameters from the spots selected in the outer rim of lower delithiation levels (I and II) displayed evidence of a single layered lattice. There were small variations in cell parameters between spots, especially when the more sensitive c value was monitored, indicating that Li contents subtly changed locally even in this broader domain with lower reactivity. The lattice parameters of these spots were also slightly different from NCA phase 2, reflecting the deviations from the average revealed by the histogram in Figure 17. The results revealed an error in the fit of Spot I by the algorithm.

Spot III was selected because it was located in a domain in the outer region of the electrode, but where the algorithm assigned higher values of a than the rest of the edge. In the XRD pattern, reflections of a single unit cell were observed, but the distance between the peak (108) and (110) increased compared to I and II, which matches the trend reported in Figure 19 as Li ions are extracted during charging. This observation validated the assignment. The fact this general domain tended to show values similar to the center (NCA phase 1) rather than the outer region (NCA phase 2) indicates that the electrical field generally governing heterogeneity was disrupted. Similar effects were also found for $LiMn_2O_4$ [7], which was tentatively assigned to the fact that the pressure within the cell, which determines the distance between Li anode and oxide cathode, was not even laterally.

Spot IV and Spot V were located at the boundary area between the two general regions in the electrode. A complex lineshape was present in these patterns, with splitting of the (107) reflection. It suggested that at least two phases with different unit cell parameters NCA phases formed in spots at the boundary region. Fits of these spots with two phases, confirmed the existence of subdomains with different extents of delithiation, but it was dominated by a lattice with a=2.83 Å approximately, and, thus, high delithiation levels consistent with phase 1.

Spot VII is found at the opposite extreme of the chemical gradient, in the center of the electrode where phase 1 dominated. When this pattern was compared to the patterns presented in Figure 19, the selective broadening and position of the (108)/(110) reflections is consistent with the values of delithiation assigned based on the cell parameter of a single unit cell. The delithiation level of NCA Phase 1 was estimated as 0.78, which matches the range of composition

where such effects were observed in the reference data. Therefore, there was only one highly delithiated phase in Spot VII.

Spots VI and VIII were also assigned anomalous values of lattice parameter a, but, in this case, the origin was their complex lineshape, especially for reflections (007) and (108), which were smeared over a large enough range to indicate the existence of multiple unit cells with different dimensions. Fits with two different cell parameters resulted one of a values fell out of the theoretical range of NCA lattice parameters, which is also an evidence of compositional gradients within the spot more complex than bimodal.

3.4   Conclusion

Overall, the μXRD mapping demonstrated in this chapter, coupled with an electrochemical design with intentional gradients of supply of charge using half-sized Li anodes, provided a means to evaluate differences in transport between complete NCA cathodes by using structural analysis to visualize the heterogeneity of phase distributions in regions where it was deficient.

NCA samples subject to different storage conditions showed different electrochemical responses when using a half-sized lithium was used as anode. Our work suggested that when NCA was well protected from exposure to air, it was still able to maintain an uniform cycling performance (up to 5C) and overcome the barriers resulting from different local conditions. In contrast, the results with NCA-air emphasized the findings presented in previous research [66] where the formation of surface impurities severely affect macroscopic performance. Moreover, our study further revealed that the reduced accessible capacity when the impurity was present could result from different local conditions, inducing a distribution of different NCA compo-

sitional domains. Chemical maps of NCA-air charged at C/5 and C/2, collected by μXRD, revealed that the domains of the cathode closer to the lithium sink at the anode were delithiated more extensively. In other words, the presence of an impurity leads to different kinetics within the cathode as a response to gradients in electrochemical conditions imposed by the cell design. When the impurity is not present, in NCA-Ar, transport throughout the electrode is sufficient to compensate these gradients in carrier supply, leading to robust electrochemical performance and homogeneous utilization of the cathode during cycling.

The demonstration of chemical heterogeneity in NCA cathodes under these conditions could be extended to more realistic conditions where gradients are expected, for instance, due to imprecisions in cell assembly. It provides a good example for future studies that aim to investigate chemical heterogeneity through phase distribution under different electrochemical conditions, using a commercial instrument that does not require access to synchrotron user facilities.

CHAPTER 4

EFFECT OF CYCLING RATES ON THE PATHWAYS OF PHASE TRANSFORMATION OF SINGLE LiNi$_{0.80}$Co$_{0.15}$Al$_{0.05}$O$_2$ SECONDARY PARTICLES

4.1   Introduction

To meet the battery requirements from applications like EVs, closing the gap between the achievable and theoretical values of specific capacity of current electrode materials would substantially increase the energy density of the final devices. For example, the practical and theoretical specific capacity of LiNi$_{0.80}$Co$_{0.15}$Al$_{0.05}$O$_2$ [30] are ~200 and 279 mAh·g^{-1} respectively. A thorough understanding of the electrochemical reactions processes at the level of single particles may provide clues as to how to close this gap.

The phase transformation of LiNi$_{0.80}$Co$_{0.15}$Al$_{0.05}$O$_2$ during galvanostatic cycling has been extensively studied for the ensemble average of cathodes using powder diffraction. For example, the study from Robert *et al.* [8] reported three major stages of evolution of the diffraction peaks of NCA, correlated with specific delithiation states, illustrated in Figure 20 with diffraction peak (003) as an example. This reflection corresponds to the spacing between transition metal layers in the structure of the oxide as an example shown in Figure 2 (a) [1]. A single phase, solid solution mechanism was described in these three consecutive evolution stages. At Stage I, the (003) peak stays at the pristine position. Stage II was characterized with a peak movement

54
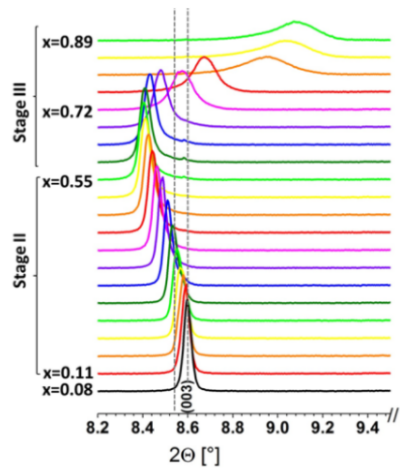
Figure 20. Evolution of the (003) diffraction peak of $Li_{1-x}Ni_{0.80}Co_{0.15}Al_{0.05}O_2$ ($\lambda = 0.7089$ Å) with correlated delithiation state, x, showing a constant evolution consistent with a single-phase, solid solution mechanism. Adapted from [8] with permission. Copyright © 2014 American Chemical Society

towards lower 2θ angle as the cathode continued delithiating up to $x=0.55$. According to Bragg's law, this change corresponds to an expansion of the spacing between layers due to the removal of Li ions between the layers. The associated decrease in positive charge reduces the screening between O^{2-} anions in different layers, which increases repulsion between them. The (003) reflection then started shifting to higher 2θ angle and broadened. The final position was substantially lower than the pristine state, indicating a significant collapse in the interlayer spacing, often ascribed to changes in the bonding and geometric interaction between O and the redox active metals, Ni and Co [68]. These observations of the changes in the bulk of an NCA cathode constitute the reference data to assess the pathways of phase transformation within NCA secondary particles in our study.

A previous study from our research group member, Dr. Brian May, measured the kinetics of phase transformation of $LiNi_{0.80}Co_{0.15}Al_{0.05}O_2$ secondary particles during the first galvanostatic cycle at a slow discharging rate, C/20, through *operando* X-ray diffraction mapping [11] using a synchrotron source at 34 ID-E beamline at Argonne National Laboratory. The data suggested that, at such slow rate, the evolution of the phase transformation was compositionally uniform within the particles. His work also uncovered a fascinating change in the rate of particle delithiation depending on the state of charge, despite the overall cell proceeding at constant current and, thus, rate. In order to investigate if this behavior is affected by the applied rate, here I demonstrate similar measurements with rates up to C/3. In addition, particles were also measured at different cycles with the same rate, which can be used to evaluate the change of electrochemical behavior for the particle during cycling lifetime.

4.2   Experimental Methods

The $LiNi_{0.80}Co_{0.15}Al_{0.05}O_2$ powders used in this study were composed of secondary particles with a hierarchical morphology, as illustrated in Figure 21(a) [9] with an example of scanning electron micrograph of NCA primary and secondary particles at pristine state Figure 21(b) [10]. The layered structure formed primary particles which were sintered into each other through grain boundaries and agglomerated to form the final secondary particles with spherical morphology. The size of the secondary particles ranged between 5 and 10 μm.

Operando μX-ray diffraction mapping of secondary particles was conducted on cathode tapes with a low concentration of $LiNi_{0.80}Co_{0.15}Al_{0.05}O_2$, using beamline 34 ID-E at the APS, as generally introduced in Chapter 2. In particular, in this work, four AMPIX cells were cycled
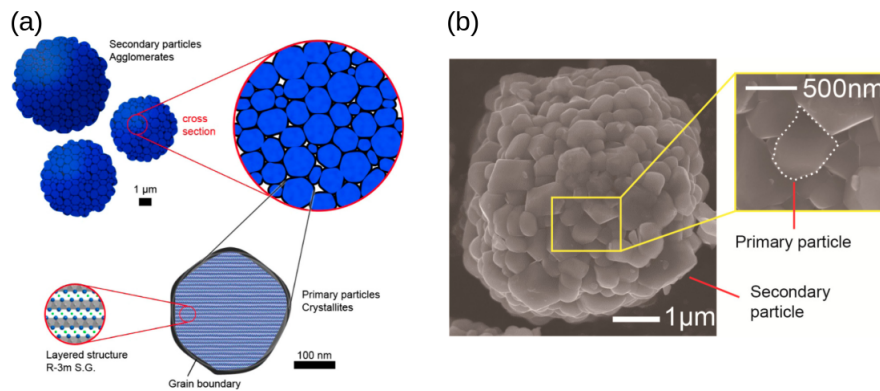
Figure 21. (a) The morphology of the NCA particles at different length scales. and (b) An example of scanning electron micrograph of NCA primary and secondary particles at pristine state. (a) was adapted from [9] with permission and (b) was adapted from [10] with permission. Copyright © 2017 American Chemical Society

galvanostatically between 4.7 V and 2.7 V versus Li^+/Li with two different C/n rates. The applied rates of each cell were listed in Table VII.

Cell I was initially charged at C/12, then accelerated to C/8 after 2 hours due to experimental constraints. It was discharged at C/8 once, then charged again at C/10. Three different particles were tracked in this cell, P1 to P3. Cell II was cycled multiple times at C/8, and 2 isolated particles were mapped (P4, P5). AMPIX Cell III and Cell IV were cycled with a faster C rate of C/3, and, as result, only one isolated particle could be mapped for each cell (P6 and P7 respectively) so that multiple states could be collected during each sweep. With the experimental time constraints at the APS, in order to compare the pathways of phase transformation of single NCA particles at different galvanostatic cycles with similar applied rates, the *operando* μXRD mapping measurement was started at different charging cycles for different cells. Mea-

TABLE VII. Cycling Rates employed for Operando Mapping of NCA Secondary Particles

Galvanostatic Cycle	Cell I	Cell II	Cell III	Cell IV
First Charge	C/12,C/8	C/8	C/3	C/3
First Discharge	C/8	C/8	C/3	C/3
Second Charge	C/10	C/8	C/3	C/3
Second Discharge	N/A	C/8	N/A	C/3
Subsequent cycles	N/A	C/8	N/A	C/3

surements in both Cell I and Cell III started at the first charge to study the electrochemical behavior of NCA particles to the end of second charge with different C/n rates. Cell II and Cell IV were employed to examine if NCA particles had similar electrochemical response in consecutive cycles at the same rates as Cell I and Cell III, respectively. The *operando* μXRD mapping for Cell II started at the end of second charge while Cell IV started at the beginning of second charge. These cells were cycled outside the beamline hutch prior to the μXRD measurements.

The number of particles mapped varied among cells due to the difference of applied rates, but it was always much smaller than the overall population, even in these dilute electrodes. The full map for a single particle took 24.2 min to acquire, defining the time resolution of the experiment. For Cell III and Cell IV, since only a single particle could be mapped at these fast rates, the process iterated from and back to the starting coordinate after collecting all 121 mapping positions, until the end of the targeted cycling process. When mapping multiple particles in a cell at slower rate, for example, in Cell I, complete maps were collected consecutively for each selected particles before iterating back to the first. The mapping stopped when the targeted charge/discharge cycles completed.
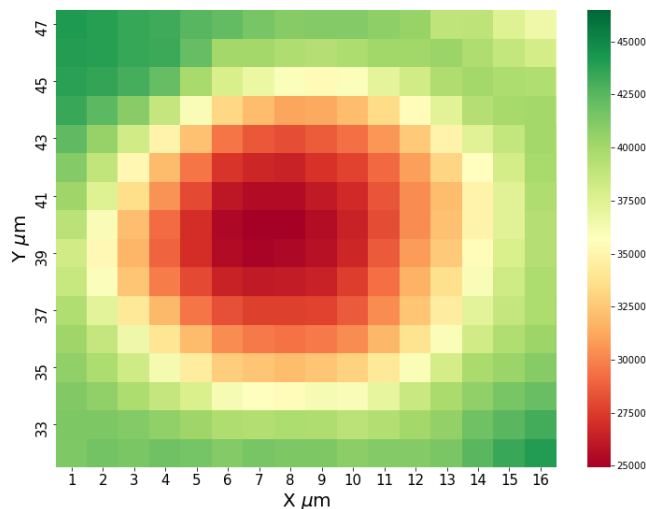
Figure 22. An example of a map of intensity at the Ni K$_\alpha$ emission line of NCA secondary particle P1. The red color represents a high concentration of Ni and the green color indicates the area surrounding the NCA particle.

After the particles were located by mapping the X-ray fluorescence at the Ni K$_\alpha$ line, as introduced in Chapter 2, a square scan was performed, as shown in Figure 22, to determine the starting coordinates of the XRD map, the approximate size of the particle as well as the step size required to capture a sufficient area. Considering the timing and convenience of data analysis, in order to collect as much reliable XRD data as possible, each particle was scanned with 11 × 11 (row × column) pixels corresponding to the size of the beam, meaning a map of one particle consists of 121 mapping positions. During XRD mapping, the sample was moved relative to the beam with exposure time of 12 s. At each exposure (mapping position), a 2D XRD pattern was obtained, an example of which is shown in Figure 23 (a). The collected

2D XRD patterns of each mapping position were analyzed using GSASII [59]. As shown in Figure 23 (a), the center position, marked with a blue $\times$, was determined through calibration with CeO_2 standards. The dash line in Figure 23 (a) shows the 2θ range (5-23°, $\lambda = 0.5166$ Å) for integration. The constrain of upper and lower 2θ limits are represented by green and orange circles, respectively. The white spotty signals represented the reflections from NCA particles. The diffuse white rings were background signals (i.e. from Kapton tape and glass fiber). As introduced in Chapter 2, the challenge of this method arises from the interfering signals of the lithium metal foil present in the cell as counterelectrode. The reflections from highly crystalline and oriented Li give rise to strong spotty signals on the 2D XRD patterns as shown in Figure 23 with dark red spots. The Li signals were masked out before integration of the 2D XRD patterns. The integrated 1D patterns with and without lithium being masked were presented in Figure 23 (b). The lithium peak was identified based on a reference pattern for metallic Li (PDF #00-001-1131). The integrated 1D patterns of each mapping position showing evidence of NCA reflections (as opposed to the surrounding electrode area with no NCA signals) were summed up to obtain a XRD pattern that represented the ensemble of the particle at a certain state of charge during galvanostatic cycling.

The position and the shape of representative reflections (003) and (104) were compared to investigate phase changes within the particle at targeted points of the reaction. The trends of these peaks were compared among the particles to evaluate if the electrochemical behavior of the particles was consistent with each other. Similar comparisons were performed to particles at C/20, from the previous study [11]. Inactive particles were found in both these earlier
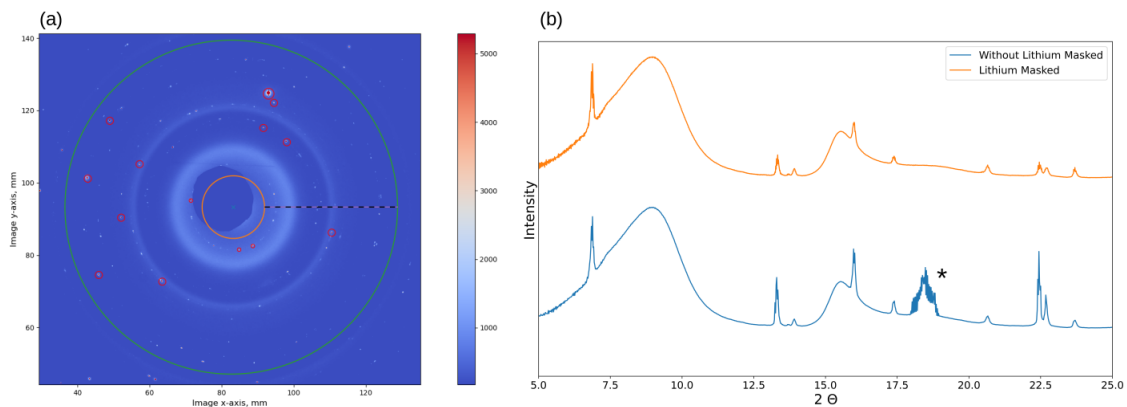
Figure 23. (a) An example of *operando* XRD 2D diffraction pattern ($\lambda = 0.5166$ Å) of P7 at single mapping position during third charge with C/3 and (b) Integrated 1D patterns with and without lithium signals being masked; the lithium signal was marked with *.

measurements, and those presented below. The existence of inactive particles was ascribed to experimental limitations associated with the modifications introduced in both electrochemical cell (AMPIX vs. conventional coin cells) and electrode design (dilute NCA tape) required to enable measurements resolving the behavior of individual particles.

4.3   Results and Discussion

4.3.1   Phase transformation of NCA secondary particle at C/8

The Ni K_α fluorescence image was used to ensure the particles selected were isolated from each other. An example is shown for P1 in Figure 22. The red color represents the center of the particle where the highest density of material is located. The green color represents a surrounding area with no Ni signal, as an indication that the particle was isolated and did not overlap any others. The image also provided an approximate measurement of the size of the

investigated particles. In the experiment at C/8, the size of the particle, from large to small, followed the order P1, P2 and P3, with approximately diameters of 10 μm, 6 μm and 5 μm, respectively. The summed XRD patterns for the particle, resulting from adding the patterns of each mapping position, at each state of charge, were stacked based on the time sequence of data collection as presented in Figure 24 with corresponding galvanostatic profiles.

All of the NCA peaks were indexed using a layered structure with R-$3m$ space group. The peaks that remained without indexing after this process, for example, around 2θ value of 17° in Figure 24 (a), resulted from spurious diffraction signals, among others, from metallic Li (PDF #00-001-1131) due to imperfect masking. These stacked patterns provided an overview of the NCA phase transformation of the particle by showing the change of the diffraction peak positions during cycling.

The overall evolution of each diffraction peak among P1-P3 indicated similar pathway of phase transformation within each particle in the first 1.5 galvanostatic cycles. For all three particles investigated, the overall trend of peak position at first charge was reminiscent of the observations reported by Robert, *et al.* [8]. Two diffraction peaks were selected for further inspection, (003) and (104), presented in Figure 25. Both of these two peaks had relatively strong diffraction signals and high expected sensitivity to small changes in cell parameter, as exemplified in Figure 20. In addition, these two peaks are well resolved from the other diffraction signals, which minimizes uncertainty when interpreting the change in position and shape.

We start our discussion on (003) diffraction peaks with P1 through P3, for which data was collected over first 1.5 cycles of the *operando* cell. All of these three particles remain in their
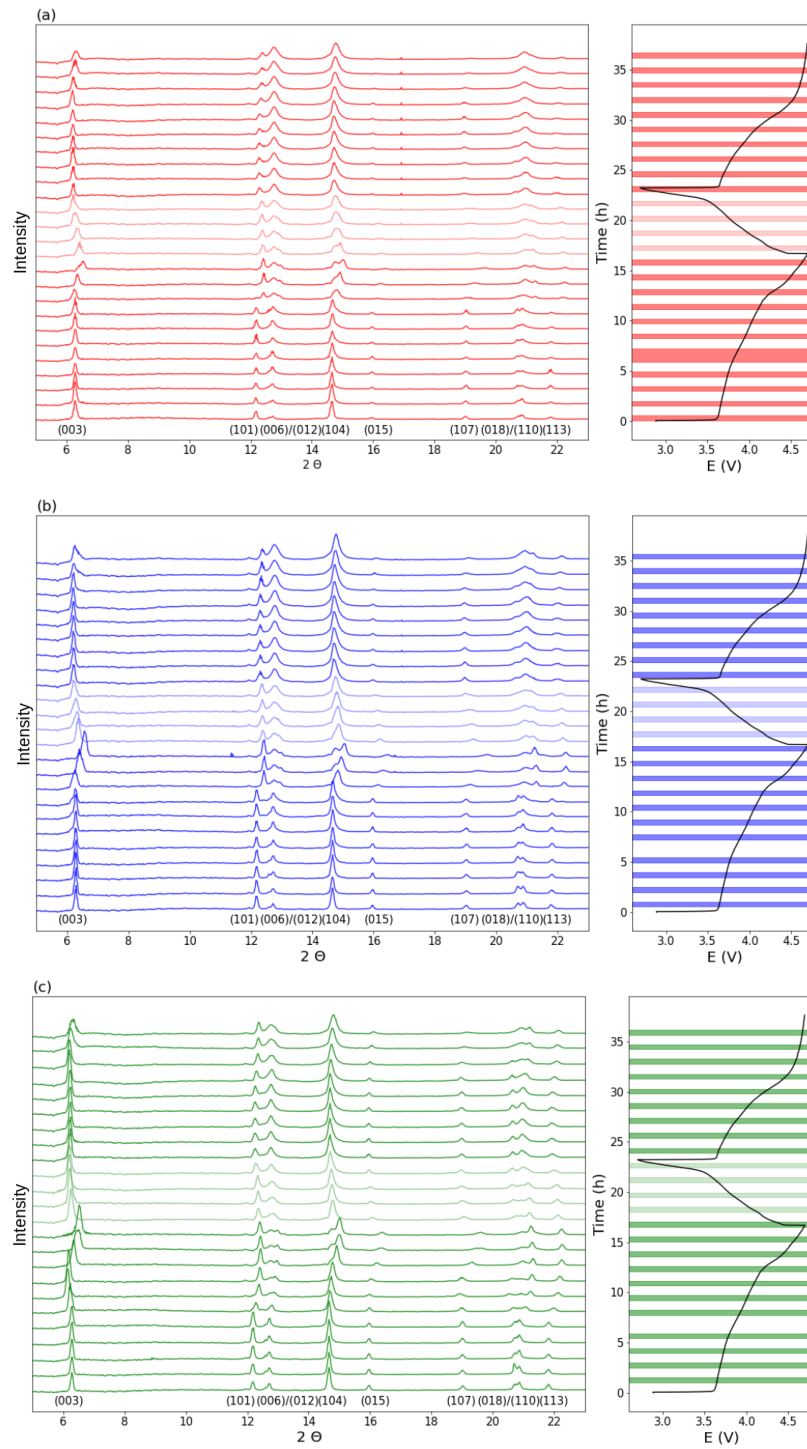
Figure 24. Evolution of the summed XRD diffraction patterns of (a) P1 (b) P2 and (c) P3, together with the associate electrochemical profiles of the cell. The patterns presented with lighter color in each panel represent the discharge sweep in that cycle.
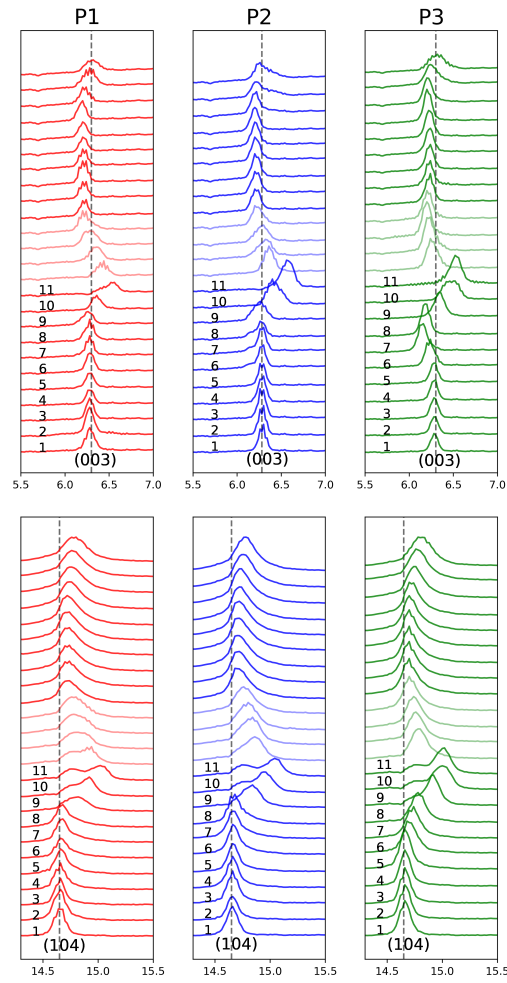
Figure 25. Summed diffraction peaks (003) and (104) of P1 (in red), P2 (in blue) and P3 (in green). The vertical dash lines indicate the position of the diffraction peaks in the pristine state, and are provided as a guide to the eye. The peak patterns of first charge were enumerated for convenience of discussion.

initial pristine phase at the beginning of the first charge with no clear change in both peak position and peak shape for first 7 summed XRD patterns of (003) for P1, and the first 5 for both P2 and P3. It was noted that the smaller particles tend to start their phase transformation earlier by showing (003) peak shifting towards lower 2θ. This could be an indication that lithium ions have shorter diffusion lengths in the smaller particles, and their higher surface-to-bulk ratio may favor activation of the reaction with current.

Starting from pattern 8 in P1, and pattern 6 in both P2 and P3, in Figure 25 all of these three particles entered a similar transition, consistent with Stage II described in Figure 20 for the NCA cathode, at which the (003) peak was characterized by shifting to lower 2θ as lithium ions were extracted. Slight differences were observed at this stage among P1-P3. For both P1 and P2, this shift was not as clearly captured as for P3, likely due to limitations of time resolution. Instead, the peak was captured already when it had already shifted to higher 2θ than the pristine state in P1 and P2, corresponding to high delithiation states, thus, Stage III. However, even before the shift was observed in both particles, the peaks also turned asymmetric, with clear shoulders to the left, for example, in pattern 9 in P1 or patterns 7 and 8 for P2 in Figure 25. The existence of a shoulder indicates the existence of at least one lattice with different c parameter compared to the dominant signal. It signifies chemical heterogeneity, which is not expected from a mechanism of delithiation following a solid solution, as exemplified in Figure 20.

In our study, with the experimental design of *operando* μXRD mapping, there are two possible reasons to explain the formation of an asymmetric peak. First, it could result from

the difference in kinetics within the particle so that its response to the applied current was not uniform across the particle, which led different domains to be at different chemical states when the pattern was collected. In this case, the summed pattern could be viewed as dominated by the spatial average. Second, with limited time resolution, it is also possible the complex summed XRD patterns resulted from the slightly different states the particle crossed during the scan of the 121 pixels in a given particle. In this situation, the last pattern collected would systematically be at a more advanced state than the first, with the sum primarily representing a time average. To evaluate the formation of an asymmetric peak, the XRD patterns of each mapping position with NCA signals were examined. In the first case, there should be no correlation in the changes of the individual XRD patterns with respect to when each location was mapped, while in the second case, the peak position of 2θ would follow a systematic evolution consistent with delithiation with the sequence of data collection. The pattern 9 in P1 in Figure 25 was used as an example to illustrate this evaluation. Figure 26 displays the position of diffraction signals, in 2θ, and their intensity, in the form of contrast of color, for each individual pattern collected. This peak intensity map showed no clear systematic and consistent distribution of 2θ peak position with the sequence of data acquisition. Therefore, the peak shoulder observed at pattern 9 in P1 was a result from heterogeneous chemical states coexisting within P1 during the process of delithiation.

Similar analysis was applied to evaluate peak shoulders in P2 as presented in Figure 27. Different from P1, in P2, patterns 6, 7 and 8 (Figure 25) had identical peak position with a left shoulder of varying relative intensity. As shown in the bottom panel in Figure 27, there
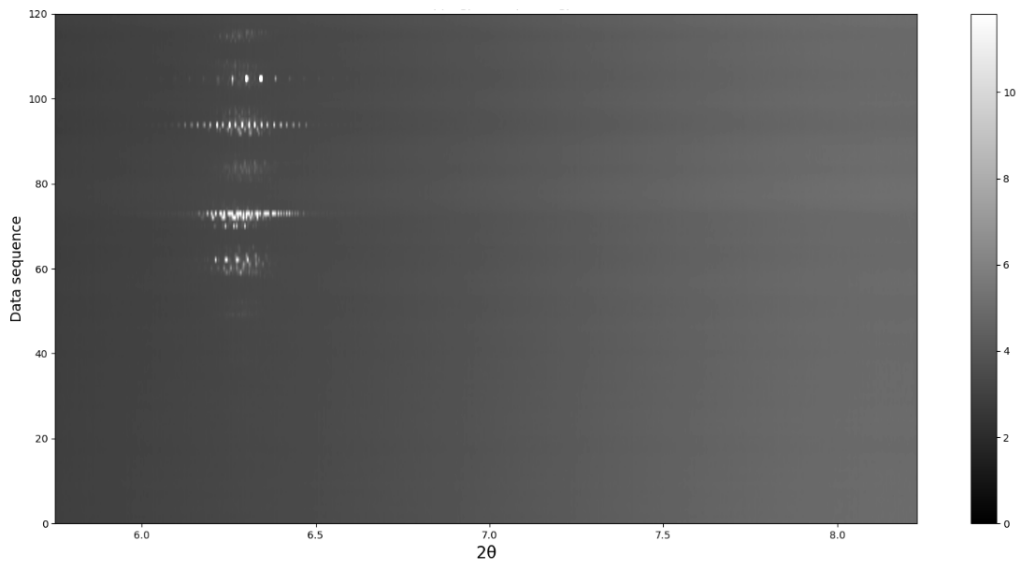
Figure 26. Map of the intensity of the (003) peak at each mapping position (data sequence) of pattern 9 in P1.

was no clear systematic distribution of peak intensity for pattern 6 in P2. There was a notable difference found for pattern 7 and 8, where the intensity maps of the (003) peak revealed diffraction clusters at two distinct 2θ positions, approximately at 6.1° and 6.3°, consistent with the position of the peak and its shoulder in the summed patterns. The signals at 6.1° appeared at similar mapping positions in consecutive particle maps and no systematic trend was observed along mapping positions as they were scanned, indicating that the shoulder found on the summed XRD was not the result of a time average. Instead, it matches a picture where the particle is reacting heterogeneously, with domains delithiating at different rates, and, thus, giving rise to multiple c parameters within the same particle at a given point in time. The

gradient between these domains was initially rather bimodal, as reflected by the existence of a dominant peak with a shoulder, but became very diffuse as more lithium ions were extracted, as signified by the notable broadening of the peak in pattern 9 of P2 in Figure 25, such that no shoulders could be observed.

Towards the end of the first charge (starting at pattern 10 for P1 and P2, and pattern 9 for P3 in Figure 25), the particles entered Stage III, where the (003) peak notably broadened and shifted to higher 2θ, following the expectations from high levels of delithiation. It is worth noting that the peak shapes remained complex for P1 and P2, with a visible shoulder to lower angles found in pattern 11 of P1. These complex lineshapes were taken as indication of persistent heterogeneity in the particles as the reaction proceeded. The peaks remained more symmetric in the first charge of P3 as presented in Figure 25 which indicated the phase transformation of P3 was comparably uniform during this first charge. However, it is worthy of notice that significant broadening was observed at pattern 10, which also displayed an unusual peak shape. This deviation was ascribed to the buildup of internal gradients of composition.

During the first discharge, all three particles underwent very similar evolution of the (003) peak in Figure 25. As lithium ions moved back to the cathode, the (003) peak tended to shift back to the initial position. It was noticed that the (003) peak did not move back exactly to the 2θ position of the pristine state at the end of discharge, but it was at higher 2θ. This effect was ascribed to the fact that, after going through Stage III, the particles got stuck in Stage II, not quite completing the path back to the pristine state.

Figure 27. Map of the intensity of the (003) peak at each mapping position (data sequence) of pattern 6 (bottom panel), pattern 7 (middle panel) and pattern 8 (top panel) in P2.

During the second charge, the changes were much less pronounced than in the first charge. There was only a minor shift to lower 2θ toward the end of the experiment, and only to approach values far from expected at full delithiation. This observation suggests that the particles were less active than in the 1st charge. P3 appeared to react the most, according to its greatest shift.

The co-existence of multiple compositions with different cell parameters in the NCA secondary particles during galvanostatic cycling at C/8 could also be verified through study on the (104) peak in Figure 25. While less intense than (003), its position at higher 2θ grants greater resolution of phases with smaller compositional gradients. Because of the influence of both a and c parameters, which change differently during the transformation as shown in Figure 11 [8], this peak only shifts to lower 2θ throughout the transformation through a solid solution.

Overall, the pathways of phase transformation evaluated from (104) were very similar through P1-P3. During the first charge, in Figure 25, (104) peaks of each particle stayed static through patterns 6 or 7, after which they rapidly moved to higher 2θ position as lithium ions were transported out from the layered structures. In addition, the (104) peaks of all particles showed a more or less pronounced peak splitting (see, for example, pattern 11 through P1-P3 in Figure 25). To again evaluate the origin of the peak splitting, intensity maps of the (104) reflection were carried out for pattern 11 in both P1 and P2 as shown in Figure 28. Two major centers of intensity were systematically seen around $2\theta = 14.9°$ and $15.0°$, with stray intensity around $14.7°$ in a small number of positions. Both intensity maps showed a random variation of the centers of gravity with the sequence of mapping, which was evidence of the existence of compositional gradients in the particle. The patterns were thus dominated by spatial effects,

rather than temporal. It is worth noting that P3 was confirmed to undergo heterogeneous changes when evaluating this peak versus a subtle lineshape effect in the (003) peak above, confirming the value of the greater resolution achieved at these angles.

During the first discharge, the (104) peaks of each particle shifted back to lower 2θ. However, while all of them reached a 2θ position that was close to the pristine state, they remained systematically higher. For P1 and P2 especially, the lineshapes also remained complex, with a semblance of a single peak only reached at the end of the process. Therefore, it can be concluded that discharge proceeded heterogeneously as well, albeit in a more progressive fashion than charge. During the second charge, as with the (003) reflection, only a slight move towards the right was observed in (104), as an indication of a significantly lower degree of lithium extraction than in the first charge. Overall, the observations of (104) peaks of P1 to P3 were aligned with the assessment from the (003) peak. While the first charge efficiently achieved high levels of delithiation, this efficiency decreased with cycling, particularly over the second charge, where all three particles progressively got stuck at Stage II.

At this point, it should be noted that, in our study, the time onset of the phase transformation of NCA during the first charge, evaluated from diffraction peaks, varied among the particles with different size (P1 vs P2 and P3). However, it is not clear whether the difference in size also affected the different kinetics within the secondary particle once the reaction initiated because its inherent rate was fast enough for the measurement performed in this thesis to suffer from insufficient time resolution, where the acquisition did not sample each particle enough to perform a quantitative analysis of rates. The fact that these three particles had
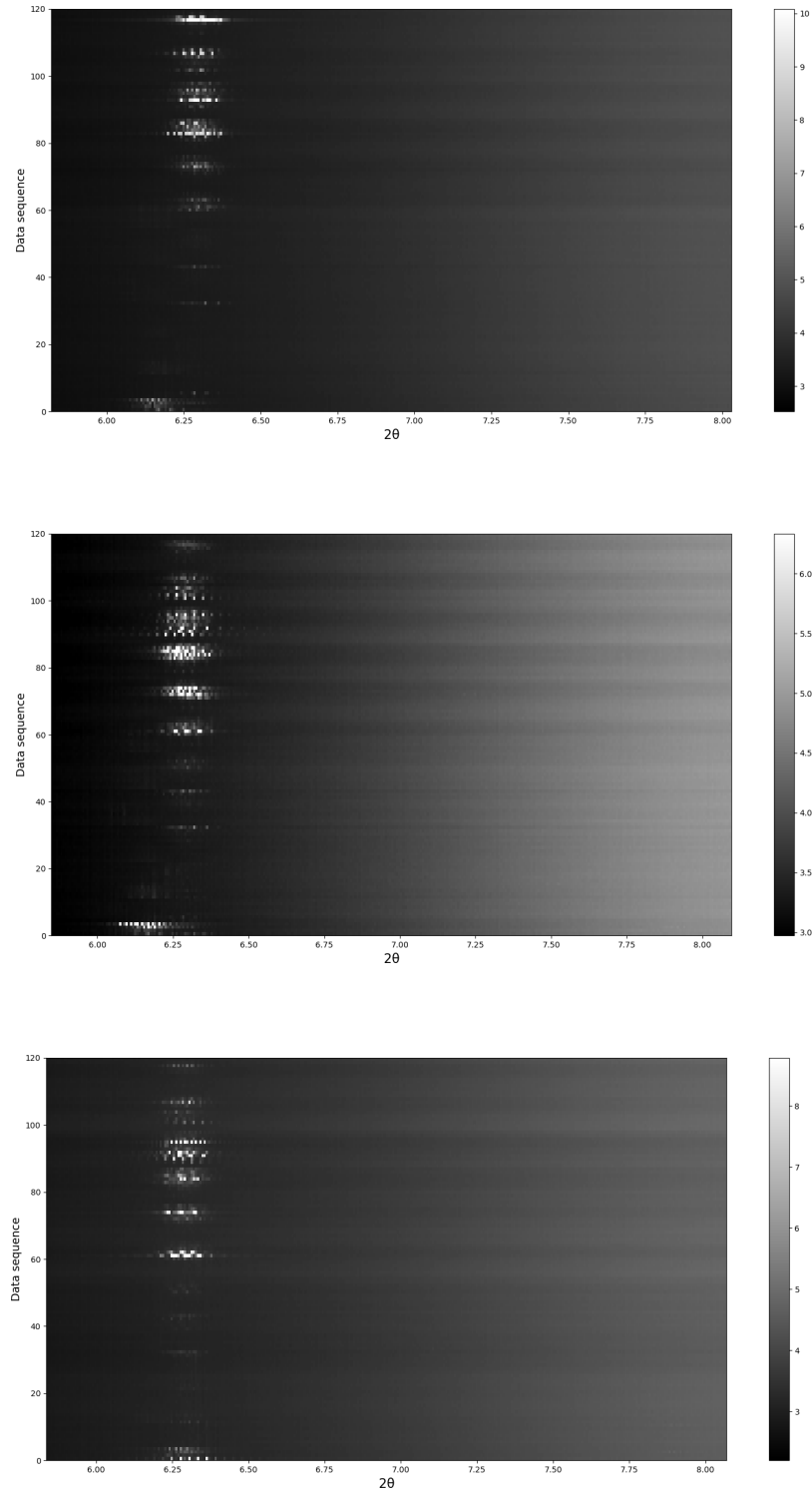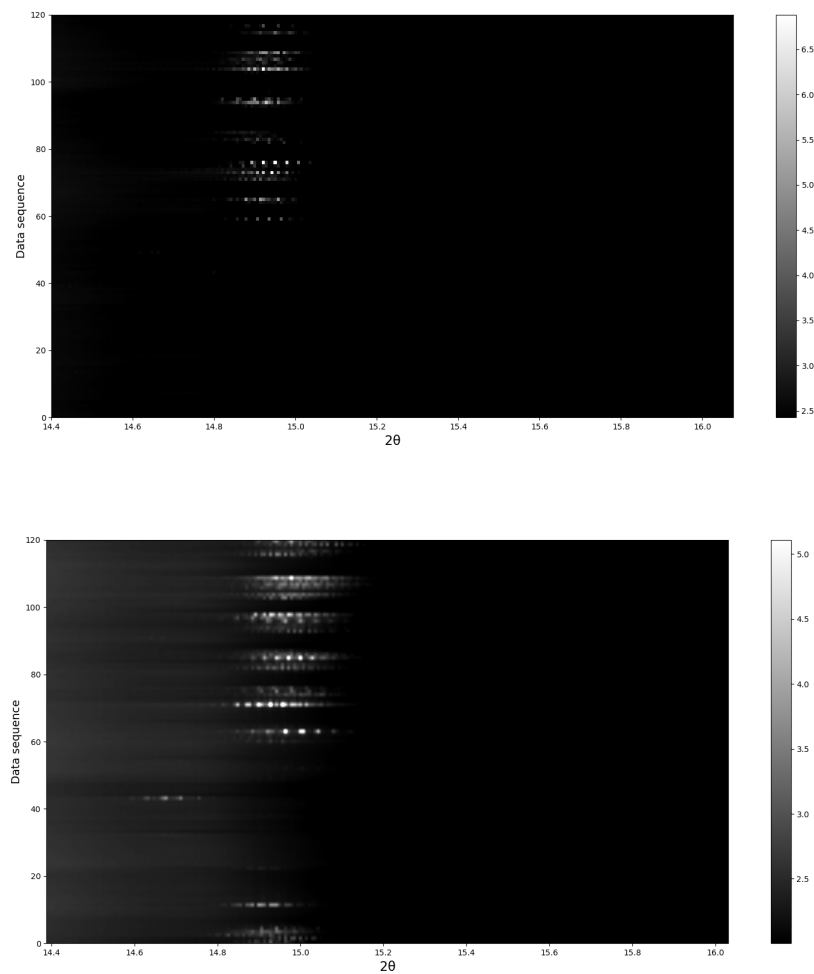
Figure 28. Maps of the intensity of the (003) peak at each mapping position (data sequence) of pattern 11 in P1 (top panel) and pattern 11 in P2 (bottom panel).

similar electrochemical behavior after the first charge could be an indication that the size of the particle did not dramatically contribute to the behavior and heterogeneous states within the NCA particles during galvanostatic cycling.

As differences were found in the evolution of NCA peaks between the first charge and subsequent cycles, two other particles, P4 and P5, from Cell II cycled at C/8, were studied over the second discharge, third charge and third discharge. Both P4 and P5 had an approximate diameter of 5 μm, estimated from their Ni K$_\alpha$ absorption images. However, it must be noted that the diffraction signals were weaker than in the case of P1 to P3 above, making analysis more challenging. The *operando* μXRD mapping for Cell II started at the end of second charge, part of which was also captured as presented in Figure 29. The initial positions of the peaks were consistent with NCA being partially delithiated. The (003) peaks of both particles, P4 and P5, moved towards the higher 2θ angles with no significant change in the peak shape and no peak splitting at the end of second charge. It is interesting to note that the position of the peaks at the end of charge matched well with the highest delithiation states observed in the first charge of P1-P3, indicating that greater activity was captured in the second cycle in this experiment. The peaks shifted back to lower 2θ angles during the second discharge. However, peak splitting was found for P4, indicating multiple compositions with different lattice parameter c appeared within the particle at the same time, and these domains progressed at different rates. As more lithium ions were intercalated back, the compositional gradient in the particle faded, and the complex lineshape collapsed into one peak towards the end of second discharge. It is worth noting that the pattern stopped changing when discharge was still ongoing, suggesting that the
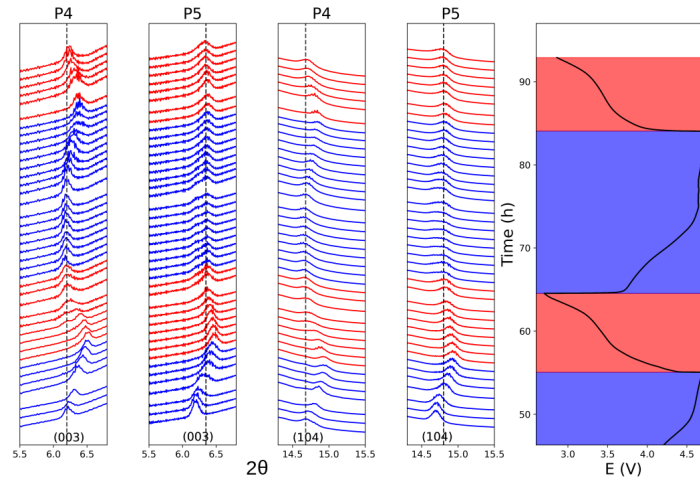
Figure 29. Summed diffraction peaks of (003) and (104) for P4 and P5 with galvanostatic profile with C/8 from the partial second charge to the end of third discharge . The diffraction patterns during charging are plotted in blue and patterns during discharge are in red. The dash line indicates the 2θ value of the corresponding reflection at the start of the the third charge to provide a reference regarding changes in peak position

particle reached its endpoint before the electrode as a whole. For P5, the (003) peak stopped changing partway through the second discharge, which was an indication it became inactive. Unlike P5, P4 continued reacting through the third cycle based on the evolution of (003) peaks, but the swing in cell parameters progressively became smaller. The evolution of peak (104) of both P4 and P5 were generally consistent with the transformation of (003) peak. However, the poor signal-to-noise ratio precluded further analysis.

Comparison of the evolution of (003) and (104) diffraction peaks through P1 to P5 revealed some characteristics of NCA secondary particles at galvanostatic cycling with C/8. First, the overall pathway of phase transformation for actively reacted particles was similar at different

cycles, with heterogeneity building up within the particles at different points of the reaction, as denoted by the onset of peak splitting. Second, it is worth noting that the reactions reached similar end points across particles. For instance, the peak position of P4 at the end of the second discharge (Figure 29) was comparable to the end of the first discharge for P1 to P3 (Figure 25). Lastly, the NCA particles degraded with cycling, as P1, P2 and P3 turned less reactive during the second charge compared to the firste, P4 turned less reactive at the third charge compared to the second and P5 was completely inactive after second discharge. Since these are highly reversible materials that can be cycled hundreds to thousands of times, we posit that this degradation is connected to the illumination of the cell with ionizing radiation, even if the X-rays were at high energy. Previous experience in our group is that beam damage is associated with loss in activity, likely through the decomposition of the organic electrolyte used to close the electrochemical circuit. Further research is needed to overcome this experimental challenge.

4.3.2 Effect of cycling rate on the pathways of phase transformation

All in all, compared to the smooth relationship between x in $Li_{1-x}Ni_{0.80}Co_{0.15}Al_{0.05}O_2$ and the change in diffraction peaks in the first charge expected for a solid solution mechanism that is homogeneous within the whole material [8,69], heterogeneous reactions were often found in the pathways of individual secondary NCA particles based on the analysis of the peak shapes. In all cases, the reaction started when the cell had been charging at C/8 for a few hours. Comparison with the literature [8,69] indicates that delithiation was largely complete at the end of the first charge. Given that each pattern corresponds to 24 min, the fact that most of the reaction was

captured in patterns 7 to 11 indicates it completed in 2 h. This observation indicates that the reaction at the single particle level was significantly faster than the electrode as a whole. Intriguingly, the rates at which particles were found to react was similar in both cases, further suggesting that it approaches the inherent rate of the reaction.

The evolution of two NCA particles during the first galvanostatic cycle at slower rate (C/20) was studied by Dr. May [11]. The overall trends are similar to what we observed in P1 to P3. However, his study demonstrated that, at slower rate, C/20, the phase transformation of the NCA particles was more uniform, with single symmetric peaks in the summed patterns, as shown in Figure 30, which were found to be consistent with a homogeneous mechanism of solid solution. Since peak splitting and asymmetry appeared in our study at C/8, it is tempting to conclude that the increased C rates promoted a less uniform phase transformation within the NCA particles due to limitations of intraparticle diffusion [70]. However, it must be noted that acceleration of the rate of delithiation of the particle with respect to the overall rate of the electrode was observed at both C/20 [11] and here at C/8. Furthermore, the timeframes at which particles were found to completely delithiate were around 1-2 h in both cases. This observation suggests that the applied current modulates kinetic behavior of individual particles by creating differences in sequence of transformation between domains, but it does not change their inherent mechanism once the reaction starts.

4.3.3   NCA secondary particles at C/3

Since comparison of data collected at C/20 [11] and C/8 showed significant difference in the reaction heterogeneity, but not the inherent timescale at which the overall particle transformed,
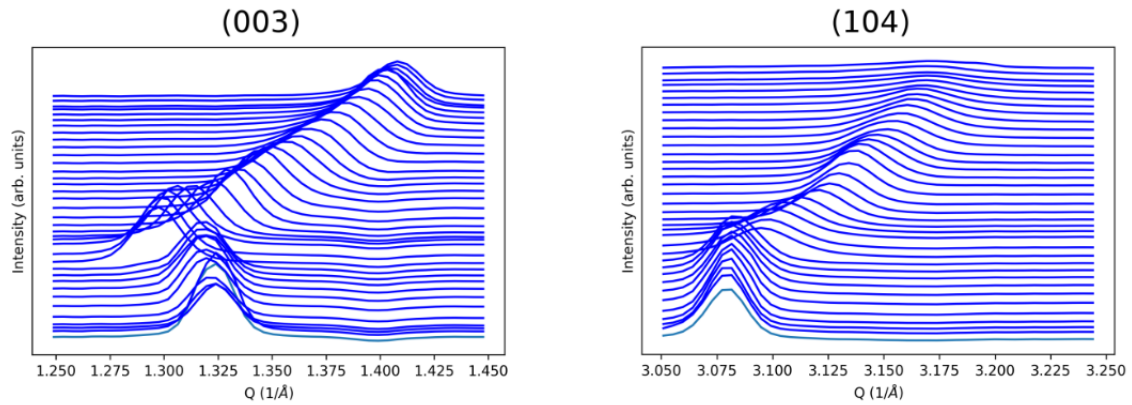
Figure 30. Summed diffraction peaks (003) and (104) of NCA secondary particle during the first charge cycled at C/20. Reprinted from [11] with permission

we performed *operando* XRD measurement at a even faster discharge rate, C/3. Our first goal was to investigate any effects on the pathway of phase transformation with this increased discharge rate, particularly applying cell currents approaching the inherent nanoscale rate of individual particles at C/8 or C/20. Two particles, P6 and P7, were measured at this rate but at different galvanostatic cycles. The XRD patterns collected at this discharge rate were collected continuously since only a single particle was mapped for Cell III and Cell IV, P6 and P7, respectively.

The stacked summed XRD patterns P6 were presented in Figure 31. Overall, the (003) and (104) peaks of P6 did not follow clear shifts characteristic of either Stage II or Stage III during the first charge. Instead, a shoulder appeared to the right of both reflections toward the end of charge. In the case of the (104) reflection, the shoulder shifted far enough to be resolved from

the dominant peak. The shoulders shifted back and merged into the main reflection during first discharge. Interestingly greater activity was observed in the second charge, where there was a clear shift to lower angles of both (003) and (104) in the last 3 patterns collected. The (104) developed clear tails to lower angles in this process. Based on the rules of analysis already employed above, the appearance of shoulders during the first charge was taken as an indication that only a very small part of P6 tends to react and the majority remained in the pristine state. The portion was reversible on discharge. Subsequent charging witness a general activation of the particle, which delithiated quickly, but again heterogeneously, with a small portion lagging in progress.

The stacked summed XRD patterns of P7 are shown in Figure 32. Both (003) and (104) peaks were only actively shifted during first charge, showing a characteristic of Stage II. Both of these two peaks remained static after that stage, through the end of the charge of the cell and beyond, meaning that P7 turned inactive after some delithiation.

The *operando* measurement on P6 and P7 indicated that the measurements became challenged when a rate as fast as C/3 was imposed. With this fast rate, the NCA particles tended to reacted partially, at best, if they did not become inactive after slightly delithiating, as P7. When meaningful changes in the patterns were observed, as at the end of the second discharge of the cell containing P6, it was clear that the particles are able to sustain high rates, with significant delithiation in less than 1 h (2 patterns), as expected from the measurements at C/8 and C/20. Instead, the challenges seem to be rooted in the design of the AMPIX cell and the
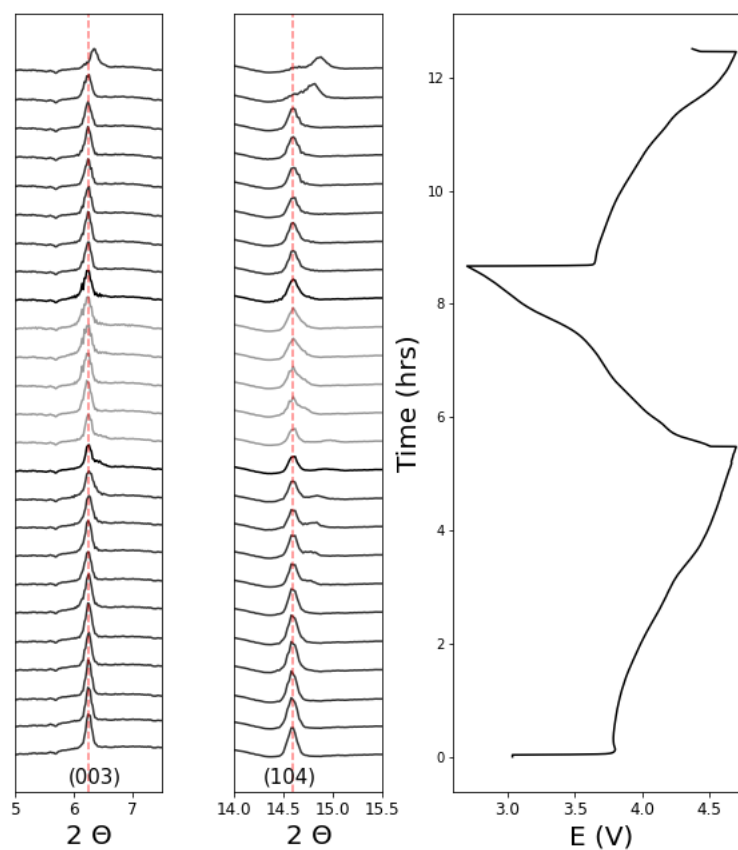
Figure 31. Summed diffraction signals of the (003) and (104) reflections for P6 compared to the electrochemical profile of the cell containing a dilute NCA cathode, cycled at C/3 from first charge to the end of second charge . The diffraction patterns during charging were plotted in black and patterns during discharging in grey. The dash line labeled the 2θ value of the pristine peak to provide a guide to the eye of changes in peak position.

Figure 32. Summed diffraction signals of the (003) and (104) reflections for P7 compared to the electrochemical profile of the cell containing a dilute NCA cathode, cycled at C/3 from second charge to the end of fifth discharge shaded in blue. The diffraction patterns during charging were plotted in black and patterns during discharging in grey. The dash line labeled the 2θ value of the pristine to provide a guide to the eye of changes in peak position.
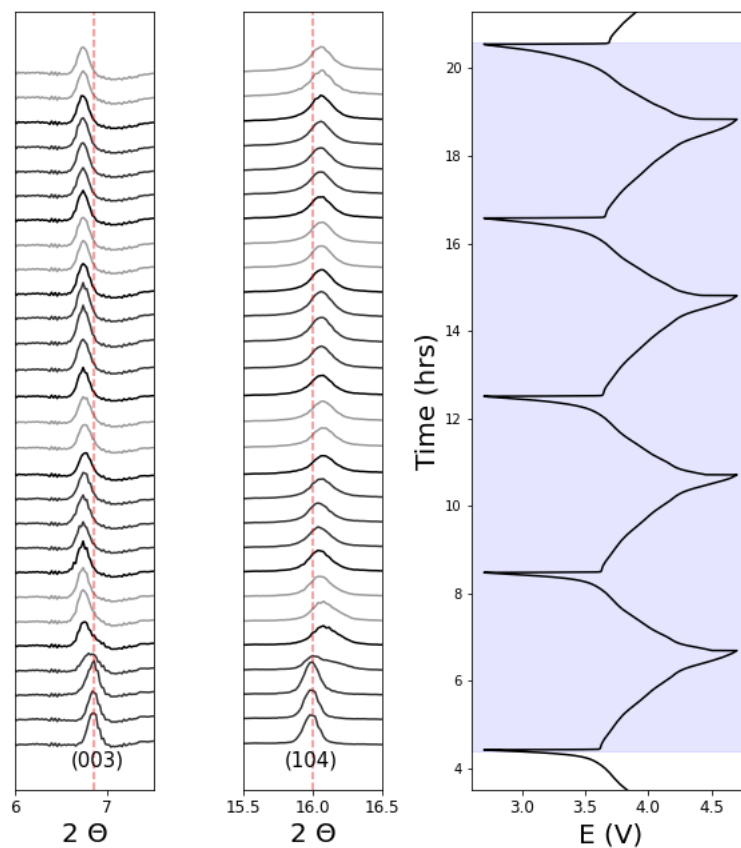
diluted electrodes. Follow-up work should be aimed at improving the electrochemical response of the cell so that these measurements can be conducted in the future.

4.4 Conclusion

Using a small beam at a synchrotron facility successfully allowed us to extend our mapping techniques to the study of individual secondary particles of NCA. The analysis of summed XRD patterns revealed compositional gradients formed within the NCA secondary particles at C/8, meaning that there was a nonuniform response to the applied current across the particle. Our work also revealed that compositional gradients also persisted with cycling (up to the third cycle in our study). Our study was limited to observe the peak evolution of NCA particles at fast rate (C/3) because of their increased inactivity in these conditions. This challenge calls for a better design of the AMPIX cell and the diluted electrode to improve local electrical connections within the particles.

In order to identify what could be the possible reason led to the formation of this heterogeneity of kinetic within the NCA particles, we compared the evolution of each individual particle as a whole at different discharge rates. There was no clear difference in the pathways of peak evolution of NCA particles at C/20 and C/8. In both cases, the effective rates of charge of the particle were much faster than the overall rate applied to the cell. However, the NCA particles had different intraparticle behavior at slower rate (C/20), which favors a response to the applied current that was completely uniform across the particles, with heterogeneity building up as the rate increased. We conclude that the particles followed the similar inherent mechanism but the kinetic behavior of discrete domains within individual particles was affected

by different C rates. The observed compositional gradient as the rate increased was ascribed to a heterogeneity of kinetics of lithium diffusion within the particle, adding a new layer of understanding of the interplay of different parameters with respect to previous work.

In summary, we extended a novel μXRD *operando* mapping technique to examine the local kinetics of NCA at the level of individual secondary particles. Based on our study, we propose that the heterogeneity of the kinetic within the NCA particles was correlated to the C rates, suggesting an intricate interplay between the kinetics of charge transfer, indicated by the exchange current, and the diffusion of carriers within the material.

CHAPTER 5

ELECTRODEPOSITION GRADIENT INDUCED BY CHANGE IN DEVIATORIC STRAIN AND MICROSTRUCTURE OF $Li_7La_3Zr_2O_{12}$ SOLID ELECTROLYTE

The content of this chapter is based off a manuscript in preparation: Garcia-Mendez,G.,Li,C., Wang, M.J., Xu,R., Sakamoto, J. and Cabana,J.:Stable Li Electrodeposition Gradient Induced by Change in Microstructure, Mechanical and Transport Properties of $Li_7La_3Zr_2O_{12}$ Solid Electrolyte

5.1 Introduction

Compared to traditional Li-ion batteries (LIBs), all-solid-state lithium batteries (ASSLBs) with the corresponding metal anode provide enhancements in safety, energy density and, in certain conditions, potentially even high-power density [71]. As one of the promising candidates for the electrolyte in ASSLBs, $Li_7La_3Zr_2O_{12}$(LLZO) has drawn research attention due to its high ionic conductivity, high stability against lithium metal and good overall electrochemical performance. However, in order to make full use of LLZO and advance ASSLBs toward deployment, some challenges need to be overcome such as the need to fabricate thin membranes to sustain currents comparable to liquid electrolytes, issues of interfacial contact at both electrodes, instability when stored in air [72] and particularly, as in this chapter, alleviate degradation of electrochemical performance during cycling.
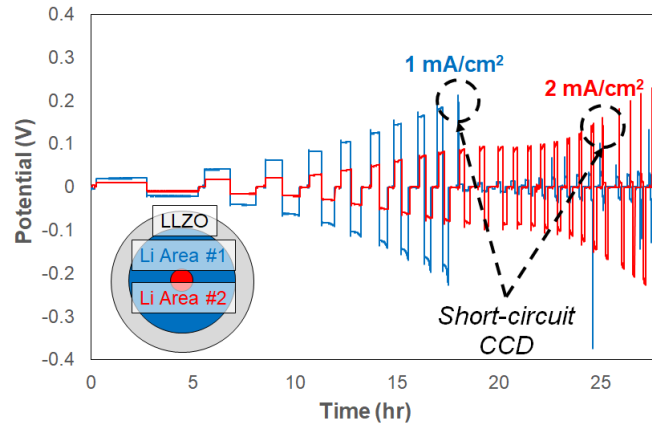
Figure 33. Evolution of the potential upon application of cycles of constant current, as indicated in the plot, of opposing sign in a $Li|Li_{6.5}La_3(Ta_{0.55}Zr_{1.45})O_{12}|Li$ symmetric cell. The cell was constructed to measure the behavior at the center of the LLZO membrane separate from the exterior, as indicated by the schematic inset, thus providing a measure of the critical current density gradients along the radius of Ta-LLZO.

Previous work from the research group of Prof. Jeff Sakamoto at University of Michigan suggested that there is a gradient in electrochemical performance as a function of radial position of circular LLZO membranes fabricated as shown for Ta-LLZO in Figure 33. The critical current density (CCD) is defined as the amount of current at which failure through a short-circuit is observed in symmetric Li/electrolyte/Li cells. This short circuit is induced by the penetration of dendrites into the electrolyte. A novel CCD test developed by the Sakamoto group examined two major domains, the center area (in red) with a radius of 3.175 mm and the entire sample (in blue) with a radius of ~6.35 mm. It was found that when the domain covered by the Li electrodes encompassed the entire disk, the cell tended to short-circuit more easily. The decrease in CCD when larger Li electrodes were used suggested that lateral conductivity gradients existed

in the Ta-LLZO sample. The same CCD test was performed on Al-LLZO sample with similar observation. Although not shown, the short-circuit CCD was 0.7 mA/cm^2 when center area with radius of 3.175 mm and 0.3 mA/cm^2 for the domains covered entire sample.

In order to investigate the possible factors leading to the observed electrochemical performance degradation, we developed a methodology of X-ray diffraction mapping to study both local physical and chemical properties of $Li_7La_3Zr_2O_{12}$. A plausible hypothesis, put forth by the Sakamoto group, is that the gradient in electrochemical performance along the radial position is the result of the processing conditions of the solid electrolyte: hot-pressing green bodies in a cylindrical die. Although hot-pressing allows for fabrication of high density ceramics, due to the presence of a uniaxial compressive stress and constraints in the lateral direction, hot-pressing can also result in differential sintering in the radial axis, which could affect CCD even after careful control of the surface topology by polishing and/or interface engineering. This control discarded the possibility that heterogeneity of the microstructure at the surface of LLZO induces the variations in electrochemical cycling properties, a hypothesis put forth by Cheng *et al.* [73]. Deviatoric strain can be used to describe such differential sintering. The work presented in this chapter will demonstrate a mapping methodology with high-resolution synchrotron Laue X-ray diffraction to visualize the distribution of deviatoric strain in LLZO membranes. This map will provide a better insight of the relationship between deviatoric strain and the radial gradient of electrochemical performance. Complementary Bragg μX-ray diffraction measurements at a lower spatial resolution also provide a means to evaluate possible gradients in chemical

composition by following the relative intensity of different reflections across the surface of the $Li_7La_3Zr_2O_{12}$ membrane.

5.2 Experimental Methods

5.2.1 Mapping of strain with Laue X-ray Diffraction

The Laue X-ray diffraction patterns were collected at beamline 34 ID-E at the Advanced Photon Source (APS), Argonne National Laboratory (ANL). The samples were transferred to a glove box at sector 11 at the APS. Each sample was placed in between two pieces of micro-cover glasses (0.13-0.16 mm thickness). The gap between glasses was filled with gasket and epoxy to avoid air exposure. The ensemble was placed on an $45°$ inclined stand as shown in Figure 8. A focused polychromatic beam with broad-bandpass radiation (white beam) was used to hit on the surface of the sample with 20-30 μm penetration.The diffraction was collected by a Perkin-Elmer XRD 1621 flat-panel detector. All of the samples were mapped with an quadrant area with step size of 50 μm except Sample 2 (Al-LLZO post-annealed), which was measured with a strip area along the radius direction considering the shape of the largest piece of the specimen used for the experiment.

5.2.2 Deviatoric Strain Analysis

The axis system was aligned with the sample for analysis, with the x and y axis set as the horizontal plane of the membrane while z was the vertical axis normal to its surface, i.e., along its thickness. The collected reflections in the Laue μX-ray diffraction patterns (an example shown in Figure 34 (a)) were automatically indexed with a cubic crystal system (Ia-$3d$ a_x:a_y:a_z=1:1:1,
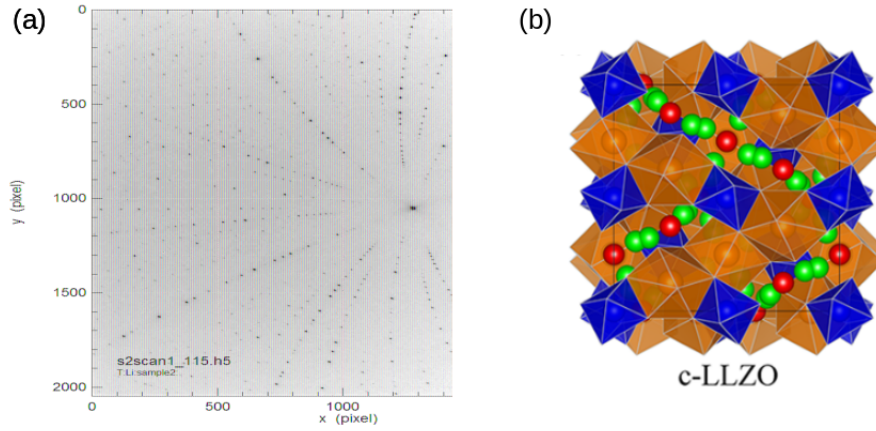
Figure 34. (a) An example of Laue reflections of Post-annealed $Li_7La_3Zr_2O_{12}$ and (b) Crystal structure of cubic LLZO. (b) was adapted from [12] with permission. Copyright © 2018 American Chemical Society

as shown in Figure 34(b) [12]), corresponding to the reported structure of LLZO [24], by IGOR Pro with the package of LaueGo developed by APS.

After the peaks were indexed, deviatoric strain analyses were carried out based on the measured peak positions to extract the actual ratio among a_x, a_y and a_z. Given the hypothesis that the lattice strain in our samples would have spatial dependence along the radius, this project only focused on the study of the trend in deviatoric strains along the *x, y, z* directions of the $Li_7La_3Zr_2O_{12}$ samples, ε_{xx}, ε_{yy}, ε_{zz} in the ε matrix:

$$\varepsilon = \begin{Bmatrix} \varepsilon_{xx} & \varepsilon_{xy} & \varepsilon_{xz} \\ \varepsilon_{yx} & \varepsilon_{yy} & \varepsilon_{yz} \\ \varepsilon_{zx} & \varepsilon_{zy} & \varepsilon_{zz} \end{Bmatrix}$$

All of these three components provided information about any alteration of the shape of the unit cell from cubic to tetragonal within the measured volume. In deviatoric strain measurements the unit cell volume is assumed to be constant as X-ray Laue diffraction is not sensitive to isotropic lattice compression or expansions, which means an additional relationship between the three principal strain components: $\varepsilon_{xx} + \varepsilon_{yy} + \varepsilon_{zz} = 0$. Considering the sample's cylindrical symmetry, we picked ε_{zz} to represent the lattice distortion at each location in the following discussions.

5.2.3 Bragg X-ray Diffraction

The X-ray diffraction patterns of $Li_7La_3Zr_2O_{12}$ samples were collected both for the ensemble and at different resolved spots on the membranes using two different Bruker D8 diffractometers at UIC. They are both equipped with a monochromatic beam (Cu-K_α radiation, $\lambda = 1.5418$ Å) A D8 Advance was used for PXRD, which probes the bulk of the sample. In turn, a D8 Discovery equipped with a 0.8mm collimator was used for μXRD. The beam hit the surface of the sample at the 2θ angular range of 45 to 75°. Four patterns were collected in different spots of each sample, with step size of 1.79 mm between mapping positions and 300s exposure time.

5.3 Results

As X-ray diffraction is sensitive to structural differences, the received samples from Dr. Sakamoto's group (Al-LLZO pre-annealed, Al-LLZO post-annealed, Al-LLZO hot-pressed and Ta-LLZO hot-pressed as listed in Table III) were examined by PXRD at UIC (Figure 35).

The PXRD patterns indicated some compositional difference among the samples, with impurities (e.g., the peak to the right of the (220) reflection at approximately $2\theta = 21°$) observed in
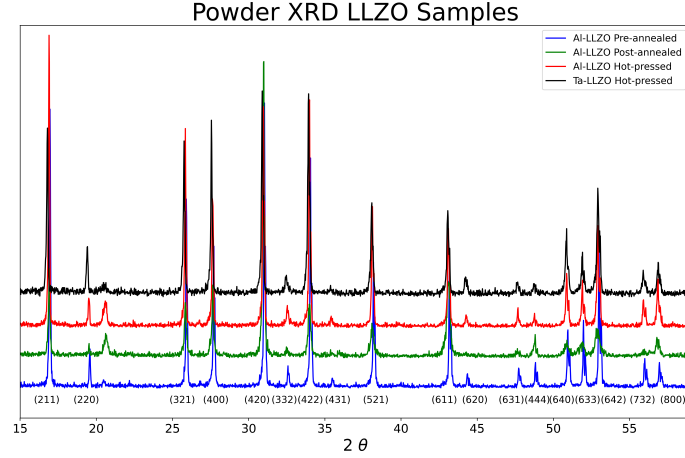
Figure 35. Power X-ray Diffraction Patterns of $Li_7La_3Zr_2O_{12}$ Samples

Al-LLZO post-annealed, Al-LLZO hot-pressed and Ta-LLZO hot-pressed. The more important observation is the change of relative peak intensity among samples. The clearest change can be observed among the peaks of (640), (633) and (642). More subtle differences were observed in the shape of specific peaks, where tails toward lower angles were found to arise after annealing. We propose that this observation can result from the existence of local heterogeneity within the LLZO membranes, either compositional or microstructural (or both). In this chapter, we demonstrate experiments with μX-ray diffraction to investigate if such local heterogeneity exists, evaluate trends of any changes and discuss what could be done to correlate the changes with the electrochemical performance of the LLZO.

Maps of the deviatoric strain of Al-LLZO Pre-annealed, Al-LLZO Hot-pressed and Ta-LLZO Hot-pressed samples in the zz direction over a quadrant area are shown in Figure 36. Due to
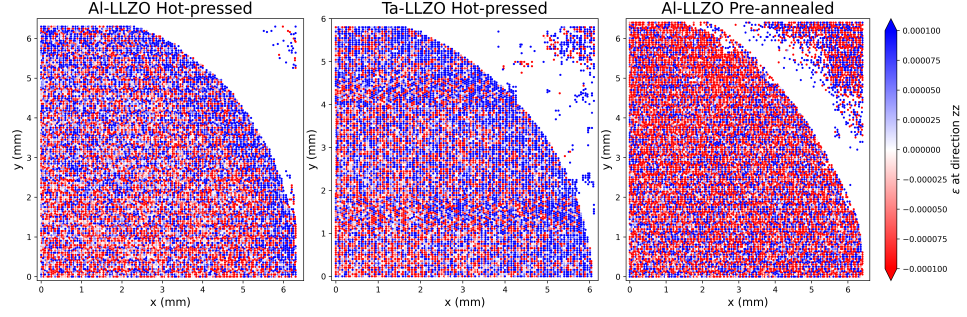
Figure 36. Deviatoric Strain ε_{zz} Maps of Li$_7$La$_3$Zr$_2$O$_{12}$ Samples

the damage on Al-LLZO Post-annealed, there were not enough data points collected to show the deviatoric strain gradient. The positive ε_{zz} was displayed in proportionally darker shades of blue, standing for tensile deviatoric strain, while negative ε_{zz} was displayed in red, representing compressive deviatoric strain. The data points outside the sample area could be stray strain signals from either the gasket or epoxy residuals in the sample holder. White spots were used to indicate ε_{zz}=0, where there is either no alteration between the measured unit cell and indexed shape in that direction, or the measured unit cell is isotropically enlarged or compressed. These situations are indistinguishable in this measurement.

Qualitatively, the measured area of Al-LLZO Pre-annealed contained a preferential distribution of pixels subject to compressive strain in the zz direction. The strain map of Al-LLZO Pre-annealed did not show any obvious evidence of a gradient in deviatoric strain over the measured area. In order to quantitatively assess any spatial dependence of ε_{zz} on the surface of Al-LLZO Pre-annealed, the measured quadrant area was iso-segmented into 10 sections based
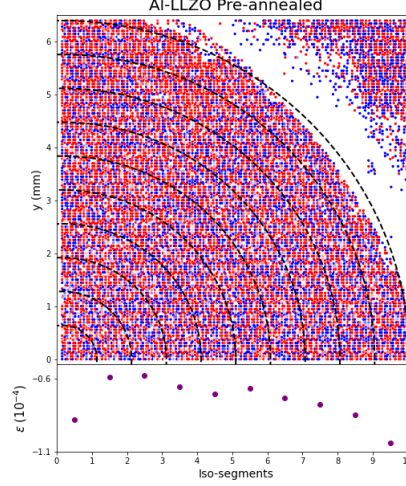
Figure 37. Map of the Deviatoric Strain ε_{zz} of Al-LLZO Pre-annealed. The bottom displays the average value of ε_{zz} extracted from iso-segmentation of the object into 10 portions based on distance from the center, as indicated in the map.

on the distance from the disk center, as presented in Figure 37 with dotted arc lines. Though the sample size of each section was different because of the shape of the object, each section included sufficient number of observations to confidently represent the overall deviatoric strain distribution. The average deviatoric strain ε_{zz} of each section was plotted at the bottom of Figure 37. A subtle, decreasing trend in ε_{zz} was found along the radial direction, especially toward the extremes. For instance, the average of ε_{zz} in section 10 was -1.04×10^{-4} compared to -0.84×10^{-5} in section 2. However, the sign of ε_{zz} remained consistent with an overall predominance of the compressive states at each segment. This trend suggested Al-LLZO Pre-annealed was slightly more compressed along the zz direction at the edge of the membrane.
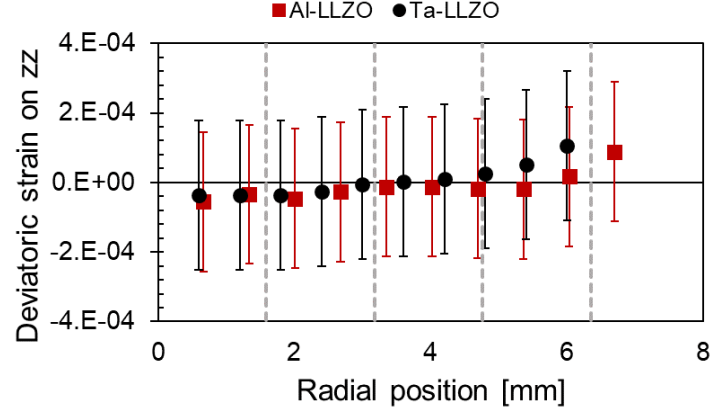
Figure 38. Values of Deviatoric Strain ε_{zz} with Radial Position. Error bars represent the standard deviation of the average in the iso-segment, and, thus, express only the dispersion of values in the population. The changes were found to be significant with respect to the limit of detection of the technique.

Compared to Al-LLZO Pre-annealed, the measured area of both Al-LLZO Hot-pressed and Ta-LLZO Hot-pressed showed greater evidence of tensile stress, as indicated by a greater overall prevalence of more blue color in the maps (Figure 36). It indicates that hot-pressing relieved compression along the zz direction. A gradient in both the magnitude and sign of the average deviatoric was also apparent along the radius of both membranes. The center of the sample had visibly greater incidence of red pixels subject to compressive strain while the areas towards the edge of the sample were dominated by tensile strain. This color gradient visually represents the existence of a gradient in deviatoric strain along the radius, from compression being, on average, dominant in the center, to tension taking over at the edge.

In order to quantitatively describe the deviatoric strain gradient, the measured quadrant area was iso-segmented into 10 sections based on the radius, as with Al-LLZO Pre-annealed above. The average of deviatoric strain ε_{zz} of each section of both Al-LLZO Hot pressed and Ta-LLZO Hot-pressed was plotted in Figure 38, with error bars providing solely a measure of the standard deviation and, thus, they reflect the dispersion of values in the iso-segment, not the accuracy of the measurement, which is greater than the difference between the most extreme values observed. For both samples, the deviatoric strain on zz direction increased as the radial position increased. From the center to the edge, ε_{zz} from -0.37×10^{-4} to 1.06×10^{-4} for Al-LLZO Hot pressed and -0.56×10^{-4} to 0.88×10^{-4} for Ta-LLZO Hot-pressed. All in all, the process of hot pressing not only introduced tensile strain into the membranes, but it does so more selectively at the edges of the membrane. Therefore, the measurement of deviatoric strain, ε, using Laue X-ray diffraction has established a correlation between the gradients of CCD observed by our collaborators and associated gradients in strain, from compressive to tensile, within the electrolyte membranes.

Based on the effects observed by PXRD, μXRD measurements were performed at different radial position of the sample, to evaluate their local persistence. The 2D XRD images of Ta-LLZO Hot-pressed sample are presented in Figure 39. The first scan at the center of the sample was labeled R1, and subsequent scans were collected with a step size of the scan of 1.79 mm along the radius, to obtain scans R2, R3 and R4. Normalized X-ray Diffraction patterns of $Li_7La_3Zr_2O_{12}$ samples at 2θ range of $49°$ to $58°$ are presented in Figure 40. The angular range includes the (640), (633), (642), (732) and (800) reflections.
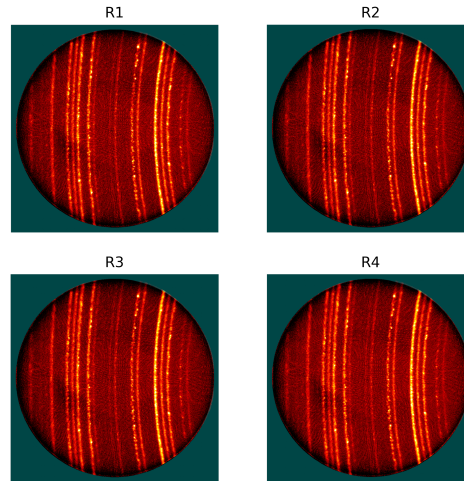
Figure 39. 2D XRD images of Ta-LLZO Hot-pressed $Li_7La_3Zr_2O_{12}$ Sample at Different Radial Positions(R1-R4)

While the position of the reflections did not visibly change between radial positions in the same sample, there were clear differences in their relative intensities. These differences are best evaluated from the ratio of relative intensities between (640) and (633) and between (732) and (800) reflections, respectively. Starting with the XRD patterns of Al-LLZO Pre-annealed, the (640) peak has a strong intensity at R1 and the ratio between (640) and (633) decreased first then increased very slightly along the radius of the membrane. The (732) peak was stronger than (800) in the center (R1) but the trend reversed at the edge (R4). On the XRD patterns of Al-LLZO Hot-pressed, at R1 and R4, the (640)/(633) ratio was similar, whereas (640) was weaker than (633) in R2 and R3. For the (732) and (800) peaks, both had similar intensity at
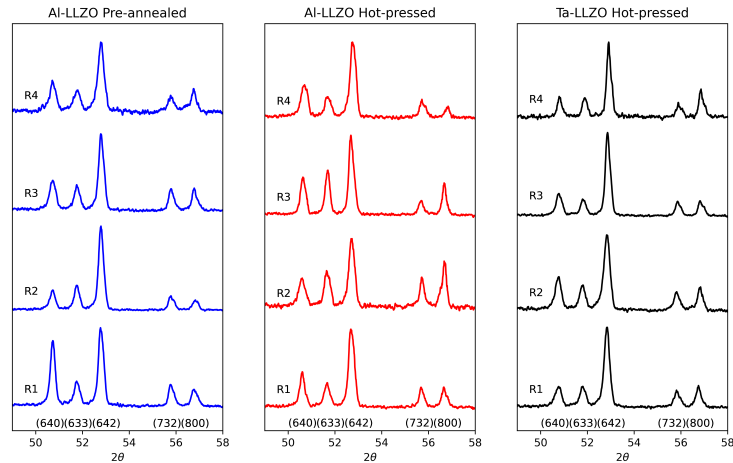
Figure 40. X-Ray Diffraction Patterns of $Li_7La_3Zr_2O_{12}$ Samples at Different Radial Positions, from the Center (R1) to the Edge (R4) of the Membrane

R1, with (800) getting much stronger than (732) at R2 and R3, with the trend reverting at the edge, R4, where (732) had higher intensity. The peak ratios, especially among R1, R2 and R3, were not as variable for Ta-LLZO Hot-pressed as the other two samples, qualitatively.

Since the intensity of reflections depends on the structure factor of that crystallographic plane, the variations observed strongly suggest changes in the exact atomic content of the different regions of each $Li_7La_3Zr_2O_{12}$ sample. The existence of supplementary peaks or asymmetries further bolsters the case for the existence of chemical heterogeneity. However, there were no strong systematic radial trends that could conclusively be correlated with the radial effect on electrochemical performance, aside from the subtle deviations in peak lineshape at the edge of each sample. For example, the lineshape of (732) and (800) peaks became more complex

at the edge (R4) with shoulders of these samples which could be an indication of subtle devia-

tions in local chemical composition such as possible presence of impurities on the outer area of

samples. Nonetheless, since ionic conductivity is shown to be sensitive to the exact composition

of $Li_7La_3Zr_2O_{12}$ and the existence of substituents like Al [74,75], it is important to determine if

this preliminary evidence of chemical heterogeneity across the surface on $Li_7La_3Zr_2O_{12}$ sample

could be linked to local variations in conductivity because they could, in turn, promote the

growth of Li dendrites that degrade the cell.

5.4   Conclusion

In our study, we were able to verify our hypothesis that the gradient in electrochemical

performance along the radial position is the result of the processing conditions of the solid

electrolyte by showing the trends of the average deviatoric strain using μX-ray Laue diffraction.

We observed a clear difference of deviatoric strain coverage between the samples that were

processed differently (annealed vs hot-pressed). The annealed sample was dominated by com-

pressive strain while both hot-pressed samples show deviatoric strain gradients from the edge

of the membrane to the center, tensile to compressive respectively. This observation suggested

the annealed sample is more densified on the zz direction. Our data for both hot-pressed not

only shows that deviatoric gradients formed along the radial position, but also that the ab-

solute value of strain is larger at the edge than the rest of the membrane. This observation

suggests a stronger deformation of the cubic symmetry of the compound at the edge of the

membrane, which would induce a reduction in ionic conductivity that could explain the better

electrochemical performance observed from CCD test when lithium only covers the center of the membranes.

Mapping of the samples with Bragg μX-ray diffraction revealed notable differences in the relative intensity of reflections depending on sample location. While observations of the 2D XRD patterns did not support the existence of effects of texturing due to the limited number of crystallites probed, the cause of the change in relative peak intensity could not be identified as this work is limited by the number of the patterns collected. As a result, these observations are left as motivation for a future study with X-ray mapping.

In summary, XRD mapping techniques presented in this chapter explored how spatial variations in electrochemical performance of solid electrolytes could be linked to their microstructural change. Our work demonstrated that the measurement of deviatroic strain could detect local atomic deformations resulting from the processing conditions of the membranes, correlated with the spatial effects observed in tests evaluating the ability of the electrolyte membranes to withstand short circuits.

CHAPTER 6

CONCLUSIONS

This thesis demonstrated applications of μXRD to visualize the heterogeneity in layered cathode materials $LiNi_{0.80}Co_{0.15}Al_{0.05}O_2$ and garnet-typed solid electrolytes $Li_7La_3Zr_2O_{12}$ for lithium batteries. The mapping techniques in this thesis provided insight into the kinetics of NCA phase transformation under different galvanostatic cycling conditions by showing structural heterogeneity of $LiNi_{0.80}Co_{0.15}Al_{0.05}O_2$ at both particle and electrode level. The gradient in quality of Li electrodeposition induced by deviatoric strain and microstructure of $Li_7La_3Zr_2O_{12}$ were also evaluated both qualitatively and quantitatively.

Ex situ μXRD mapping was demonstrated in Chapter 3 on $LiNi_{0.80}Co_{0.15}Al_{0.05}O_2$ electrode subject to different storage conditions. Heterogeneity in the contents of Li within the NCA cathode was identified through analysis of PXRD in materials stored in air, due to the formation of insulating impurities on the surface of the particles, such as Li_2CO_3. μXRD mapping spatially located the gradients in the form of two distinct compositional domains at different delithiation states within the NCA-air sample. The phase domains on the resulting maps were consistent with the analysis through bulk PXRD, which verified the accuracy of evaluation. These gradients were found to match a model by which Li transport was detrimentally affected by the insulating impurities on the oxide, leading to preferential delithiation in domains directly facing the anode. With appropriate protection under inert atmosphere, no gradients

were found, indicating that transport within the electrode could compensate the gradients in charge supply in the cell.

Application of *operando* μXRD mapping with small beams was presented in Chapter 4 to study the pathways of phase transformation of single NCA secondary particles. By observing the evolution of selected diffraction peaks (003) and (104), the overall trend of the NCA phase transformation was monitored, which revealed compositional gradients existed within the NCA particles during cycling at C/8, in contrast to a previous study on NCA particles with a similar technique but slower rate. As a result, this heterogeneity of chemical states was postulated to result from increased applied rate, which led to limitations of diffusion in individual particles. The limitations of our *operando* μXRD mapping methodology appeared when the applied rate was raised to C/3. Much less activity was observed in these conditions, including inactive particles, which indicated possible problems of local electrical connection within the particles in the custom-made cell at fast rates. The improvement of the electrochemical versatility of this mapping technique should be considered when fast applied rates are required.

The goal of Chapter 5 was to investigate the correlation between microstructural changes and gradients of critical current density observed when Li is plated using different membranes based on derivatives of LLZO as solid electrolyte. The measurement of local deviatoric strain, ε, using Laue X-ray diffraction established a correlation whereby locally lower values of CCD are associated with the existence of tensile stress in the membrane. Maps visualized the heterogeneity of deviatoric strain along the zz direction across the surface of the LLZO samples, verifying a clear radial trend of ε_{zz} for hot-pressed samples. Measurements of μXRD also revealed local

variations in peak intensity and lineshape that could be related to chemical heterogeneity which

must be probed in future work.

APPENDICES

Appendix A

PERMISSIONS

Appendix A (Continued)

CCC Marketplace™

This is a License Agreement between Chao Li ("User") and Copyright Clearance Center, Inc. ("CCC") on behalf of the Rightsholder identified in the order details below. The license consists of the order details, the CCC Terms and Conditions below, and any Rightsholder Terms and Conditions which are included below.
All payments must be made in full to CCC in accordance with the CCC Terms and Conditions below.

Order Date	07-Jul-2021	Type of Use	Republish in a thesis/dissertation
Order License ID	1131338-1	Publisher	ROYAL SOCIETY OF CHEMISTRY
ISSN	1460-4744	Portion	Image/photo/illustration

LICENSED CONTENT

Publication Title	Chemical Society reviews	Publication Type	e-Journal
Article Title	Lithium and sodium battery cathode materials: computational insights into voltage, diffusion and nanostructural properties.	Start Page	185
		End Page	204
		Issue	1
Author/Editor	Royal Society of Chemistry (Great Britain)	Volume	43
Date	12/31/1971	URL	http://www.rsc.org/csr
Language	English		
Country	United Kingdom of Great Britain and Northern Ireland		
Rightsholder	Royal Society of Chemistry		

REQUEST DETAILS

Portion Type	Image/photo/illustration	Distribution	United States
Number of images / photos / illustrations	1	Translation	Original language of publication
Format (select all that apply)	Print, Electronic	Copies for the disabled?	No
Who will republish the content?	Academic institution	Minor editing privileges?	Yes
Duration of Use	Current edition and up to 5 years	Incidental promotional use?	No
Lifetime Unit Quantity	Up to 499	Currency	USD
Rights Requested	Main product		

NEW WORK DETAILS

Title	Visualization of Heterogeneity in Materials for Lithium Batteries Using Micro X-ray Diffraction	Institution name	University of Illinois at Chicago
		Expected presentation date	2021-07-16
Instructor name	Chao Li		

ADDITIONAL DETAILS

Order reference number	N/A	The requesting person / organization to appear on the license	Chao Li

REUSE CONTENT DETAILS

Title, description or numeric reference of the portion(s)	Figure 3	Title of the article/chapter the portion is from	Lithium and sodium battery cathode materials: computational insights into voltage, diffusion and nanostructural properties.
Editor of portion(s)	Islam, M. Saiful; Fisher, Craig A. J.		
Volume of serial or monograph	43	Author of portion(s)	Islam, M. Saiful; Fisher, Craig A. J.
Page or page range of portion	185-204	Issue, if republishing an article from a serial	1
		Publication date of portion	2013-12-01

Figure 41. Permission for Figure 2

Appendix A (Continued)

CCC Marketplace™

This is a License Agreement between Chao Li ("User") and Copyright Clearance Center, Inc. ("CCC") on behalf of the Rightsholder identified in the order details below. The license consists of the order details, the CCC Terms and Conditions below, and any Rightsholder Terms and Conditions which are included below.
All payments must be made in full to CCC in accordance with the CCC Terms and Conditions below.

Order Date	07-Jul-2021	Type of Use	Republish in a thesis/dissertation
Order License ID	1131346-1	Publisher	Royal Society of Chemistry
ISSN	2050-7496	Portion	Image/photo/illustration

LICENSED CONTENT

Publication Title	Journal of materials chemistry. A, Materials for energy and sustainability	Publication Type	e-Journal
		Start Page	23628
Article Title	Probing and Quantifying Cathode Charge Heterogeneity in Li Ion Batteries	End Page	23661
Author/Editor	Royal Society of Chemistry (Great Britain)	Issue	41
Date	12/31/2012	Volume	7
Language	English	URL	http://pubs.rsc.org/en/journals/journalissues/ta
Country	United Kingdom of Great Britain and Northern Ireland		
Rightsholder	Royal Society of Chemistry		

REQUEST DETAILS

Portion Type	Image/photo/illustration	Distribution	United States
Number of images / photos / illustrations	1	Translation	Original language of publication
Format (select all that apply)	Print, Electronic	Copies for the disabled?	No
Who will republish the content?	Academic institution	Minor editing privileges?	Yes
Duration of Use	Life of current edition	Incidental promotional use?	No
Lifetime Unit Quantity	Up to 499	Currency	USD
Rights Requested	Main product		

NEW WORK DETAILS

Title	Visualization of Heterogeneity in Materials for Lithium Batteries Using Micro X-ray Diffraction	Institution name	University of Illinois at Chicago
		Expected presentation date	2021-07-16
Instructor name	Chao Li		

ADDITIONAL DETAILS

Order reference number	N/A	The requesting person / organization to appear on the license	Chao Li

REUSE CONTENT DETAILS

Title, description or numeric reference of the portion(s)	Fig 1	Title of the article/chapter the portion is from	Probing and Quantifying Cathode Charge Heterogeneity in Li Ion Batteries
Editor of portion(s)	Tian, Chixia; Yang, Zhijie; Zhang, Yuxin	Author of portion(s)	Tian, Chixia; Yang, Zhijie; Zhang, Yuxin
Volume of serial or monograph	7	Issue, if republishing an article from a serial	41
Page or page range of portion	23628-23661	Publication date of portion	2018-12-31

Figure 42. Permission for Figure 3

Appendix A (Continued)

CCC Marketplace™

This is a License Agreement between Chao Li ("User") and Copyright Clearance Center, Inc. ("CCC") on behalf of the Rightsholder identified in the order details below. The license consists of the order details, the CCC Terms and Conditions below, and any Rightsholder Terms and Conditions which are included below.
All payments must be made in full to CCC in accordance with the CCC Terms and Conditions below.

Order Date	07-Jul-2021	Type of Use	Republish in a thesis/dissertation
Order License ID	1131368-1	Publisher	John Wiley & Sons
ISBN-13	9780470502648	Portion	Image/photo/illustration

LICENSED CONTENT

Publication Title	Two-dimensional X-ray Diffraction	Country	United States of America
Author/Editor	He	Rightsholder	John Wiley & Sons - Books
Date	11/12/2009	Publication Type	e-Book
Language	English		

REQUEST DETAILS

Portion Type	Image/photo/illustration	Distribution	United States
Number of images / photos / illustrations	3	Translation	Original language of publication
Format (select all that apply)	Print, Electronic	Copies for the disabled?	No
Who will republish the content?	Academic institution	Minor editing privileges?	Yes
Duration of Use	Life of current edition	Incidental promotional use?	No
Lifetime Unit Quantity	Up to 499	Currency	USD
Rights Requested	Main product		

NEW WORK DETAILS

Title	Visualization of Heterogeneity in Materials for Lithium Batteries Using Micro X-ray Diffraction	Institution name	University of Illinois at Chicago
		Expected presentation date	2021-07-16
Instructor name	Chao Li		

ADDITIONAL DETAILS

The requesting person / organization to appear on the license	Chao Li

REUSE CONTENT DETAILS

Title, description or numeric reference of the portion(s)	Figure 1.10, Figure 3.5 and Figure 3.6	Title of the article/chapter the portion is from	Chapter 1 and Chapter 3
Editor of portion(s)	N/A	Author of portion(s)	He
Volume of serial or monograph	N/A	Publication date of portion	2009-11-12
Page or page range of portion	14, 62-63		

RIGHTSHOLDER TERMS AND CONDITIONS

No right, license or interest to any trademark, trade name, service mark or other branding ("Marks") of WILEY or its licensors is granted hereunder, and you agree that you shall not assert any such right, license or interest with respect thereto. You may not alter, remove or suppress in any manner any copyright, trademark or other notices displayed by the Wiley material. This Agreement will be void if the Type of Use, Format, Circulation, or Requestor Type was misrepresented during the licensing process. In no instance may the total amount of Wiley Materials used in any Main Product, Compilation or Collective work comprise more than 5% (if figures/tables) or 15% (if full articles/chapters) of the (entirety of the) Main Product, Compilation or Collective Work. Some titles may be available under an Open Access license. It is the Licensors' responsibility to identify the type of Open Access license on which the requested material was published, and comply fully with the terms of that license for the type of use specified Further details can be found on Wiley Online Library http://olabout.wiley.com/WileyCDA/Section/id-410895.html.

Figure 43. Permission for Figure 4 and Figure 6

Appendix A (Continued)

Figure 44. Permission for Figure 5

Appendix A (Continued)

CCC
RightsLink®

Home Help Live Chat Chao Li ∨

In situ Visualization of State-of-Charge Heterogeneity within a LiCoO2 Particle that Evolves upon Cycling at Different Rates

Author: Yahong Xu, Enyuan Hu, Kai Zhang, et al

ACS Publications
Most Trusted. Most Cited. Most Read.

Publication: ACS Energy Letters

Publisher: American Chemical Society

Date: May 1, 2017

Copyright © 2017, American Chemical Society

PERMISSION/LICENSE IS GRANTED FOR YOUR ORDER AT NO CHARGE

This type of permission/license, instead of the standard Terms and Conditions, is sent to you because no fee is being charged for your order. Please note the following:

- Permission is granted for your request in both print and electronic formats, and translations.
- If figures and/or tables were requested, they may be adapted or used in part.
- Please print this page for your records and send a copy of it to your publisher/graduate school.
- Appropriate credit for the requested material should be given as follows: "Reprinted (adapted) with permission from {COMPLETE REFERENCE CITATION}. Copyright {YEAR} American Chemical Society." Insert appropriate information in place of the capitalized words.
- One-time permission is granted only for the use specified in your RightsLink request. No additional uses are granted (such as derivative works or other editions). For any uses, please submit a new request.

If credit is given to another source for the material you requested from RightsLink, permission must be obtained from that source.

BACK   CLOSE WINDOW

Figure 45. Permission for Figure 7

terms and conditions of use

General

Figure 46. Permission for Figure 9

Appendix A (Continued)

CCC Marketplace™

This is a License Agreement between Chao Li ("User") and Copyright Clearance Center, Inc. ("CCC") on behalf of the Rightsholder identified in the order details below. The license consists of the order details, the CCC Terms and Conditions below, and any Rightsholder Terms and Conditions which are included below.
All payments must be made in full to CCC in accordance with the CCC Terms and Conditions below.

Order Date	07-Jul-2021	Type of Use	Republish in a thesis/dissertation
Order License ID	1131378-1	Publisher	IOP Publishing
ISSN	1945-7111	Portion	Chart/graph/table/figure

LICENSED CONTENT

Publication Title	Journal of the Electrochemical Society	Rightsholder	IOP Publishing, Ltd
Article Title	Mapping and Metastability of Heterogeneity in LiMn2O4 Battery Electrodes with High Energy Density	Publication Type	e-Journal
		Start Page	020526
		Issue	2
Author/Editor	Electrochemical Society.	Volume	167
Date	12/31/1947	URL	http://www.scitation.org/JES
Language	English		
Country	United States of America		

REQUEST DETAILS

Portion Type	Chart/graph/table/figure	Distribution	United States
Number of charts / graphs / tables / figures requested	1	Translation	Original language of publication
		Copies for the disabled?	No
Format (select all that apply)	Print, Electronic	Minor editing privileges?	Yes
Who will republish the content?	Academic institution	Incidental promotional use?	No
Duration of Use	Life of current edition	Currency	USD
Lifetime Unit Quantity	Up to 499		
Rights Requested	Main product		

NEW WORK DETAILS

Title	Visualization of Heterogeneity in Materials for Lithium Batteries Using Micro X-ray Diffraction	Institution name	University of Illinois at Chicago
		Expected presentation date	2021-07-16
Instructor name	Chao Li		

ADDITIONAL DETAILS

Order reference number	N/A	The requesting person / organization to appear on the license	Chao Li

REUSE CONTENT DETAILS

Title, description or numeric reference of the portion(s)	Figure S13	Title of the article/chapter the portion is from	Mapping and Metastability of Heterogeneity in LiMn2O4 Battery Electrodes with High Energy Density
Editor of portion(s)	Cabana, Jordi; Khawaja, Sara; Wolfman, Mark	Author of portion(s)	Cabana, Jordi; Khawaja, Sara; Wolfman, Mark
Volume of serial or monograph	167		
Page or page range of portion	020526	Issue, if republishing an article from a serial	2
		Publication date of portion	2020-01-22

RIGHTSHOLDER TERMS AND CONDITIONS

These special terms and conditions are in addition to the standard terms and conditions for CCC's Republication Service and, together with those standard terms and conditions, govern the use of the Works. As the User you will make all reasonable efforts to contact the author(s) of the article which the Work is to be reused from, to seek consent for your intended use. Contacting one author who is acting expressly as authorised agent for their co-author(s) is acceptable. User will reproduce the following wording prominently alongside the Work: the source of the Work, including author, article title, title of journal, volume number, issue number (if relevant), page range (or first page if this is the only information available) and date of first publication; and a link back to the article (via DOI); and if practicable, and IN ALL CASES for new works published under any of the Creative Commons licences, the words "© The Electrochemical Society. Reproduced by permission of IOP Publishing Ltd. All rights reserved" Without the express permission of the author(s) and the Rightsholder of the article from which the Work is to be reused, User shall not use it in any way which, in the opinion of IOP Publishing Ltd, could: (i) distort or alter the author(s)' original intention(s) and meaning; (ii) be prejudicial to the honour or reputation of the author(s); and/or (iii) imply endorsement by the author(s) and/or the Rightsholder and/or IOP Publishing Ltd. This licence does not apply to any article which is credited to another source and which does not have the copyright line '© The Electrochemical Society'. User must check the copyright line of the article from which the Work is to be reused to check that the Electrochemical Society and IOP Publishing Ltd has all the necessary rights to be able to grant permission. User is solely responsible for identifying and obtaining separate licences and permissions from the copyright owner for reuse of any such third party material/figures which the Rightsholder is not the copyright owner of. The Rightsholder shall not reimburse any fees which User pays for a republication license for such third party content. This licence does not apply to any material/figure which is credited to another source in the Rightsholder's publication or has been obtained from a third party. User must check the Version of Record of the article from which the Work is to be reused, to check whether any of the material in the Work is third party material. Third party citations and/or copyright notices and/or permissions statements may not be included in any other version of the article from which the Work is to be reused and so cannot be relied upon by the User. User is solely responsible for identifying and obtaining separate licences and permissions from the copyright owner for reuse of any such third party material/figures where the Rightsholder is not the copyright owner. The Rightsholder shall not reimburse any fees which User pays for a republication license for such third party content. User and CCC acknowledge that IOP Publishing Ltd and/or the Rightsholder may, from time to time, make changes or additions to these special terms and conditions without express notification, provided that these shall not apply to permissions already secured and paid for by User prior to such change or addition. User acknowledges that the Rightsholder and IOP Publishing Ltd (which includes companies within its group and third parties for whom it publishes its titles) may make use of personal data collected through the service in the course of their business. If User is the author of the Work, User may automatically have the right to reuse it under the rights granted back when User transferred the copyright in the article to the Rightsholder. User should check the copyright form and the relevant author rights policy to check whether permission is required. If User is the author of the Work and does require permission for proposed reuse of the Work, User should select 'Author of requested content' as the Requestor Type. The Rightsholder shall not reimburse any fees which User pays for a republication license. If User is the author of the article which User wishes to reuse in User's thesis or dissertation, the republication licence covers the right to include the Version of Record of the article, provided it is not then published commercially. User must include citation details and, for online use, a link to the Version of Record of the article on the IOPscience website. User may need to obtain separate permission for any third party content included within the article. User must check this with the copyright owner of such third party content. User may not include the article in a thesis or dissertation which is published by ProQuest. Any other commercial use of User's thesis or dissertation containing the article would also need to be expressly notified in writing to the Rightsholder at the time of request and would require separate written permission from the Rightsholder. As well as CCC, the Rightsholder and IOP Publishing Ltd shall have the right to bring any legal action that they deem necessary to enforce their rights should they consider that the Work infringes those rights in any way. For content reuse requests that qualify for permission under the STM Permissions Guidelines, which may be updated from time to time, the STM Permissions Guidelines supplement the terms and conditions contained in this license.

Figure 47. Permission for Figure 10

Appendix A (Continued)

Rightslink® by Copyright Clearance Center

CCC
RightsLink®

Home | Help | Live Chat | Sign in | Create Account

ACS Publications
Most Trusted. Most Cited. Most Read.

Activation Mechanism of LiNi0.80Co0.15Al0.05O2: Surface and Bulk Operando Electrochemical, Differential Electrochemical Mass Spectrometry, and X-ray Diffraction Analyses

Author: Rosa Robert, Christa Bünzli, Erik J. Berg, et al

Publication: Chemistry of Materials

Publisher: American Chemical Society

Date: Jan 1, 2015

Copyright © 2015, American Chemical Society

PERMISSION/LICENSE IS GRANTED FOR YOUR ORDER AT NO CHARGE

This type of permission/license, instead of the standard Terms & Conditions, is sent to you because no fee is being charged for your order. Please note the following:

- Permission is granted for your request in both print and electronic formats, and translations.
- If figures and/or tables were requested, they may be adapted or used in part.
- Please print this page for your records and send a copy of it to your publisher/graduate school.
- Appropriate credit for the requested material should be given as follows: "Reprinted (adapted) with permission from (COMPLETE REFERENCE CITATION). Copyright (YEAR) American Chemical Society." Insert appropriate information in place of the capitalized words.
- One-time permission is granted only for the use specified in your request. No additional uses are granted (such as derivative works or other editions). For any other uses, please submit a new request.
- If credit is given to another source for the material you requested, permission must be obtained from that source.

BACK   CLOSE WINDOW

Figure 48. Permission for Figure 11, Figure 19 and Figure 20

Appendix A (Continued)

Figure 49. Permission for Figure 21

Appendix A (Continued)

CCC
RightsLink®

Home   Help   Live Chat   Chao Li ∨

Origin of the Phase Transition in Lithium Garnets

ACS Publications
Most Trusted. Most Cited. Most Read.

Author: Fei Chen, Junyang Li, Zhifeng Huang, et al
Publication: The Journal of Physical Chemistry C
Publisher: American Chemical Society
Date: Feb 1, 2018

Copyright © 2018, American Chemical Society

PERMISSION/LICENSE IS GRANTED FOR YOUR ORDER AT NO CHARGE

This type of permission/license, instead of the standard Terms and Conditions, is sent to you because no fee is being charged for your order. Please note the following:

- Permission is granted for your request in both print and electronic formats, and translations.
- If figures and/or tables were requested, they may be adapted or used in part.
- Please print this page for your records and send a copy of it to your publisher/graduate school.
- Appropriate credit for the requested material should be given as follows: "Reprinted (adapted) with permission from {COMPLETE REFERENCE CITATION}. Copyright {YEAR} American Chemical Society." Insert appropriate information in place of the capitalized words.
- One-time permission is granted only for the use specified in your RightsLink request. No additional uses are granted (such as derivative works or other editions). For any uses, please submit a new request.

If credit is given to another source for the material you requested from RightsLink, permission must be obtained from that source.

BACK   CLOSE WINDOW

Figure 50. Permission for Figure 34

Appendix A (Continued)

CCC Marketplace™

This is a License Agreement between Chao Li ("User") and Copyright Clearance Center, Inc. ("CCC") on behalf of the Rightsholder identified in the order details below. The license consists of the order details, the CCC Terms and Conditions below, and any Rightsholder Terms and Conditions which are included below.
All payments must be made in full to CCC in accordance with the CCC Terms and Conditions below.

Order Date	07-Jul-2021	Type of Use	Republish in a thesis/dissertation
Order License ID	1131386-1	Publisher	ELSEVIER BV
ISSN	1369-7021	Portion	Chart/graph/table/figure

LICENSED CONTENT

Publication Title	Materials today	Rightsholder	Elsevier Science & Technology Journals
Article Title	Li-ion battery materials: present and future	Publication Type	Journal
Author/Editor	European Materials Research Society.	Start Page	252
Date	12/31/1997	End Page	264
Language	English	Issue	5
Country	Netherlands	Volume	18

REQUEST DETAILS

Portion Type	Chart/graph/table/figure	Distribution	United States
Number of charts / graphs / tables / figures requested	1	Translation	Original language of publication
		Copies for the disabled?	No
Format (select all that apply)	Print, Electronic	Minor editing privileges?	Yes
Who will republish the content?	Academic institution	Incidental promotional use?	No
Duration of Use	Life of current edition	Currency	USD
Lifetime Unit Quantity	Up to 499		
Rights Requested	Main product		

NEW WORK DETAILS

Title	Visualization of Heterogeneity in Materials for Lithium Batteries Using Micro X-ray Diffraction	Institution name	University of Illinois at Chicago
		Expected presentation date	2021-07-16
Instructor name	Chao Li		

ADDITIONAL DETAILS

Order reference number	N/A	The requesting person / organization to appear on the license	Chao Li

REUSE CONTENT DETAILS

Title, description or numeric reference of the portion(s)	Table I	Title of the article/chapter the portion is from	Li-ion battery materials: present and future
Editor of portion(s)	Nitta, Naoki; Wu, Feixiang; Lee, Jung Tae; Yushin, Gleb	Author of portion(s)	Nitta, Naoki; Wu, Feixiang; Lee, Jung Tae; Yushin, Gleb
Volume of serial or monograph	18	Issue, if republishing an article from a serial	5
Page or page range of portion	252-264		
		Publication date of portion	2015-05-31

RIGHTSHOLDER TERMS AND CONDITIONS

Elsevier publishes Open Access articles in both its Open Access journals and via its Open Access articles option in subscription journals, for which an author selects a user license permitting certain types of reuse without permission. Before proceeding please check if the article is Open Access on http://www.sciencedirect.com and refer to the user license for the individual article. Any reuse not included in the user license terms will require permission. You must always fully and appropriately credit the author and source. If any part of the material to be used (for example, figures) has appeared in the Elsevier publication for which you are seeking permission, with credit or acknowledgement to another source it is the responsibility of the user to ensure their reuse complies with the terms and conditions determined by the rights holder. Please contact permissions@elsevier.com with any queries.

Figure 51. Permission for Table I

CITED LITERATURE

1. Islam, M. S. and Fisher, C. A. J.: Lithium and sodium battery cathode materials: computational insights into voltage, diffusion and nanostructural properties. Chemical Society Reviews, 43:185–204, 2014.

2. Zhang, Y., Yang, Z., and Tian, C.: Probing and quantifying cathode charge heterogeneity in Li ion batteries. Journal of Materials Chemistry A, 7:23628–23661, 2019.

3. He, B. B.: Two-Dimensional X-ray Diffraction. John Wiley & Sons, Inc, 2009.

4. Maser, J., Stephenson, B., Winarski, R., Benson, C., Shu, D., Lai, B., Vogt, S., and Holt, M.: Development of a hard X–ray nanoprobe beamline at the advanced photon source. Microsopy and Microanalysis, 11(S02):680–681, 2005.

5. Xu, Y., Hu, E., Zhang, K., Wang, X., Borzenets, V., Sun, Z., Pianetta, P., Yu, X., Liu, Y., Yang, X.-Q., and Li, H.: In situ visualization of state-of-charge heterogeneity within a $LiCoO_2$ particle that evolves upon cycling at different rates. ACS Energy Letters, 2:1240–1245, 2017.

6. Boriewicz, O. J., Shyam, B., Wiaderek, K. M., Kurtz, C., Chupas, P. J., and Chapman, K. W.: The AMPIX electrocehmcial cell: a versatile apparatus for in situ X-ray scattering and spectroscopic measurements. Journal of Applied Crystallography, 45:1261–1269, 2012.

7. Wolfman, M., Khawaja, S., and Cabana, J.: Mapping and metastability of heterogeneity in $LiMn_2O_4$ battery electrodes with high energy density. Journal of the Electrochemical Society, 167(2):020526, 2020.

8. Robert, R., Bunzli, C., Berg, E. J., and Petr, N.: Activation mechanism of $LiNi_{0.80}Co_{0.15}Al_{0.05}O_2$: surface and bulk operando electrochemical, differential electrochemcial mass spectrometry, and X-ray diffraction analyses. Chemistry of Materials, 27:526–536, 2015.

9. Grenier, A., Liu, H., Wiaderek, K., Lebens-Higgins, Z., Borkiewicz, O., Piper, L., Chupas, P., and Chapman, K.: Reaction heterogeneity in $LiNi_{0.80}Co_{0.15}Al_{0.05}O_2$ induced by surface layer. Chemistry of Materials, 29:7345–7352, 2017.

10. Liu, H., Wolf, M., Karki, K., Yu, Y.-S., Stach, E. A., Cabana, J., Chapman, K. W., and Chupas, P. J.: Intergranular cracking as a major cause of long-term capacity fading of layered cathodes. Nano Letters, 17(6):3452–3457, 2017.

11. May, B.: Probing Phase Transformations in Lithium Ion Cathode Materials Using X-ray Imaging. University of Illinois at Chicago, 2018.

12. Chen, F., Li, J., Huang, Z., Yang, Y., Shen, Q., and Zhang, L.: Origin of the phase transition in lithium garnets. The Journal of Physical Chemistry, 122(4):1963–1972, 2018.

13. Nitta, N., Wu, F., Lee, J. T., and Yushin, G.: Li-ion battery materials: present and future. Materials Today, 18:252–264, 2015.

14. Tarascon, J. and Armand, M.: Issues and challenges facing rechargeable lithium batteries. Nature, 414(6861):359–367, 2001.

15. Wang, J., Purewal, J., Liu, P., Hicks-Garner, J., Soukazian, S., Sherman, E., Sorenson, A., Vu, L., Tataria, H., and Verbrugge, M. W.: Degradation of lithium ion batteries employing graphite negatives and nickel-cobalt-manganese oxide + spinel manganese oxide positives: Part 1, aging mechanisms and life estimation. Journal of Power Sources, 269:937–348, 2014.

16. Watanabe, N. and Fukuda, M.: Primary cell for electric batteries. U.S. Patent 3536532A, 1970.

17. Zhang, J.-G., Xu, W., and Henderson, W. A.: Lithium Metal Anodes and Rechargeable Lithium Metal Batteries. Springer, 2017.

18. Yang, H., Li, J., Sun, Z., Fang, R., Wang, D.-W., He, K., Cheng, H.-M., and Li, F.: Reliable liquid electrolytes for lithium metal batteries. Energy Storage Materials, 30:113–129, 2020.

19. Akira, Y., Takayuki, N., and Kenichi, S.: Secondary battery. U.S. Patent 4668595A, 1985.

20. Newman, J. and Thomas-alyea, K.: Electrochemical Systems. John Wiley Sons, Inc., 2004.

21. Feng, F., Hu, X., Hu, L., Hu, F., Li, Y., and Zhang, L.: Propagation mechanisms and diagnosis of parameter inconsistency within Li-ion battery packs. Renewable and Sustainable Energy Reviews, 112:102–113, 2019.

22. Whittingham, M.: Lithium batteries and cathode materials. Chemical Reviews, 104(10):4271–4302, 2004.

23. Luo, X., Pan, W., Liu, H., Gong, J., and Wu, H.: Glass fiber fabric mat as the separator for lithium-ion battery with high safety performance. Ionics, 21:3135–3139, 2015.

24. Wagner, R., Redhammer, G. J., Rettenwander, D., Senyshyn, A., Schmidt, W., Wilkening, M., and Amthauer, G.: Crystal stucture of garnet-related Li-ion conductor $Li_{7-3x}Ga_xLa_3Zr_2O_{12}$: Fast Li-ion conduction caused by a different cubic modification? Chemistry of Materials, 28:1861–1871, 2016.

25. Jain, A., Ong, S. P., Hautier, G., Chen, W., Richards, W. D., Dacek, S., Cholia, S., Gunter, D., Skinner, D., Ceder, G., and Persson, K. A.: Commentary: The materials project: A materials genome approach to accelerating materials innovation. APL Materials, 1(1):011002, 2013.

26. Cho, J., Kim, Y.-W., Kim, B., Lee, J.-G., and Park, B.: A breakthrough in the safety of lithiumsecondary batteries by coating the cathodematerial with $AlPO_4$ nanoparticles. Angewandte Chemie International Edition, 42(14):1618–21, 2003.

27. Ohzuku, T., Ueda, A., and Nagayama, M.: Electrochemistry and structural chemistry of $LiNiO_2$ (R3m) for 4 volt secondary lithium cells. Journal of The Electrochemical Society, 140:1862–1870, 1993.

28. Bruce, P., Robert Armstrong, A., and Gitzendanner, R.: New intercalation compounds for lithium batteries: layered $LiMnO_2$. Journal of Materials Chemistry, 9:193–198, 1999.

29. Lin, F., Markus, I. M., Nordlund, D., Weng, T.-C., D., A. M., Xin, H. L., and Doeff, M. M.: Surface reconstruction and chemical evolution of stoichiometric layered cathode materials for lithium-ion batteries. Nature Communications, 5(1):3529, 2014.

30. Martha, S. K., Haik, O., Zinigrad, E., Exnar, I., Drezen, T., Miners, J. H., and Aurbach, D.: On the thermal stability of olivine cathode materials for lithium-ion batteries. Journal of The Electrochemical Society, 158(10):A1115, 2011.

31. Wang, R., He, X., He, L., Wang, F., Xiao, R., Gu, L., Li, H., and Chen, L.: Atomic structure of Li_2MnO_3 after partial delithiation and re-lithiation. Advanced Energy Materials, 3:1358–1367, 2013.

32. Lee, M.-J., Lee, S., Oh, P., Kim, Y., and Cho, J.: High performance $LiMn_2O_4$ cathode materials grown with epitaxial layered nanostructure for Li-ion batteries. Nano Letters, 14, 2014.

33. Choi, S.and Manthiram, A.: Synthesis and electrochemical properties of $LiCo_2O_4$ spinel cathodes. Journal of the Electrochemical Society, 149, 2002.

34. Yamada, A., Chung, S., and Hinokuma, K.: Optimized $LiFePO_4$ for lithium battery cathodes. Journal of the Electrochemical Society, 149(2):993–9, 2001.

35. Choi, D., Wang, D., Bae, I.-T., Xiao, J., Nie, Z., Wang, W., Viswanathan, V. V., Lee, Y. J., Zhang, J.-G., Graff, G. L., Yang, Z., and Liu, J.: $LiMnPO_4$ nanoplate grown via solid-state reaction in molten hydrocarbon for Li-ion battery cathode. Nano Letter, 10(8):2799–2805, 2010.

36. Lloris, J. M., Vicente, C. P., and Tirado, J. L.: Improvement of the electrochemical performance of $LiCoPO_4$ 5 V material using a novel synthesis procedure. Electrochemical and Solid-State Letters, 5(10):A234, 2002.

37. Sobkowiak, A., Roberts, M. R., Younesi, R., Ericsson, T., Häggström, L., Tai, C.-W., Andersson, A. M., Edström, K., Gustafsson, T., and Björefors, F.: Understanding and controlling the surface chemistry of $LiFeSO_4F$ for an enhanced cathode functionality. Chemistry of Materials, 25(15):3020, 2013.

38. Barker, J., Gover, R., Burns, P., Bryan, A., Saidi, M., and Swoyer, J.: Structural and electrochemical properties of lithium vanadium fluorophosphate, $LiVPO_4F$. Journal of Power Sources, 146(1–2):516–520, 2005.

39. Kalyani, P. and Kalaiselvi, N.: Various aspects of $LiNiO_2$ chemistry: A review. Science and Technology of Advanced Materials, 6(6):689–703, 2005.

40. Gu, M., Belharouak, I., Zheng, J., Wu, H., Xiao, J., Genc, A., Amine, K., Thevuthasan, S., Baer, D. R., Zhang, J.-G., Browning, N. D., Liu, J., and Wang, C.: Formation of the spinel phase in the layered composite cathode used in Li-ion batteries. ACS Nano, 7(1):760–767, 2013.

41. J.Tu, X.B.Zhao, G.S.Cao, D.G.Zhuang, T.J.Zhu, and J.P.Tu: Enhanced cycling stability of LiMn$_2$O$_4$ by surface modification with melting impregnation method. Electrochimica Acta, 51(28):6456–6462, 2006.

42. Golubkov, A. W., Scheikl, S., Planteu, R., Voitic, G., Wiltsche, H., Stangl, C., Fauler, G., Thalera, A., and Hackerb, V.: Thermal runaway of commercial 18650 Li-ion batteries with LFP and NCA cathodes – impact of state of charge and overcharge. RSC Advances, 5:57171–57186, 2015.

43. Wan, D. Y., Fan, Z. Y., Dong, Y. X., Baasanjav, E., Jun, H.-B., Jin, B., Jin, E. M., and Jeong, S. M.: Effect of metal (Mn, Ti) doping on NCA cathode materials for lithium ion batteries. Journal of Nanomaterials, pages 1–9, 2018.

44. Mohanty, D., Dahlberg, K., King, D. M., David, L. A., Sefat, A. S., Wood, D. L., Daniel, C., Dhar, S., Mahajan, V., Lee, M., and Albano, F.: Modification of Ni-rich FCG NMC and NCA cathodes by atomic layer deposition: Preventing surface phase transitions for high-voltage lithium-ion batteries. Scientific Reports, 6(26532), 2016.

45. Takada, K.: Progress and prospective of solid-state lithium batteries. Acta Materialia, 61(3):759–770, 2013.

46. Awaka, J., Kijima, N., Hayakawa, H., and Akimoto, J.: Synthesis and structure analysis of tetragonal Li$_7$La$_3$Zr$_2$O$_{12}$ with the garnet-related type structure. Journal of Solid State Chemistry, 182(8):2046–2052, 2009.

47. Murguan, R. and Weppner, W.: Solid Electrolytes for Advanced Applications. Springer, 2019.

48. Tadanaga, K., Takano, R., Ichinose, T., Mori, S., Hayashi, A., and Tatsumisago, M.: Low temperature synthesis of highly ion conductive li$_7$la$_3$zr$_2$o$_{12}$–li$_3$bo$_3$ composites. Electrochemistry Communications, 33:51–54, 2013.

49. Zhu, Y., Connell, J. G., Tepavcevic, S., Zapol, P., Regina Garcia-Mendez, N. J. T., Sakamoto, J., Ingram, B. J., Curtiss, L. A., Freeland, J. W., Fong, D. D., and Markovic, N. M.: Dopant-dependent stability of garnet solid electrolyte interfaces with lithium metal. Advanced Energy Materials, 9, 2019.

50. Kang, S. G. and Sholl, D. S.: First-principles study of chemical stability of the lithium oxide garnets Li$_7$La$_3$M$_2$O$_{12}$ (M = Zr, Sn, or Hf). Journal of Physical Chemistry, 118(31):17402–17406, 2014.

51. Cheng, L., Crumlin, E. J., Chen, W., Qiao, R., Hou, H., Lux, S. F., Zorba, V., Russo, R., Kostecki, R., Liu, Z., Persson, K., Yang, W., Cabana, J., Richardson, T., Chena, G., and Doeff, M.: The origin of high electrolyte–electrode interfacial resistances in lithium cells containing garnet type solid electrolytes. Physical Chemistry Chemical Physics, 16(34):18294–18300, 2014.

52. Ohta, S., Seki, J., Yagi, Y., Kihira, Y., Tani, T., and Asaoka, T.: Co-sinterable lithium garnet-type oxide electrolyte with cathode for all-solid-state lithium ion battery. Journal of Power Source, 265(1):40–44, 2014.

53. Kerman, K., Luntz, A., Viswanathan, V., Chiang, Y.-M., and Chen, Z.: Review—practical challenges hindering the development of solid state Li ion batteries. Journal of The Electrochemical Society, 164(7):A1731, 2017.

54. Shimonishi, Y., Toda, A., Zhang, T., Hirano, A., Imanishi, N., Yamamoto, O., and Yasuo-Takeda: Synthesis of garnet-type $Li_{7-x}La_3Zr_2O_{12-1/2x}$ and its stability in aqueous solutions. Solid State Ionics, 183(1):48–53, 2011.

55. Ishiguro, K., Nemori, H., Sunahiro, S., Nakata, Y., Sudo, R., Matsui, M., Takeda, Y., Yamamoto, O., and Imanishi, N.: Ta-doped $Li_7La_3Zr_2O_{12}$ for water-stable lithium electrode of lithium-air batteries. Journal of The Electrochemical Society, 161(5):A668, 2014.

56. Ren, Y., Deng, H., Chen, R., Shen, Y., Lin, Y., and Nan, C.-W.: Effects of Li source on microstructure and ionic conductivity of Al-contained $Li_{6.75}La_3Zr_{1.75}Ta_{0.25}O_{12}$ ceramics. Journal of the European Ceramic Society, 35(2):561–572, 2015.

57. Okumura, T., Nakatsutsumi, T., Ina, T., Orikasa, Y., Arai, H., Fukutsuka, T., Iriyama, Y., Uruga, T., Tanida, H., Uchimotoa, Y., and Ogumib, Z.: Depth-resolved X-ray absorption spectroscopic study on nanoscale observation of the electrode–solid electrolyte interface for all solid state lithium ion batteries. Journal of Materials Chemistry, 21(27):10051–10060, 2011.

58. Moncton, D. E.: The advanced photon source a national synchrotron radiation research facility. Argonne National Laboratory, 1997.

59. Toby, B. and Von Dreele, R.: GSAS-II: The genesis of a modern open-source all purpose crystallography software package. Journal of Applied Crystallography, 46(2):544–549, 2013.

60. Wolfman, M.: Scimap. https://github.com/canismarko/scimap/, 2015.

61. Trease, N., Seymour, I., Radin, M., Liu, H., Liu, H., Hy, S., Chernova, N., Parikh, P., Devaraj, A., Wiaderek, K., Chupas, P., Chapman, K., Whittingham, M., Meng, Y., Van, A., and Grey, C.: Identifying the distribution of Al_3^+ in $LiNi_{0.80}Co_{0.15}Al_{0.05}O_2$. Chemistry of Materials, 28:8170–8180, 2016.

62. Zheng, J., Yang, Z., Dai, A., Tang, L., Wei, H., Li, Y., and He, Z.: Boosting cell performance of $LiNi_{0.80}Co_{0.15}Al_{0.05}O_2$ via surface structure design. Small, 15(50):1904854, 2019.

63. Lin, Y., Xu, M., Tian, Y., Fan, W., Yu, L., and Li, W.: Understanding impacts of environmental relative humidity to the cell performance based on $LiNi_{0.80}Co_{0.15}Al_{0.05}O_2$. Materials Chemistry and Physics, 211:200–205, 2018.

64. Zhang, L., Fu, J., and Zhang, C.: Mechanical composite of $LiNi_{0.80}Co_{0.15}Al_{0.05}O_2$/carbon nanotubes with enhanced electrochemical performance for lithium-ion batteries. Nanoscale Reseach Letters, 12(1):376, 2017.

65. Matsumoto, K., Kuzuo, R., Takeya, K., and Yamanaka, A.: Effects of CO_2 in air on Li deintercalation from $LiNi_{1-x-y}Co_xAl_yO_2$. Journal of Power Sources, 81-82:558–561, 1999.

66. Zhuang, G. V., Chen, G., Shim, J., Song, X., Ross, P. N., and Richardson, T. J.: Li_2CO_3 in $LiNi_{0.80}Co_{0.15}Al_{0.05}O_2$ cathodes and its effects on capacity and power. Journal of Power Sources, 134:293–297, 2004.

67. Chen, T., Li, X., Wang, H., Yan, X., Wang, L., Deng, B., Ge, W., and Qu, M.: The effect of gradient boracic polyanion-doping on structure, morphology, and cycling performance of ni-rich $LiNi_{0.8}Co_{0.15}Al_{0.05}O_2$ cathode material. Journal of Power Sources, 374:1–11, 2018.

68. Lebens-Higgins, Z. W., Faenza, N. V., Radin, M. D., Liu, H., Sallis, S., Rana, J., Vinckeviciute, J., Reeves, P. J., Zuba, M. J., Badway, F., Pereira, N., Chapman, K. W., Lee, T.-L., Wu, T., Grey, C. P., Melot, B. C., Ven, A. V. D., Amatucci, G. G., Yang, W., and Piper, L. F. J.: Revisiting the charge compensation mechanisms in $LiNi_{0.8}Co_{0.2-y}Al_yO_2$ systems. Materials Horizons, 6(10):2112–2123, 2019.

69. Yoon, W.-S., Chung, K. Y., McBreen, J., and Yang, X.-Q.: A comparative study on structural changes of $LiCo_{1/3}Ni_{1/3}Mn_{1/3}O_2$ and $LiNi_{0.8}Co_{0.15}Al_{0.05}O_2$ during first charge using in situ XRD. Electrochemistry Communications, 8(8):1257–1262, 2006.

70. Ge, M., Wi, S., Liu, X., Bai, J., Ehrlich, S., Lu, D., Lee, W.-K., Chen, Z., and Wang, F.: Kinetic limitations in single-crystal high-nickel cathodes. <u>Angewandte Chemie International Edition</u>, 2020.

71. Yang, C., Fu, K., Zhang, Y., Hitz, E., and Hu, L.: Protected lithium-metal anodes in batteries: from liquid to solid. <u>Advanced Materials</u>, 29:1701169, 2017.

72. Liu, Q., Geng, Z., Han, C., Fu, Y., Li, S., bing He, Y., Kang, F., and Li, B.: Challenges and perspectives of garnet solid electrolytes for all solid-state lithium batteries. <u>Journal of Power Source</u>, 389:120–134, 2018.

73. Cheng, L., Chen, W., Kunz, M., Persson, K., Tamura, N., Chen, G., and Doeff, M.: Effect of surface microstructure on electrochemcial performance of garnet solid electrolytes. <u>Applied Materials and Interfaces</u>, 7:2073–2081, 2015.

74. Li, Y., Han, J.-T., Wang, C.-A., Xie, H., and Goodenough, J. B.: Optimizing Li^+ conductivity in a garnet framework. <u>Journal of Materials Chemistry</u>, 22(30):15357–15361, 2012.

75. Jin, Y. and McGinn, P.: Al-doped $Li_7La_3Zr_2O_{12}$ synthesized by a polymerized complex method. <u>Journal of Power Sources</u>, 96(20):8683–8687, 2011.

76. Andrei A. Bunaciu, Elena Gabriela Udristioiu, H. Y. A.-E.: X-ray diffraction: Instrumentation and applications. <u>Critical Reviews in Analytical Chemistry</u>, 45:289–299, 2015.

77. Bramble, M., Flemming, R., and McCausland, P.: Grain size, 'spotty' XRD rings, and chemin: Two-dimensional X-ray diffraction as a proxy for grain size measurement in planetary materials. <u>45th Lunar and Planetary Science Conference</u>, 2014.

78. Che, G., Jirage, K. B., Fisher, E. R., Martin, C. R., and Yoneyama, H.: Chemical-vapor deposition-based template synthesis of microtubular TiS_2 battery electrodes. <u>Journal of The Electrochemical Society</u>, 144:4296–4302, 1997.

79. Luo, C., Xu, Y., Zhun, Y., Liu, Y., Zheng, S., Liu, Y., Langrock, A., and Wang, C.: Selenium at mesoporous carbon composite with superior lithium and sodium storage capacity. <u>ACS Nano</u>, 7(9):8003–8010, 2013.

80. Reimers, J. N. and Dahn, J. R.: Electrochemical and in situ X-ray diffraction studies of lithium intercalation in Li_xCoO_2. Journal of The Electrochemical Society, 139(8):2091, 1992.

81. Mark, L. and Rex, P.: Structure Determination by X-ray Crystallography. Springer, 2013.

82. T., E.: Structural study by energy dispersive X-ray diffraction. Springer, 1981.

Chao Li
Curriculum Vitae

Education

2010–2014 : **B.Sc, Chemistry**, *University of Massachusetts Boston.*
B.Sc, Business Administration and Management, *University of Massachusetts Boston.*

Publications and Conference Presentations

Journal Article/Manuscripts in Preparation

2021 **Chao Li**, Mark Wolf, and Jordi Cabana. Surface Impurities Affect Macroscopic Transport in $LiNi_{0.80}Co_{0.15}Al_{0.05}O_2$ Cathodes. *In Preparation*, 2021.

2021 Regina Garcia-Mendez, **Chao Li**, Michael J. Wang, Ruqing Xu, Jeff Sakamoto, and Jordi Cabana. Stable Li Eletrodeposition Gradient Induced by Changes in Microstructure,Mechanical and Transport Properties of $Li_7La_3Zr_2O_{12}$ Solid Electrolyte. *In Preparation*, 2021.

2015 Dong Zheng, Xuran Zhang, **Chao Li**, Meaghan E. Mckinnon, Rachel G. Sadok, Deyu Qu, Xiqian Yu, Hung-Sui Lee, Xiao-Qing Yang, and Deyang Qu. *Qualitative Chromatographic Determination of Dissolved Elemental Sulfur in the Non-aqueous Electrolyte for Lithium-Sulfur Batteries.* **Jornal of The Electrochemical Society**, volume 162, pages A203–206, 2015.

Conference Presentations

2019 **Chao Li**, Mark Wolf, and Jordi Cabana. *Visualization of Inhomogeneity Formation on the Cathode Materials of Lithium-ion Battery by X-ray Microdiffraction.* **Materials Research Society Fall Meeting and Exhibit**. Poster Presentation, 2019.

2018 **Chao Li**, Will Judge Mark Wolf, and Jordi Cabana. *Visualization of Chemical Diversity in Battery Materials at Multiple Length Scales.* **Functional and Regenerative Materials Workshop**. Poster Presentation, 2018.

2014 **Chao Li**, Dong Zheng, and Deyang Qu. *Reexamining the Chromatographic Separation of Polysulfide Species on Reversed Phase HPLC.* **Annual Northeast Student Chemistry Research Conference**. Poster Presentation, 2014.

Research Experience

University of Illinois at Chicago, Chicago IL

Advisor : **Dr. Jordi Cabana**.

Jan,2018 – present **Visualization of Heterogeneity of Cathode by μX-ray Diffraction**.
Design and implement a protocol of combined galvanostatic cycling μXRD to study heterogeneity in cathodes based on layered transition-metal-oxide material, $LiNi_{0.80}Co_{0.15}Al_{0.05}O_2$, design for application with high energy density. Develop a methodology of μX-ray Diffraction with Bruker D8 for *ex-situ* cathode mapping of cathode heterogeneity.

Jan,2018 – present **Operando μX-ray Diffraction Imaging of Single Particles of Cathode Materials**.
Design and implement *operando* mapping with μX-ray diffraction to investigate kinetic effects on single particles of $LiNi_{0.80}Co_{0.15}Al_{0.05}O_2$ during cycling at different charging/discharging rates. The synchrotron at Argonne National Lab was utilized for efficient data collection at Beamline section 34-ID-E.

Collaborator : Dr. Ruqing Xu

June,2018 – present	**Strain Analysis in a Solid Electrolyte by μX-ray Laue Diffraction**. Lead and design a method of μX-ray Laue Diffraction mapping to investigate the strain difference across the solid electrolytes $Li_7La_3Zr_2O_{12}$. The correlation between the deviatoric strain and electrochemical performance of the electrolytes was proved through the strain analysis.
Collaborator :	Dr. Regina Garcia-Mendez and Dr. Ruqing Xu and Dr. Jeff Sakamoto and Michael J. Wang

University of Massachusetts Boston, Boston MA

Advisor :	**Dr. Deyang Qu**.
Sep,2012 – Dec,2014	**Reexamining the Chromatographic Separation of Polysulfiede Species on Reversed Phase HPLC**. Assisted with Li-S cell assembling. Applied reversed phase HPLC tandem with electrospray ionization mass spectrometry (RP-HPLC ESI/MS) to examine the chromatographic separation of polysulfide species. The analysis could help the further research on the optimization and modification of the performance and the design of the Li-S battery.
Director :	**Dr. Dong Zheng**
Sep, 2013 – May 2014	**Qualitative Chromatographic Determination of Dissolved Elemental Sulfur in the Non-aqueous Electrolyte for Lithium-Sulfur Batteries**. Assisted senior researchers and collaborated with other undergraduate and graduate students to make a qualitative analysis of dissolved elemental sulfur in the non-aqueous electrolytes for Li-S batteries. HPLC/UV method was applied to determine the solubility of sulfur in 12 different pure solvents and in 22 different electrolytes.

Professional Skills

Lab Skills	Powder/Micro/Laue XRD, Cell Assembling (coin cell and AMPIX cell), Cell Testing
Data Analysis	EC/BT Lab, EVA.Diffraction, GSASII, Python, Image J
Instruments	Bruker D8, HPLC, GC-MS, ATR-FTIR, ICP-IES
Languages	English, Chinese(Mandarin)

Teaching Assistantship

Fall, 2020 :	**CHEM314: Inorganic Chemistry**, UIC.
Spring, 2020 :	**CHEM314: Inorganic Chemistry**, UIC.
Fall, 2018 :	**CHEM314: Inorganic Chemistry**, UIC.
Summer,2018:	**CHEM122/123: General Chemistry I and Lab**, UIC.
Spring, 2018 :	**CHEM314: Inorganic Chemistry**, UIC.
Fall, 2017 :	**CHEM314: Inorganic Chemistry**, UIC.
Summer,2017:	**CHEM122/123: General Chemistry I and Lab**, UIC.
Spring, 2017 :	**CHEM122/123: General Chemistry I and Lab**, UIC.
Fall, 2016 :	**CHEM124/125: General Chemistry II and Lab**, UIC.